2012

A Paleoclimate Modeling Experiment to Calculate the Soil Carbon Respiration Flux for the Paleocene-Eocene Thermal Maximum

David M. Tracy
University of Massachusetts Amherst

A PALEOCLIMATE MODELING EXPERIMENT TO CALCULATE THE SOIL CARBON RESPIRATION FLUX FOR THE PALEOCENE-EOCENE THERMAL MAXIMUM.

A Thesis Presented

By

David M. Tracy

Submitted to the Graduate School of the
University of Massachusetts Amherst in partial fulfillment
of the requirements for the degree of

MASTER OF SCIENCE

MAY 2012

DEPARTMENT OF GEOSCIENCES

A PALEOCLIMATE MODELING EXPERIMENT TO CALCULATE THE SOIL CARBON RESPIRATION FLUX FOR THE PALEOCENE-EOCENE THERMAL MAXIMUM.

A Thesis Presented

By

David M. Tracy

Approved as to style and content by:

_____
Robert DeConto, Chair

_____
Steven Petsch, Member

_____
Mark Leckie, Member

_____
Mark Leckie, Department Head
Department of Geosciences

ACKNOWLEDGEMENTS

In the journey of completing this project I have had assistance from many people around me. First and foremost I would like to thank Jackie, my loving girlfriend, for all of her support and understanding over this nearly four year long project. I would never have completed this research if not for her. An endless thank you is owed to my family; Dad, Lisa, and Melissa, for getting me to where I am today. There is no appropriate way to convey the amount of appreciation I have for all that you have provided for me throughout my life. Mom, although you may not have been physically beside me I know you have been looking over and helping me along this journey, thank you.

I would like to thank my fellow classmates and colleagues who I've turned to for support in one form or another. I would like to thank the immensely gifted staff and professors of the UMass Geosciences department, without their support this project would have never been completed. I would like to thank my committee members for the endless emails, meetings, reviews, discussions, and collaboration on this project. Together, they were the guiding light for my success.

Lastly, I would like to thank Rob for being the mastermind behind this work and for his endless patients with me while I learned my way. I greatly appreciate having the opportunity to work with and get to know you.

ABSTRACT

A PALEOCLIMATE MODELING EXPERIMENT TO CALCULATE THE SOIL CARBON RESPIRATION FLUX FOR THE PALEOCENE-EOCENE THERMAL MAXIMUM.

MAY 2012

DAVID M. TRACY, B.S., STATE UNIVERSITY OF NEW YORK COLLEGE AT ONEONTA

M.S., UNIVERSITY OF MASSACHUSETTS AMHERST

Directed by: Professor Robert DeConto

The Paleocene-Eocene Thermal Maximum (PETM) (55 million years ago) stands as the largest in a series of extreme warming (hyperthermal) climatic events, which are analogous to the modern day increase in greenhouse gas concentrations. During the PETM, global surface temperatures rose ~5-9°C, however, the cause of this warming remains elusive (Zeebe *et al*., 2009). Driven by an orbit trigger of a series of extreme Milankovitch-based cycles (Lourens *et al*., 2005, Galeotti *et al*., 2010), the PETM is marked by a large (-3‰) carbon isotope ($\partial^{13}C$) excursion. For many years, highly depleted (-60‰) methane hydrates were assumed to be the main culprit of this warming event. Zeebe *et al*., (2009) noted that a methane based release would only account for 3.5°C of warming. An isotopically heavier carbon, such as that of soil and C3 plants, has the potential to account for the warming and signature observed in the $\partial^{13}C$ record (Zachos *et al*., 2005).

During the early Eocene, high latitude surface temperatures created favorable conditions for terrestrial vegetation growth and the sequestration of terrestrial carbon. A

large untapped terrestrial carbon reservoir, such as that within permafrost regions, contains the potential, if degraded, to account for the isotopic excursion as well as the global temperature increase observed during the PETM.

Using an integrated steady state ocean, atmosphere, soil global climate model (GENESIS) with fully coupled vegetation model (BIOME4), we show that adequate conditions for permafrost growth and terrestrial carbon sequestration did exist during the lead up to the PETM. By calculating the flux of net primary production (NPP) and soil respiration (Rs), via an offline soil respiration model, we demonstrate that the biodegradation of permafrost-based carbon reservoirs had the potential to drive the PETM. Furthermore, we show that the natural planetary response to unbalanced carbon reservoirs resulted in the terrestrial sequestration of atmospheric carbon via permafrost regeneration, yielding a vulnerable carbon reservoir for the subsequent hyperthermal.

TABLE OF CONTENTS

Page

LIST OF TABLES

LIST OF FIGURES

Figure Page

LIST OF EQUATIONS

CHAPTER 1

INTRODUCTION

The Paleocene-Eocene Thermal Maximum (PETM) has, in recent years, become a point of study as an example of the climate system response to a large and sudden increase in greenhouse gas concentrations. Over the period of a few thousand years, the global surface temperature rose ~5-9°C, however, the ultimate cause of the warming is still largely unknown (Zeebe *et al.*, 2009). Many researchers (Dickens *et al*., 1997, Bowen *et al*., 2004, Thomas *et al*., 2002) have cited the release of methane (CH_4) from frozen marine methane hydrates as the main culprit. The event is marked by a negative $\partial^{13}C$ excursion that translates to a ~2,000GtC (Gigaton Carbon) release (Zachos *et al*., 2005) of carbon if ones assumes a methane hydrate source with an isotopic composition of -60 per mil. However, this mass of carbon that is seen in the record (ODP sites 1208, 1221; Zeebe *et al.,* 2009) only accounts for ~3.5°C warming over that time period. Bowen *et al.* (2004) noted that the remainder of the temperature increase could be attributed to amplifying feedbacks including elevated relative humidity, changes in ocean circulation/heat transport, and increased CH_4 input from wetlands. It is unlikely, however, that these feedbacks accounted for an additional 1.5-5.5°C increase in equatorial and polar temperatures, respectively. Instead, I propose that another source of carbon in addition to methane hydrates contributed to the warming. This study will investigate circum-Arctic and Antarctic terrestrial soil-CO_2 efflux as possible carbon sources that would account for the previously unexplained warming during the PETM.

The evidence, which prompts such a study, lies within the carbon and temperature reconstructions performed for the PETM period. Zeebe *et al.,* (2009) state that the extended duration of the event cannot be explained without continued carbon release. Zachos *et al.,* (2005) noted that an input of >4500 GtC would be required for the observed magnitude of global temperature rise, yet <2000 GtC can be accounted for by hydrate release alone (Pagani et al., 2009). A release of ~4500 GtC from a methane source would produce an isotopic signature greater than what is observed (~-4‰). Another source of carbon, that is isotopically heavier (less depleted) than the carbon in methane hydrates (-60‰), would be required to accommodate the observed temperature excursion as well as the stable carbon isotope excursion. Zachos *et al.,* (2005) points out that oxidation of isotopically heavier organic carbon, which varies from -22‰ to -30‰, could constitute the missing carbon. Soil and C3 plant carbon lie in this range of values (-20‰ to -35‰) (Bernoux *et al.*, 1998) and could account for the missing source. Kurt *et al*., (2003) studied the ratio between organic carbon (C_{org}) and pyrite sulfur (S_{py}), which is deduced to be an indicator of C_{org} burial environment. High C_{org}/S_{py} burial ratios, which leading up to the PETM, are thought to indicate an enhanced terrestrial accumulation of C_{org}.

During this time period (55.5 Ma) high latitude SST's were on the order of ~18°C which increased to ~23°C during the event (Sluijs *et al*., 2006). Weijers *et al.* (2007) observed high latitude continental annual mean air temperatures as high as 25°C during the PETM based on leaf margin analysis and oxygen isotope analysis of fossil teeth enamel. The high latitude mean air temperatures happen to coincide with the optimal production temperatures (25°C) of CH_4 from Peat (Metje *et al.*, 2005). Soil carbon

respiration reaches its optimal output temperature between ~15°C and 25°C (Raich *et al*., 1992). Peatlands and soil carbon alike uphold a high sensitivity to variations in temperature.

In a study done on high latitude northern peatland soils, it was concluded that a 1°C increase in global temperature would raise soil respiration by .038 – .1GtC per year (based on an area of 3.30 x 10^6 Km^2), acting as a positive feedback to global warming (Dorrepaal *et al.*, 2009). More importantly the 1°C increase in temperature affected soil carbon respiration to a depth of 50cm. The carbon respiration from the soil is controlled by a number of variables such as temperature and soil water content (Davidson *et al.* 1998), which is defined as the percentage of soil pore-space that is filled with water (Linn *et al*. 1984). An increase in this percentage has varying effects. When increased, the aerobic microbial activity is also elevated, however, once the percentage exceeds a critical point (~60%), the amount of pore water begins to limit the diffusion and availability of oxygen (Linn *et al*. 1984). Nonetheless, if the level is held to 40% – 65%, then CO_2 production is maximized (max being 60% pore space filled) (Linn *et al.* 1984).

In addition to high northern latitudes, Antarctica was a possible location for these methane producing wetlands and carbon releasing soils due to its polar-centered location and vast area of vegetated land surface 55 million years ago. Antarctica was largely ice-free and the landscape was quite different than today. Modern Antarctica has an area of fourteen million square-kilometers. At the time of the PETM, due to the crustal thinning associated with the late Cenozoic rifting between East and West Antarctica, the total subaerial land area was ~20% bigger than present day (Wilson *et al*., 2009). Upon preliminary calculations based on a rough estimate of biome distribution from the

BIOME4 control simulation, utilizing the current area of Antarctica with estimated vegetation types of 60% boreal forest/woodlands (322±31gC/m^2/yr), 35% tundra (60±6gC/m^2/yr), and 5% wetlands (413±76gC/m^2/yr). Antarctica has the potential to produce ~3.29GtC/yr of soil carbon alone (Raich *et al*., 1992). This is a very crude estimate to point out the potential role of this huge landmass in the global carbon cycle, prior to its glaciation in the early Oliogocene ~34 Ma (DeConto *et al*., 2003).

DeConto *et al*., 2012 note that initial orbitally induced global warming, due to an extreme high eccentricity and high obliquity orbit (Lourens *et al*., 2005; Galeotti *et al*., 2010), in combination with steadily increase background greenhouse gas concentrations would have had the ability drive the decomposition of global soil organic carbon pools in circum-Arctic and Antarctic terrestrial permafrost. Post peak PETM global warming, global soil organic carbon pools would have sequestered atmospheric carbon. This unbalanced flux of atmospheric carbon into the global soil organic carbon pool would have been observed via increased annual net primary production and decreased annual soil respiration (DeConto *et al.,* 2012*)*. This recharging of the global soil organic carbon pools would have provided a vulnerable source of organic carbon for the subsequent hyperthermals that followed the PETM (DeConto *et al.,* 2012*)*. This research concentrates on the additional ongoing contribution of enhanced organic carbon flux from polar residual permafrost and wetland regions at the PETM and the successive hyperthermals.

1.1 Net Primary Production and Soil Respiration

Terrestrial ecosystems sequester and release huge quantities of carbon annually. Depending on variables such as vegetation cover, temperature, and precipitation, the

amount of carbon sequestered or released will vary. This research focuses on two soil parameters, Net Primary Production (NPP) and Soil Respiration (Rs). NPP is defined as the net amount of carbon captured by land plants through photosynthesis each year (Melillo *et al*., 1993). Rs refers to the process of removing/releasing carbon from the soil in the form of CO_2 (Raich *et al*., 1992). Contributors to this process are plant roots as well as microbes living within the soil column, which oxidize carbon-bearing materials (Raich *et al*., 1992). Rs output varies based on the gradient of CO_2 between the soil and the atmosphere. This gradient is influenced by air temperature, soil pore space, and wind speed (Raich *et al*., 1992). The ratio of NPP to Rs will determine whether there is a net uptake of carbon by the soil or a net release. On average this ratio is ~1:1 indicating that the amount of carbon sequestered and released over a given time period is equal.

1.2 Permafrost as a Global Contributor to CO_2

Permafrost is defined as subsurface Earth materials remaining below 0°C for two consecutive years (Schuur *et al*., 2008). According to the International permafrost association (IPA), 23 million km^2 of continuous, discontinuous, isolated, and sporadic permafrost exist in the world today, most of which are located in the circumpolar north (http://ipa.arcticportal.org/). Permafrost thickness varies from 350 to 650 meters in continuous regions to 1 to 50 meters in discontinuous regions (Schuur *et al*., 2008). In unglaciated regions of Siberia, permafrost can reach a depth of 1,450 meters (Schuur *et al*., 2008). Permafrost is significant to this research due to its carbon sequestering potential. Permafrost exists in regions with a low mean annual temperature (MAT). Due to this, the microbial activity (carbon respiring activity) within the soil column is largely reduced. This reduction in respiring activity has the affect of enabling huge quantities of

carbon to be stored within the soil column with little carbon flux to the atmosphere. Tarnocai et al., (2009) estimated that the modern northern circumpolar permafrost region contains 1,672 PgC (PgC = Peta grams of carbon) (1 Pg = 1 billion metric tons). Permafrost characteristics are controlled by latitude and more importantly the MAT at a given latitude. A global temperature increase would alter the polar boundary of where permafrost is sustained, thus beginning the thawing process and accelerating the soil column microbial activity (Schuur *et al*., 2008). Due to current global warming, it is estimated that 0.5 to 1 PgC per year is being released from thawing permafrost regions (Schuur *et al.,* 2008). This release can be partially counteracted by the northern advance of various biomes, which sequester higher carbon amounts, into regions where biomes and soils with low carbon contents once existed (Schuur *et al*., 2008). An example of this would be Boreal forest advancing into a region where tundra once existed (Schuur *et al*., 2008) or vice versa if the tundra biome contains large quantities of peat. However, this process may be negated by the soil respiration that occurs within the soil column of those specific biomes (Schuur *et al*., 2008). The net release of carbon, in the form of CO_2 or CH_4, which rapidly dissociates to CO_2, has the potential to result in significant global warming. In return, this warming is likely to accelerate the thawing of further permafrost regions and increase the soil respiration rate.

1.3 Orbital Trigger

Until recently it was not possible to accurately calculate the Milankovitch parameters (eccentricity, precession, obliquity) cyclicity in correlation to the timing of the PETM. This was simply due to the time that had elapsed since the event until present and lack of high resolution observed records. Laskar (2004) developed a series of

mathematical astronomical solutions for the last 50 millions years, that have been combined with high resolution observed data from the Western Tethys Contessa Road section (Galeotti *et al*., 2010) and ODP leg 208 on the Walvis ridge (Lourens *et al*., 2005) to calculate the timing and amplitude of the eccentricity and precession cycles. It was found that a long 405 Kyr eccentricity maxima directly corresponds to the PETM (Galeotti *et al*., 2010). Given the possible feedbacks from insolation, the climate system, and the biosphere, the long-term eccentricity modulation forcing would have been largely increased and potentially responsible for the onset of the PETM (Galeotti *et al*., 2010).

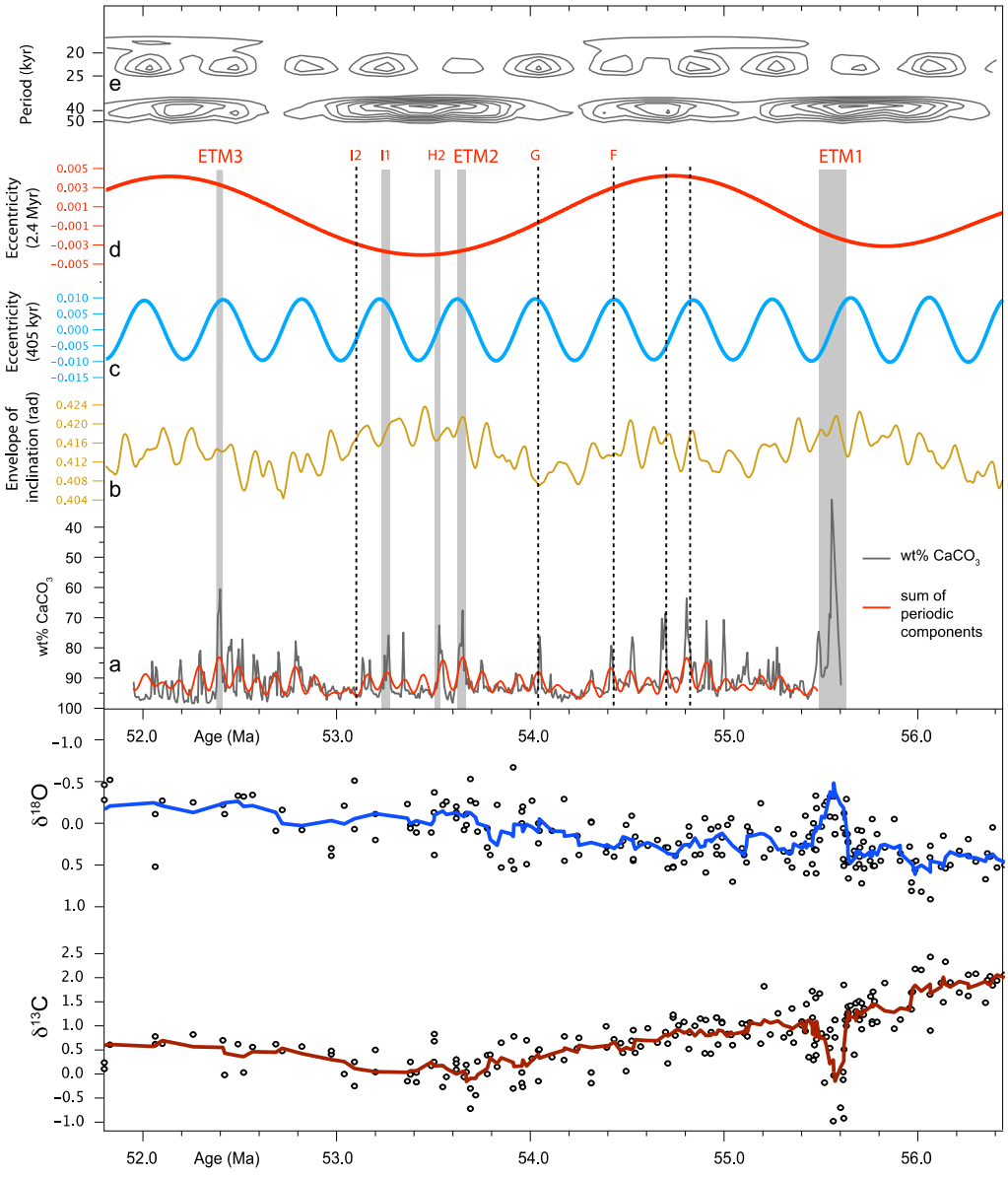

Figure 1.1: Mathematically calculated orbital pacing of ETM events Galeotti *et al.*, 2010, were able to use orbital algorithms finely tuned using the Contessa Road section stratigraphy to pin point specific orbitally induced global warming events. Some of these events include the PETM (ETM1), ETM2, and ETM3 which all fall on nodes of high eccentricity and obliquity.

1.4 Research Statement

This investigation will evaluate the role of Antarctic soil carbon as a major carbon contributor during the PETM, by testing the hypothesis that "*The release of carbon into the atmosphere from Antarctica via soil carbon respiration was largely responsible for the Paleocene/Eocene thermal maximum".* This research will not only be vital in understanding the PETM itself but may also serve as an analogue for future climate as similar boreal environments continue to warm, resulting in the melting of permafrost and the degradation of soil carbon stores. The PETM serves as the best-documented, rapid-warming event that resembles the current rate of global warming, yet there is much that remains unknown. That very reason begs for more intensive research to explore all potential scenarios that can explain such an event.

This document is arranged in a progression from an explanation of the various software, input files, and functions utilities to drive the experiments or simulations as described in the Methods section (Chapter 2). The result of these simulations are described in the Results section (Chapter 3). The overall outcome is located in the discussion section (Chapter 4). The final conclusion of this research statement is provided in Chapter 5. The All tables, figures, and equations are interbedded within the text in a fashion that is relevant to each section. Figure, table, and equation labeling is consistent throughout each section and follows a numeric scheme based on the chapter nomenclature (i.e. Figure 1 for Chapter 1 = Figure 1.1, Figure 2 = Figure 1.2, etc).

CHAPTER 2

METHODS

2.1 Mathworks MATLAB R2008b

Mathworks MATLAB is a matrix-based forth-generation computing language numerical programming environment with a graphical user interface. All pre and post data processing was conducted via computer programs written for and executed in MATLAB. MATLAB contains NetCDF (Network Common Data Form), statistical, mapping, and visualization packages, which makes it an ideal tool for handling large quantities of data such as GCM outputs. In total, over 110 programs and scripts were written and used to complete this research.

2.2 Global Climate Model: Genesis Version 3.0

This research utilizes the Global Environment and Ecological Simulations of Interactive Systems (GENESIS) model version 3.0 (Thompson and Pollard., 1997) with an embedded biogeochemistry-biogeography model (Biome4) (Kaplan *et al*., 2003, Haxeltine and Prentice., 1996). GENESIS is a fully coupled global climate model of atmosphere, ocean, vegetation, soil, snow, icesheets, and sea ice. The atmospheric model is a 3-D atmospheric general circulation model (AGCM), coupled to the land-surface model by a Land-Surface-Transfer scheme (LSX), which computes fluxes through the vegetation model (Pollard and Thompson, 1995). The spatial resolution of the land surface models is two degrees of longitude by two degrees of latitude (2° x 2°). The AGCM has a slightly coarser resolution of 3.75° x 3.75°. In the configuration used here,

the ocean component is a non-dynamic slab (50-m), with predicted sea surface temperatures, ocean heat transport, and sea ice.

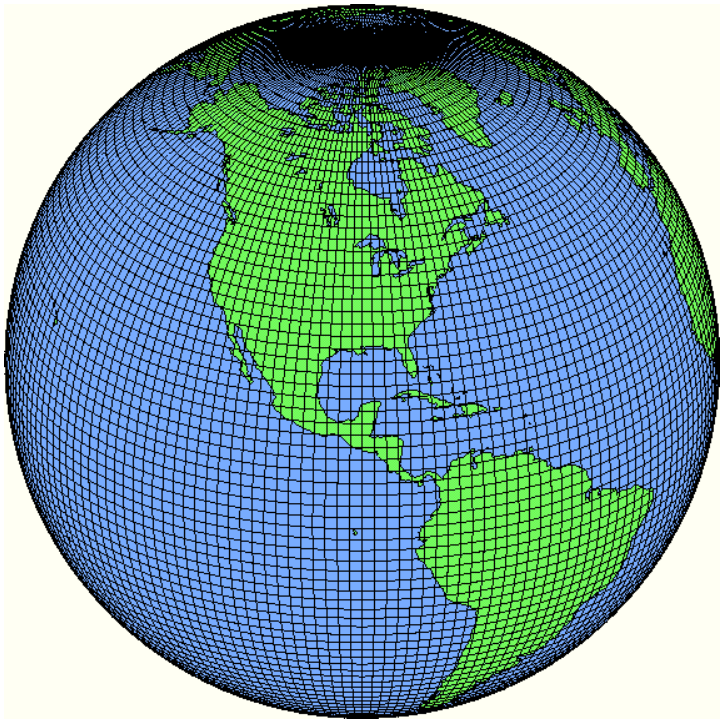

Figure 2.1: The GCM grid with a 2° x 2° lat lon matrix
The above figure represents the resolution of the GENESIS land surface models. The resolution is coarse with the northeastern United States consisting of roughly nine cells. (Thompson and Pollard., 1997)

GENESIS is initialized using a suite of boundary conditions such as surface-type, sea surface temperature, surface topography, etc. These prescribed input files are read by the model during start up and set the base for all calculations made during the course of the model simulation. GENESIS offers the ability to alter these input files allowing users the freedom to experiment with various orbital parameters, green house gas concentrations, and land surface configurations of time periods other than present day (such as the PETM). (Thompson and Pollard., 1997)

2.2.1 GENESIS Boundary Conditions

Upon initial model start-up, input parameters are read into GENESIS that setup the initial boundary conditions acting as baseline variables for the initial calculations as well as set the stage for the model simulation. The simulations completed for this research utilize 2° longitude by 2° latitude resolution (90 rows by 180 columns) input files. These files consist of topography, gravity-wave orographic roughness, atmospheric ozone distribution, surface type, ocean-lake fraction, and soil texture and depth (Pollard and Thompson., 1995). The input files are split between the surface and atmospheric models. GENESIS provides modern day boundary condition input files, however, as used here GENESIS allows for the input of user developed boundary condition files. Chapter 2, Methods, describes in details the various boundary condition files that were created for this research.

2.2.2 GENESIS Subsurface Soil Layers

GENESIS utilizes a multilayer soil model that simulates diurnal and seasonal cycles of heat and moisture in the upper few meters of soil. Each layer contains three prognostic variables: Temperature (T), fractional liquid water content (w_l) to ice-free pore space (soil moisture), and fractional ice content (w_i) relative to total pore space (Pollard and Thompson., 1995). The diffusion of liquid water follows a highly non-linear dependence to soil moisture. Soil temperature diffusion into and within the soil columns follows a linear temperature dependence.

Equation 2.1: Soil Model Equation for liquid Diffusion and Drainage

$$P\frac{\partial w_l}{\partial t} = \frac{\partial}{\partial z}\left[-K_o\, w_l^{2B+3} + K_o\, \phi_o\, B\, w_l^{B+2}\, \frac{\partial w_l}{\partial z}\right]$$

Equation 2.2: Soil Model Equation for Surface to Subsurface Heat Transfer

$$\frac{\partial}{\partial t}(\rho c T) = \frac{\partial}{\partial z}\left[\kappa_g\, \frac{\partial T}{\partial z} + \rho_l c_l \overline{w_l\, T_l}\right]$$

Equation (Eq) (2.1) describes the relationship of the diffusion and drainage of liquid water within the soil column. P is equal to soil porosity, K_o is the saturated hydraulic conductivity, ϕ_o is the saturated soil suction, and B is an empirical soil exponent (Pollard and Thompson., 1995). Eq (2.2) described the net heat flux at the soil surface as well as the diffusion of heat within the soil columns. Variable ρc is the appropriate weighted average for soil, liquid, and ice heat capacity, $\rho_l c_l w_l T_l$ is the heat flux associated with the moisture transport from Eq (2.1), and κ_g is the heat conductivity.

The land-surface models contain a preset soil column, which is broken down into six subunits. Each of the six soil units has a specific depth measuring 5 cm, 10 cm, 20

cm, 40 cm, 1 m, and 2.5 m from top to bottom of the soil column (Pollard and Thompson., 1995). The total thickness of the six layers measures 4.25 m and is able to capture the diurnal and seasonal cycles. The multi-layer soil model also responds to heat and soil moisture fluxes for each layer. These data are output as subsurface temperature (T1 – 6, T1 = top layer & T6 = bottom most layer), fractional liquid water content (WET1 – 6) relative to ice-free pore space, and fractional ice content (WICE1 – 6) relative to total pore space.

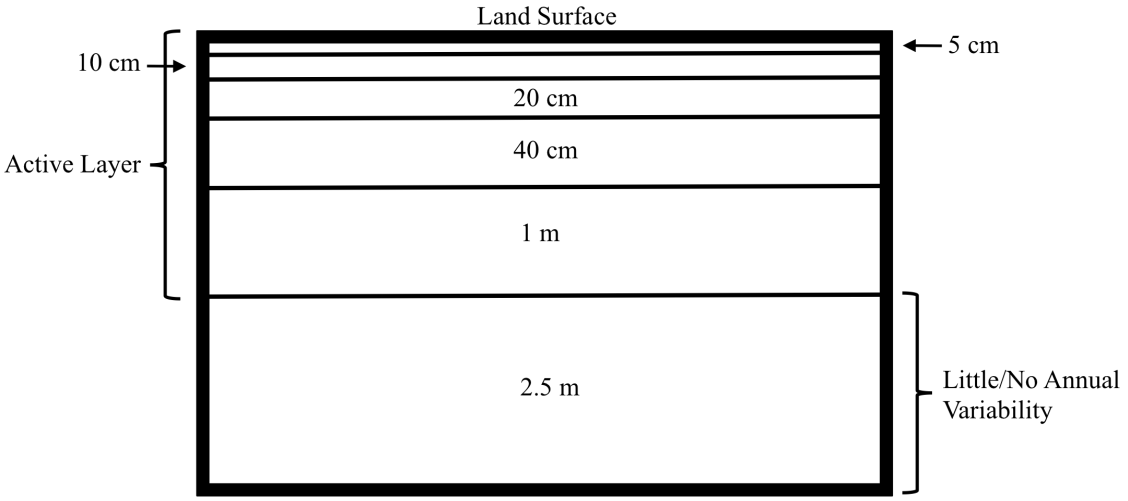

Figure 2.2: Six soil layer thicknesses utilized in the soil model
These layers (not to scale) display the Active Layer and the layer of Little/No Annual Variability. The Active Layer (top 5 layers) exhibits seasonal variation in fractional ice content of the soil pore space as well as soil temperature. Layer 6 (bottom layer) contains little to no variability in soil ice and more importantly little to no variation in soil temperature. In the model, these layers are numbered with 1 = top and 6 = bottom of the soil column. T# represents subsurface soil temperature (the # is equal to the soil layer). This research focuses on T6.

2.2.3 BIOME4 Overview

BIOME4 predicts steady state vegetation distribution, structure, and biogeochemistry via a coupled carbon and water flux model. The model runs offline from GENESIS utilizing variables such as mean monthly temperature, sunshine, and precipitation. The coupled carbon and water flux model determines the seasonal maximum leaf area index (LAI) based on a series of biological and atmospheric parameters. In order to accurately simulate vegetation types per grid cell BIOME4 makes use of twelve plant functional types (PFTs), which represent distinct physiological classes. Once run, the model ranks tree and nontree PFTs for a given grid cell. Based on this information, the model assigns the output grid cell with one of the twenty-eight potential biomes (Table 2.1). Kaplan *et al*., (2003).

Biome #	Biome Type
1	Tropical evergreen forest
2	Tropical semi-deciduous forest
3	Tropical deciduous forest/woodland
4	Tropical xerophytic shrubland
5	Temperate xerophytic shrubland
6	Tropical grassland
7	Temperate grassland
8	Temperate conifer forest
9	Warm mixed forest
10	Cool mixed forest
11	Cool conifer forest
12	Cold mixed forest
13	Temperate deciduous forest
14	Evergreen taiga/montane forest
15	Deciduous taiga/montane forest
16	Tropical savanna
17	Temperate broadleaved savanna
18	Open conifer woodland
19	Temperate sclerophyll woodland
20	Boreal parkland
21	Steppe tundra
22	Shrub tundra
23	Dwarf shrub tundra
24	Prostrate shrub tundra
25	Cushion-forbs lichen and moss
26	Desert
27	Barren
28	Land ice

Table 2.1: The 28 biomes assigned by BIOME4
Each biome is assigned based on the leaf area index and net primary production output of BIOME4. For this research, high latitude biomes such as 14, 23, 24, and 21 are of particular interest.

2.3 Boundary Conditions

2.3.1 PETM Topography

The global topography 55 Ma years ago was vastly different from present day, and for this reason a new topography input file was generated for GENESIS. An existing global topography reconstruction by Jake Sewall and Matt Huber (Sewall *et al*., 2000, Huber *et al*., 2003) is the most current reconstruction for the Eocene, however, their reconstruction underestimates the area of Antarctica. Wilson *et al*., (2009) produced a high-resolution Eocene-Oligocene boundary Antarctica topography reconstruction that accounts for erosion and sediment deposition, thermal contraction, and horizontal tectonic motion. The reconstruction produced by Wilson *et al*., (2009) estimated an Antarctic sub-aerial land area about 20% larger than present day.

The topography reconstruction by Jake Sewall and Matt Huber (Sewall *et al*., 2000, Huber *et al*., 2003) was imported into MATLAB and found to be 90 x 180, which matches the 2° x 2° resolution of the GENESIS land surface models. Rows 78 through 90 and all 180 columns, which contained Antarctica, were removed to leave a gridded space for the updated Antarctica topography. It should be noted that in the Sewall and Huber reconstruction Antarctica is connected to Australia via a sizable mountain range (1800m + peaks) through the Tasmanian Gateway, which the Wilson reconstruction does not display. The Wilson reconstruction data set consists of a column for Latitude, Longitude, and Elevations. In a gridded form, the original data set was formatted in a stereographic (polar) projection, which is the incorrect format for the GENESIS input file. In order to

correct this a transformation was required. To process the data in ArcGIS the gridded Wilson data was exported from MATLAB and saved in a Microsoft Excel spreadsheet file. In ArcGIS the data was transformed to an equidistant cylindrical projection and only the elevation data was saved. The new Wilson data set contained 251 rows by 2,469 columns and required a reduction of the resolution to 12 rows by 180 columns. In order to accomplish this, the data were imported into Microsoft Excel and, using an averaging technique that averaged two adjoining cells of the same row into one cell, the data was processed. This method was applied to the entire data set a series of times until the desired resolution was reached. Through this process, as well as the transformation process, Antarctica was reduced to an area ~21% smaller than the original (9,531,142 km^2 versus the 12,100,000 km^2 of the Wilson *et al*., (2009) reconstruction). To correct this error a nearest neighbor interpolation technique was used to reassign values to the perimeter grid cells. This was done in a meticulous fashion with constant reference to the original Wilson *et al.,* (2009) data set in order to preserve the topography data to the highest level possible. When possible, three surrounding grid points were used in the calculation. Once the process was complete, the Antarctica area measured 12,098,642 km^2. The 12 by 180 Antarctica file was imported into MATLAB and imported into rows 78 through 90 by 180 columns.

2.3.2 PETM Antarctica Tectonic Rotation Correction

The orientation of the new Antarctica landmass did not precisely match the orientation of the original Antarctica landmass from the Seawall and Huber reconstruction. To correct this orientation issue a section of data 12 rows by 1 column (a rectangle of Antarctica) was removed from the 180^{th} column location. The remaining

Antarctica grid cells were then moved by one column leaving the first column empty, which allowed for the removed 12 rows by 1 column of data to be pasted into that location. This has the effect of tectonically rotating Antarctica in a global sense to its correct position 55 million years ago.

2.3.3 PETM Tasmanian Gateway Mountain Range

As mentioned earlier, a mountain range exists in the Sewall and Huber reconstruction that does not exist in the Wilson reconstruction. Utilizing data from the Sewall and Huber reconstruction as well as interpolating from the existing data, the Australian mountain range was connected seamlessly to an existing range in the Wilson reconstruction through the Tasmanian gateway.

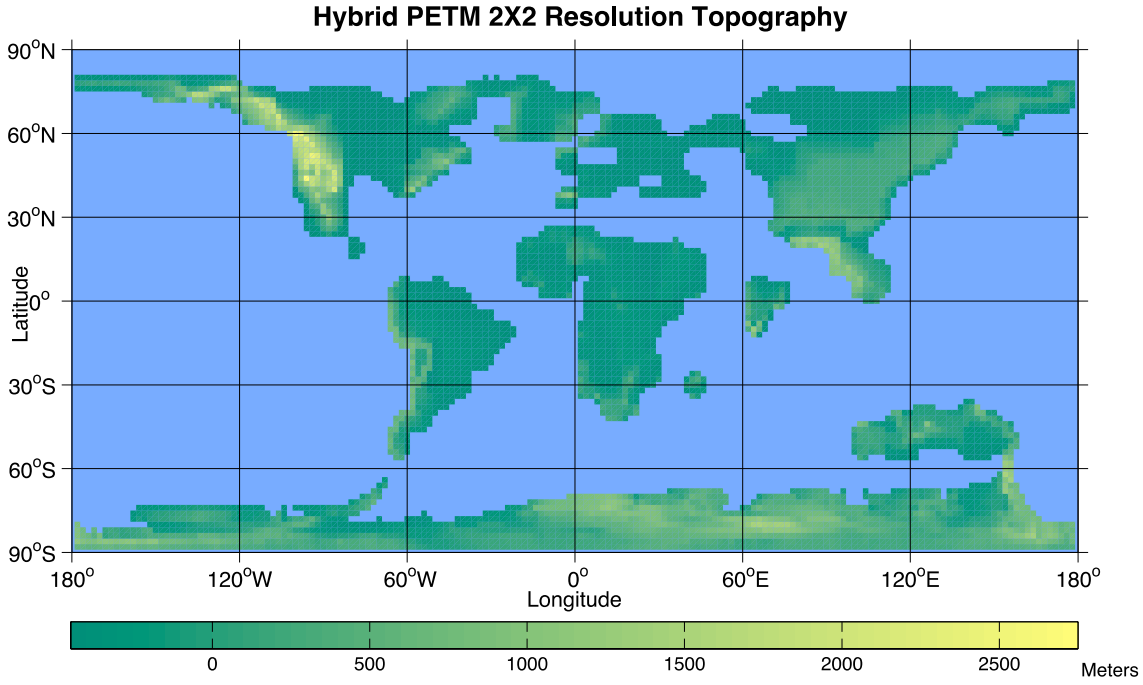

Figure 2.3: Equidistant-cylindrical projection of the hybrid Sewall *et al*., (2000) & Huber *et al*., (2003) and Wilson *et al.,* (2009) reconstruction. The blocky nature of the plot represents the 2° x 2° resolution of the GENESIS land surface models. The elevation of many regions was higher during the PETM than today. The presence of permafrost in many locations may be attributed to topography. This hybrid reconstruction was used in all simulations for this research and was adopted by DeConto *et al*., 2012.

2.3.4 Land Mask File Generation

The final step to complete this process was the creation of a Land Mask or LMASK file for GENESIS. This consists of a 90 x 180 matrix, displaying ones (1) wherever land is present and zeros (0) wherever ocean is present. The data was then exported using the Fortran i-5 format required by GENESIS, which simply contains five spaces or place holders per column. All model simulations for this project utilize the updated topography (Fig. 2.3) file.

2.4 GENESIS Model Simulations

In order to assess the potential for permafrost to have existed during the PETM and then have the ability to collect data from those permafrost regions, as well as other variables of interest, a GCM must be used. GENESIS allows for full control over Milankovitch parameters in addition to atmospheric greenhouse gas concentrations such as carbon dioxide (CO_2), methane (CH_4), and nitrous oxide (N_2O). To simulate such a rapid increase in atmospheric carbon dioxide a series of simulations were preformed with varying CO_2, CH_4, and N_2O in combination with the influence of Eccentricity, Precession, and Obliquity (Table 2.2).

Exp.	CO_2 (eppmv)	CO_2 (ppmv)	CH_4 ppbv	N_2O (ppbv)	Ecc.	Prec. (º)	Obl. (º)	Orbital Forcing
Cont.	400	355	1714	311	0.017	77.06	23.765	-
1	550	500	1200	350	0	0	23.5	Neutral
2	900	750	2100	375	0	0	23.5	Neutral
3	900	750	2100	375	0	0	24.5	High Obl.
4	900	750	2100	375	0.05	270	24.5	Warm Orbit
5	900	750	2100	375	0.05	90	24.5	Cold Orbit
6	1275	1000	3000	400	0	0	23.5	Neutral
7	2680	2000	3500	450	0	0	23.5	Neutral
8	5360	4000	3500	450	0	0	23.5	Neutral

Table 2.2: Displays the experiment number, the concentrations of CO_2 and CH_4, and Milankovitch parameters per model simulation used in this research. The concentrations of greenhouse gases increase with the experiment number. The Milankovitch parameters consist of eccentricity, precession, and obliquity. Eccentricity is the amount that an orbit deviates from a perfect circle (0 = perfect circle). Precession is the prograde angle in degrees from perihelion to the vernal equinox. Obliquity is the tilt angle of the Earth from the orthogonal plane of the Earth to the Sun. Simulation Cont. represents the modern control simulation, which is used for model validation as well as comparison to the other simulations. The control uses modern day (as of 1995) greenhouse gas concentrations and Milankovitch parameters. Values of CH_4 and N_2O are scaled to CO_2 according to Beerling *et al*., 2010.

Each simulation is a sensitivity test, which focuses on one or two parameters. The goal is to incrementally increase CO_2, CH_4, and N_2O, simulating the PETM atmospheric conditions to test the response of the atmosphere and biosphere. Simulations 2, 3, and 4 test the influence of eccentricity and precession in two configurations, boreal austral or summer warm and cold orbits. The definition of a warm or cold austral summer orbit is dependent on the longitude of perihelion during the summer solstice and is directly controlled by the precession and eccentricity (Figure 2.4). When the Northern Hemisphere is angled towards the sun during perihelion it is considered a cold Antarctic orbital configuration, the reverse of which, is a warm orbital configuration, that occurs when the Northern Hemisphere is angled away from the sun during perihelion producing warm Antarctic summers. The Milankovitch parameters are systematically altered to demonstrate the orbital trigger hypothesis by Galeotti *et al*., (2010) and Lourens *et al*., (2005). The Control simulation experiment is testing close to modern atmospheric and orbital conditions and serves as a baseline, which can be validated with observed data.

From the onset to its maximum, the PETM atmospheric CO_2 concentrations rose from ~400ppm to ~2,000ppm (or higher) in a period of ~10,000 years or less (Zachos *et al*., 2008). The goal of this research is to not only accurately simulate terrestrial carbon dynamics in CO_2, but more importantly capture the biosphere's response to the increase in CO_2, for this reason a series of CO_2 and CH_4 increments were used. From these simulations information on permafrost area, NPP, and Rs are calculated.

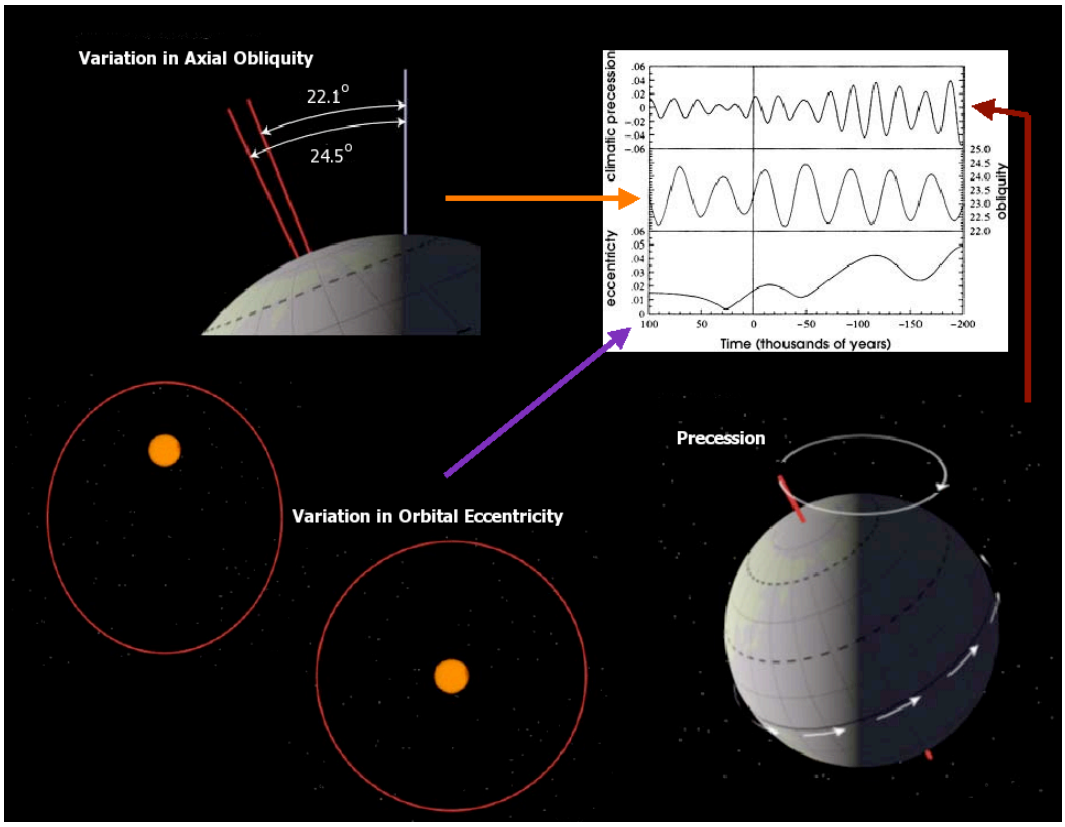

Figure 2.4: A visual representation of Earth's Milankovitch cycles (Precession, Obliquity, and Eccentricity).
Precession is the *wobble* of Earth about its axis. Obliquity is the variation of Earth's axial tilt from 22.1° to 24.5°. Eccentricity is the fluctuation in Earth's orbit path around the sun. A highly eccentric orbit is oval shaped while a orbit with a low eccentricity is circular. The combination of these three planetary and orbital characteristics has the ability to alter the intensity and duration of Earth's seasons (Simmons, A., Hoffman, D. L. 2008).

2.5 Model Output Processing

The Genesis surface model LSX output produces 54 variables of monthly data. This research focuses on the fractional soil ice volume, subsurface temperature, fractional soil water content, vegetation biomes, 2 meters surface temperature, and precipitation. Model simulations are designed to run until a state of equilibrium is reached among all variables. This typically means that, for a GCM of this nature with a 50-m slab ocean

component, the model is run for 30 or more years. In the case of this research, the model simulations were run for 35 years to ensure that the model had fully equilibrated to the initial run conditions (CO_2, CH_4, N_2O, and Milankovitch). In order to make certain that the most accurate data is collected, the last five years of the model simulation are extracted (years 30 – 40). Each variable, which contains monthly data for all 10 years, is then averaged per grid cell per month to produce one file that is 90x180x12 that represents one year of monthly global data that is then used for analysis.

2.5.1 Soil Model Output

Special consideration is given when processing the soil model data for this research. The soil-ice and temperature data are considered in the permafrost calculations. For this reason, not only are the data averaged over the last five years of the simulation, but they are also split between the north and south hemispheres. The separation of the hemispheres is based on the month that contains the warmest subsurface temperatures and least soil ice content (November in the north and April in the south). By choosing these months, it eliminates annual variability and ensures that only the permafrost that is truly perennial is considered in further calculations.

2.5.2 Biome4 Output

In order to ensure that the most equilibrated version of the biome output is used the vegetation data is based on the last year of the simulation. Less importantly, it becomes a small programming challenge when averaging the vegetation data. This is due to the arrangement of the 28 biomes and the fact that, for example, the 11^{th} biome type

may not at all be related to the 12th biome type. If, from year 30 – 35, the biome of a cell that is averaged has changed, the resulting mean value of that cell may not reflect an appropriate biome.

2.6 Gridded Area Matrix

A substantial portion of this project entailed creating/executing calculations of permafrost area from the model simulations. To make these permafrost area calculations, a gridded-area 2-D array to represent the area of the Earth per 2° x 2° grid cell was developed. GENESIS does not produce a gridded area file that contains the area per grid cell for all 16,200 grid cells. Careful consideration had to be taken when generating this array for two reasons. First, the Earth is not a perfect sphere, with a radius of 6,378.1 km at the equator and 6,356.8 km at the poles. If one of these radiuses were arbitrarily chosen it would result in an area bias and over/under estimation of either the equator or poles depending which radius was chosen. Second, because GENESIS bases the model grid cells on the latitude and longitude of Earth, the areas per grid cell become smaller as latitude increases. The first step was to determine an accurate surface area of the planet; a generally accepted surface area of the earth is 510,072,000 km^2. An equation was found on an Internet math forum (http://mathforum.org) that successfully handled calculating global area from latitude and longitude and was easily convertible into a MATLAB program. This equation was tested via a multistep, degree-based validation process which indicated that the equation was able to produce consistent results regardless of model resolution (0.5°x0.5° through 5°x5° tested).

Equation 2.3: Area per grid cell

$$\frac{\pi}{180} \bullet R^2 \bullet [\sin(lat1) - \sin(lat2)] \bullet [lon1\text{-}lon2] = \text{Area per grid cell}$$

The above equation (Equation (Eq) (2.3)) was then modified to match the 2° x 2° resolution of GENESIS and a correct ($\pi/180 * R^2$) constant was calculated.

Equation 2.4: Area per grid cell with calculated radius

$$708{,}433.333 \bullet [\sin(lat1) - \sin(lat2)] \bullet [lon1\text{-}lon2] = \text{Area per grid cell}$$

It was calculated that a radius of 6,371 km would be required in order to have a total surface area as close as possible to the actual. When multiplied through ($\pi/180$) a constant of 708,433.3333 is produced. The original equation was designed to calculate the area for a one-degree of latitude by one-degree of longitude grid. This equation was tested numerous times and it consistently produced a global area of 510,071,999.99 km^2 (this number equaling the summed total of all the individual grid cells).

In order to validate the model land surface area, a value which is important in a study such as this as terrestrial area, more specifically vegetated terrestrial area, will have a large impact NPP and Rs output. The control simulation produced a current day terrestrial area of 160,118,417 Km^2. This is ~12 million square kilometers too large. This result is likely due to the coarse resolution of the model (2°x2°) and the model's inability to precisely differentiate between the land-sea boundary resulting in an area that is too large. The terrestrial areas per grid cell were adjusted by ~7.1% in order to produce a

global terrestrial area of 148,846,993 Km^2. This accepted global terrestrial area is 148,847,000 Km^2 (Van der Leeden *et al.* 1990).

The PETM Topography file produced a terrestrial area of 126,464,192 Km^2. This is ~22.4 million square kilometers less than modern day terrestrial area due to the higher Eocene (ice-free) sea level. This will impact low CO_2 (500 ppm) NPP and Rs results due to the reduced area in which terrestrial biomass can form.

2.7 Calculating Permafrost Area

GENESIS does not contain permafrost as a subsurface variable. For this reason the area of permafrost is calculated via a subsurface temperature variable (T6). T6 displays the least amount of annual variability and is below the freeze-thaw active layer. As previously noted, permafrost is defined as subsurface Earth materials remaining below 0°C for two consecutive years (Schuur *et al*., 2008). To calculate the permafrost area, one criteria has to be satisfied, the region measured must be below 273.15 K for a minimum of two years. Originally the permafrost was calculated from the soil ice content, yet, the definition of permafrost specifically states temperature and makes no mention of ice and therefore the method was discontinued.

To calculate the permafrost area a script was written that scans the split hemisphere averaged T6 file for all grids with a temperature below 273.15 K (0°C). If a cell below freezing is located, the gridded area matrix is accessed and the same cell location of the T6 file is pulled from the area matrix file and placed into a new matrix. There is no fractionalization of the gridded area. If a cell is below freezing the entire cell area is then added to the permafrost area matrix. The total areas are split into 3 groups:

Southern Hemisphere, Northern Hemisphere, and total global area. This allows for the isolation of Antarctica for further analysis.

2.8 NPP and Rs Preliminary Calculations

2.8.1 NPP

The calculation of NPP in BIOME4 is based on a set of equations developed by Haxeltine and Prentice, 1996 then adopted for the various versions of BIOME. Haxeltine and Prentice, 1996 note that NPP by terrestrial ecosystems is proportional to absorbed photosynthetically active radiation (APAR) on a seasonal and annual basis. Haxeltine and Prentice, 1996 utilize standard formulations representing the instantaneous response of leaf net photosynthesis to APAR to show that the optimized canopy net photosynthesis is proportional to APAR. This approach results in reasonable values for the maximum (unstressed) light-use efficiency (LUE) of gross and net primary production of C_3 plants. The formulas implemented to complete the above referenced GPP and NPP relationship ship to LUE calculations can be found in Haxeltine and Prentice, 1996.

In order to validate the NPP dataset, a modern global value must be determined. The IPCC AR4 (Chapter 7, Pg 515) states an estimated terrestrial flux GPP ~120 PgC/yr. Zhang *et al.,* 2009 found that NPP:GPP equaled ~0.52 based on a multi-parameter ecosystem investigation using 2000-2003 MODIS data. With a ratio of 0.52, global terrestrial NPP is calculated to be 62.4 PgC/yr based on the 120 PgC/yr IPCC GPP estimate (Jones *et al.,* 2005, Prentice *et al.,* 2001). Due to the complexity of calculating NPP, terrestrial global totals vary approximately 30 PgC/yr (~+/- 15 PgC/yr from the mean) (Doughty *et al.,* 2010). This uncertainty is in part due to a large annual variability

of GPP in northern South America, central Africa, and the southwest pacific island region (Beer *et al*., 2010). The control GENESIS-BIOME4 simulation raw NPP output produced a terrestrial mean global total flux of 83.9 PgC/yr. As previously noted, uncertainties may stem from model low-latitude precipitation and vegetation biases leading to larger average NPP per grid cell. In order to account for the various biases and adhere to modern day estimates, the model NPP output mean was multiplied by an appropriate correction coefficient of 0.7434 to produce a corrected NPP terrestrial global total of 62.4 PgC/yr. From the data created in an ecosystem biomass experiment by Lou and Zhou, 2008, it was derived that NPP:Rs is ~0.835. When comparing the control simulation NPP result of 62.4 PgC/yr to the Rs result of 74.0 PgC/yr, a variance of 0.837 is observed. This simple calculation assists in validating not only the modeled NPP and Rs in relation to modern day estimates, but also within the ratio constraints of the two parameters. For the goals of this research it is not only important to accurately estimate NPP and Rs but also retain the proper relationship between NPP and Rs throughout the various simulations.

In section 3.2.5 NPP and Rs are compared from south to north latitudinally to provide a better understanding of the NPP versus Rs global distribution. The data used in that comparison are standardized by averaging the terrestrial NPP and Rs per 2° of latitude. This effectively removes biases due to increased land area per band of latitude. This produces a north to south NPP cross section that is not influenced by latitudinal land mass. When a plot with NPP and Rs is produced, the areas with net gain or loss of carbon to the subsurface is easily seen. Sections 3.2.3 and 3.2.4 discuss global NPP and Rs output.

When performing a simple calculation where the NPP or Rs per grid cell is converted from $g/m^2/yr$ to $g/km^2/yr$, multiplied by the area of the grid cell, then the terrestrial grid cells are summed to produce a global total flux a latitudinal bias is observed. The low latitudes produce the highest NPP and Rs output due to increased biomass, increased temperatures, and increase precipitation. The increased parameters coupled with the large area per grid cell has the affect of dwarfing the output of the high latitudes and creating unrealistic global totals. In order to correct for this issue, a global NPP or Rs mean is used then multiplied by the individual grid cell areas. This has the effect of removing the latitudinal bias and produces an overall more accurate global total per simulation, with land area having more of an impact on the overall output versus the NPP or Rs produced in a specific grid cell. In order to retain the ability to accurately discuss individual continental totals (i.e. Antarctica), a more direct approach is used.

2.8.2 Rs Calculation

Several attempts at calculating soil respiration (Rs) are provided in this section. Typically, simple Rs models either utilize annual (Raich *et al.,* 1995) temperature and precipitation or a linear relationship between Rs and NPP. When calculating Rs via an NPP relationship, the output is either net positive or negative. This guarantees an output that is either higher for every grid cell than the associated NPP, or lower for every grid cell than the associated NPP. The dynamics one would hope include are absent, which don't allow for Rs to act in a realistic manner. Producing an output that will closely mimic actual global Rs estimates requires a model that will utilize various other model outputs such as temperature and precipitation. Raich and Schlesinger (1992) evaluated

six Rs models that utilize temperature (T, °C) and precipitation (P, mm). Of the six models the two with the highest r^2 values are used.

Equation 2.5: Soil respiration equation 1

$$Rs = (9.26T) + (0.0127TP) + 289$$

Equation 2.6: Soil respiration equation 2

$$Rs = (9.88T) + (0.0344P) + (0.0112TP) + 268$$

Where T is mean annual air temperature in °C, P is mean annual precipitation in mm/yr, Rs is equal to soil respiration in (PgC/yr). Each equation produces an $r^2 = 50$. The BIOME4 control simulation yields 68.23 PgC/yr (Equation (Eq) 2.5) and 70.37 PgC/yr (Eq 2.6) respectively. This is a difference of ~3% from observations. As with the NPP output, the Rs data are validated to the accepted annual global estimate of ~74 PgC/yr (Bahn *et al.* 2009). Bahn *et al.,* 2009 found annual global Rs to lie with 68 to 80 PgC/yr (74 PgC/yr +/- 6 PgC/yr). The accepted global value is then divided by the model result to produce correction factors of 1.0846 (Eq 2.5) and 1.0516 (Eq 2.6). Each yield a result of ~74 PgC/yr. Both offline Rs models produce uncorrected results within the known error of Rs, however, due to the lower correction factor needed to achieve the exact value of 74 PgC/yr, Eq (2.6) is utilized here.

A third attempt was made to calculate Rs from a series of analog data sets compiled from around the world. Bond-Lamberty and Thomson (2010) published an Rs data set containing 730 observed locations spanning 98 biomes from all over the world. The data were imported into excel and then filtered by putting equivalent biomes into categories. Incomplete data points were removed. Once all 730 observed locations were correlated to a BIOME4 biome type, the data were then averaged to produce a single Rs

data point to correlate to the BIOME4 biome that it represented. This approach, however, required an impractical amount of tuning to produce a realistic result. The method was discounted as a realistic means for calculating global Rs.

For Rs global and continental total estimates, please refer to section 2.8.1 for methodology.

CHAPTER 3

RESULTS

3.1 Control Simulation

3.1.1 Permafrost and Temperature

In order to test the validity of the soil model's ability to accurately simulate subsurface ground temperature, the control simulation was compared to modern day permafrost conditions. This test provides confidence in the later calculations where observed data are not available. The control simulation yielded an area of 23,719,230 km^2. The modern permafrost area, as calculated by the International Permafrost Association (IPA), yields an area of ~$23x10^6$ km^2. This result only takes into account the T6 grid cells that are below 273.15 K with no additional parameters or tuning. The land surface below the Greenland and Antarctic ice sheets were ignored in the calculations for a more accurate result (i.e. no permafrost in icesheet-covered regions). Figure (Fig 3.1) is a comparison between the observed circumpolar northern permafrost extent and the control simulation permafrost extent. The model captures the entirety of the permafrost extent accurately, with a slight underestimation in southern Canada and Alaska. This is balanced by an overestimation in regions of south-central Eurasia and in Finland. The slight redistribution may be a result of the model's coarse resolution inability and to confine the details of the global topography. Upon inspection of the two meter annual surface air temperature output versus the T6 temperature output (Fig 3.2), the surface air temperatures in the regions of southern Canada and Alaska are below freezing, however,

this temperature does not seem to translate to below breezing temperatures for the lowest layer of the soil column. This is likely due to the duration of the below freezing air temperatures and the inability for the surface temps to remain below freezing during the warmest months of the year (resulting in non-perennially frozen ground).

A

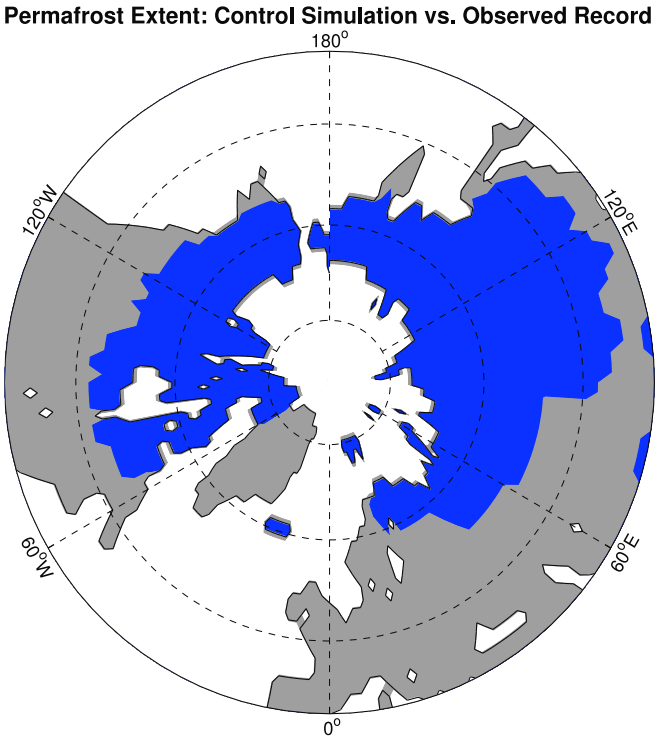

B

Figure 3.1: Comparison of the control simulation northern circumpolar permafrost extent to modern day observations.
Plot A (blue/grey) represents the control simulation run in GENESIS. The grey area represents land area while the blue region represents modern modeled permafrost extent. Plot B represents modern observed permafrost extent. The brown of the lower plot represents land while the various shades of purple represent permafrost extent (Schuur *et al*., 2008.).

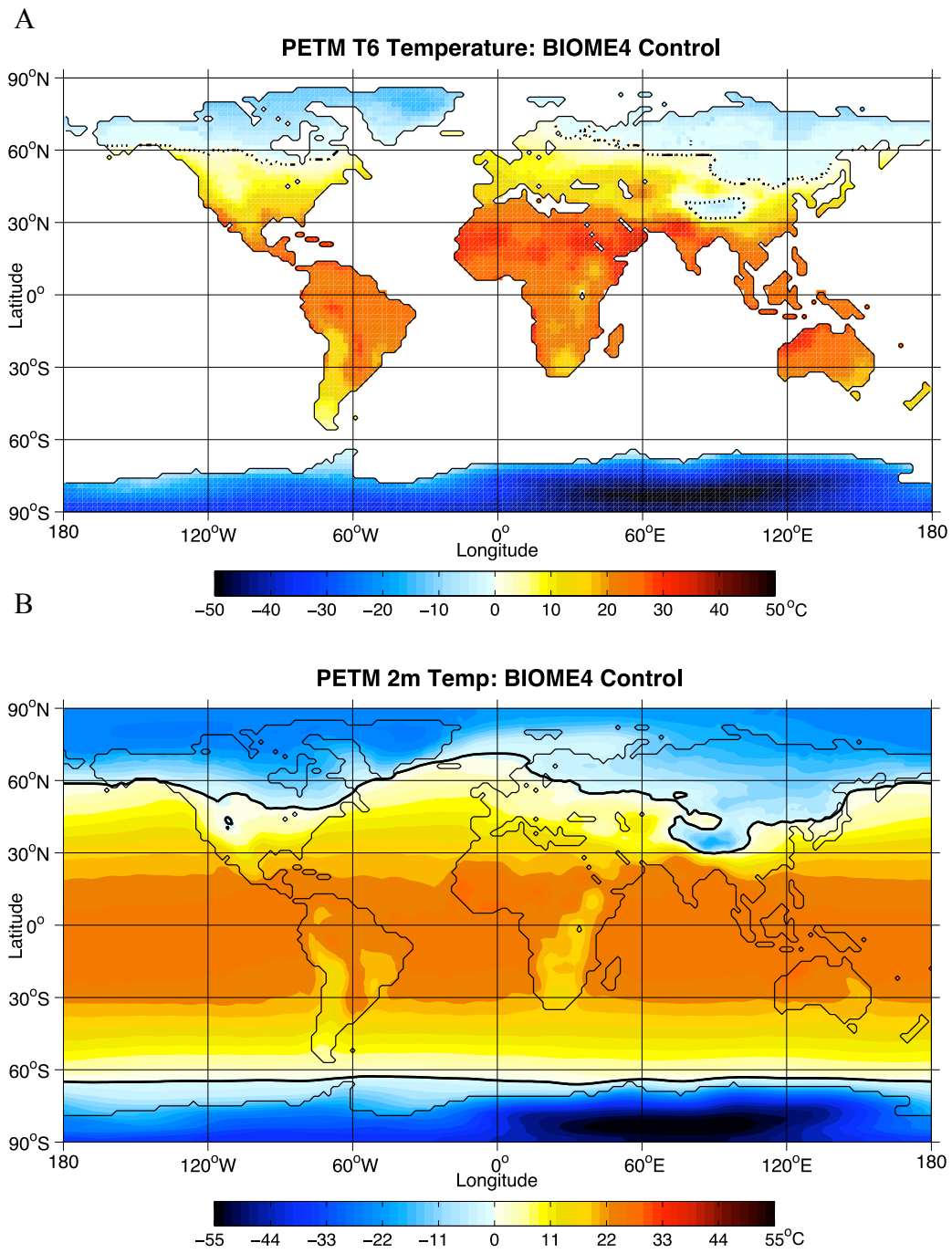

Figure 3.2: Comparison of temperature between the control simulation deepest soil layer (T6) and the control simulation 2-meter atmospheric temperature. Plot A displays the subsurface soil temperature of soil layer six (T6). The dotted line represents the 0°C boundary. Plot B displays the 2-meter annual air surface temperatures. The solid bold black line of the lower plot represents the 0°C boundary. There is a distinct difference, especially in the Northern Hemisphere, between the annual surface air temperatures and the subsurface soil temperatures.

3.1.2 Permafrost and Vegetation Distribution

The type of biomes that are present in permafrost regions determines total amount of carbon sequestered or released annually. In the control simulation biome types (Table 3.1; Page 40) 10, 14, 15, 21, 22, 23, 24, and 25 are present within the permafrost region. Biomes 10, cool mixed forest, and 25, cushion-forbs lichen and moss, occupy the least number of grid cells. Biome 14, evergreen taiga/montane forest, occupies the highest number grid cells and is the dominant feature through Alaska, central Canada, and Northern Eurasia. Various forms of tundra cover the northern most extent of North America, north of Hudson Bay, and northern Siberia. The Himalayas are an interesting case due to the elevation differences between the valley floor and the high peaks. Although, in the permafrost region of the Himalayas, tundra and evergreen forest are present with cool mixed forest and cool conifer forest, type 11, occupying less than five grid cells.

Biome #	Biome Type	Color Key
1	Tropical evergreen forest	
2	Tropical semi-deciduous forest	
3	Tropical deciduous forest/woodland	
4	Tropical xerophytic shrubland	
5	Temperate xerophytic shrubland	
6	Tropical grassland	
7	Temperate grassland	
8	Temperate conifer forest	
9	Warm mixed forest	
10	Cool mixed forest	
11	Cool conifer forest	
12	Cold mixed forest	
13	Temperate deciduous forest	
14	Evegreen taiga/montane forest	
15	Deciduous taiga/montane forest	
16	Tropical savanna	
17	Temperate broadleaved savanna	
18	Open conifer woodland	
19	Temperate scierophyll woodland	
20	Boreal parkland	
21	Steppe trundra	
22	Shrub tundra	
23	Dwarf shrub tundra	
24	Prostrate shrub tundra	
25	Cushion-forbs lichen and moss	
26	Desert	
27	Barren	
28	Land ice	

Table 3.1: The BIOME4 biome key with color bar.
Each biome in BIOME4 is plotted utilizing a unique color code specific to an individual biome. This color scheme is modified from the Haxeltine and Prentice., 1996 BIOME3 biome color scheme.

A

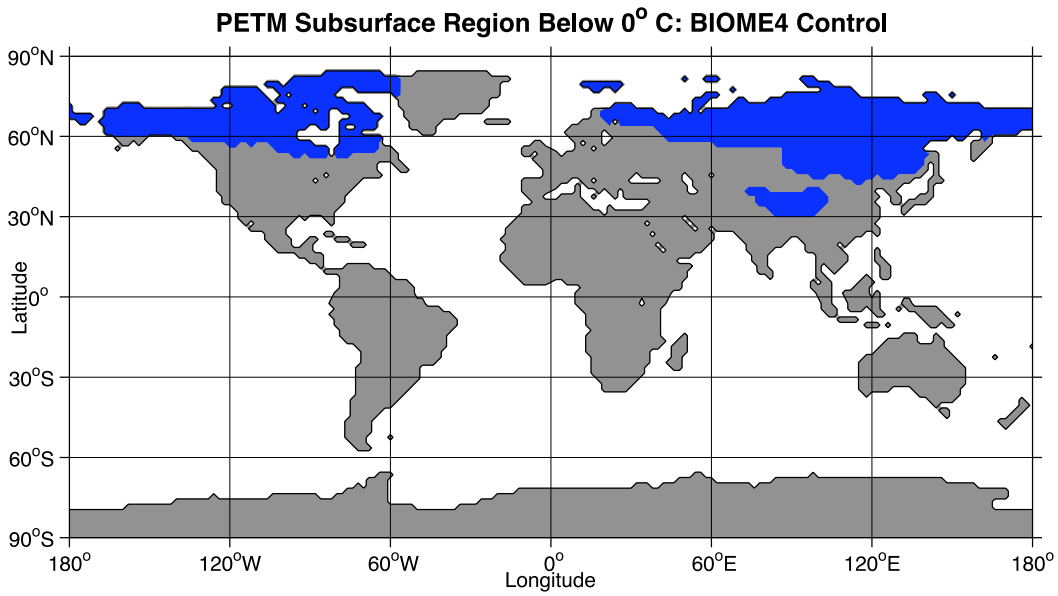

B

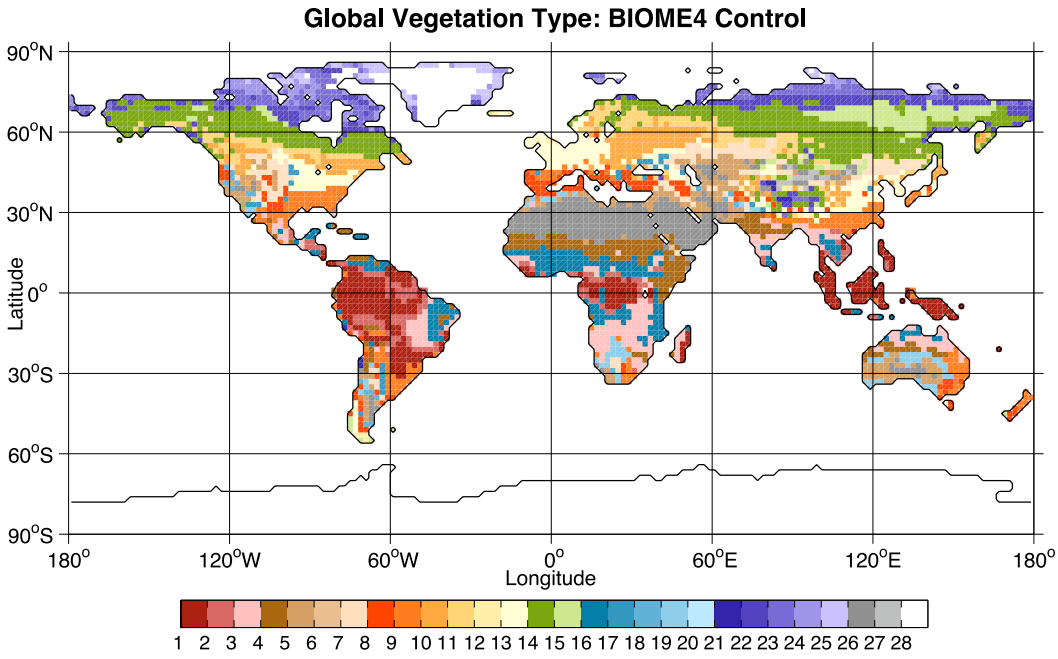

Figure 3.3: Comparison of the control simulation global permafrost extent to control simulation global vegetation.

Plot A displays an equidistant cylindrical projection of the control simulation permafrost extent. The grey represent non-permafrost covered land area while the blue represents the permafrost covered land area. Plot B displays the distribution of the 28 biome types for the control simulation as produced by BIOME4. In order to reference the biome names from biome number please see Table 3.1.

Exp.	CO_2 (eppmv)	CO_2 (ppmv)	MAT (ºC)	NH PF (10^6 km^2)	SH PF (10^6 km^2)	Tot. PF (10^6 km^2)
Cont.	400	355	14.65	23.72	-	23.72
1	550	500	18.31	19.47	11.77	31.24
2	900	750	20.3	12.04	10.31	22.35
3	900	750	20.58	7.24	9.7	16.94
4	900	750	20.63	5.82	9.7	15.52
5	900	750	20.92	5.77	9.21	14.98
6	1275	1000	22.39	1.59	8.27	9.86
7	2680	2000	26.3	0.45	1.33	1.78
8	5360	4000	30.31	0.11	.07	0.18

Table 3.2: Outline of experiments with CO_2, MAT, and hemispheric/global permafrost area.

Permafrost area varies per experiment. Exp. presents the experiment number with Cont. signifies the control simulation. CO_2 (parts per million by volume) states the atmospheric carbon dioxide concentration per experiment. The MAT states the Mean Air Temperature per simulation in degrees Celsius. The permafrost areas are slit into three categories: Northern Hemisphere (NH), Southern Hemisphere (SH), and total global area (Tot.). All areas are in millions of square kilometers (10^6 km^2). In runs 1-8, Antarctica is ice free and vegetated, allowing for permafrost to form.

3.2 Experiments 1 - 8

Experiment 1-5, represent pre to early onset PETM conditions. With the coolest temperatures produced of all the PETM simulations, experiment 1 displays the largest permafrost extent. The vegetation distribution in experiment 1 most closely matches the control simulation in terms of zonal distribution. In the subsequent simulations the permafrost area is reduced and the biome distribution changes in response to the warmer climates.

3.2.1 Permafrost Extent

3.2.1.1 Experiment 1

With the addition of the larger Antarctica as a potential region for permafrost formation, the amount of global permafrost increases to 31.25 x 10^6 km^2 from the 23.72 x 10^6 km^2 of present day. All of Antarctica is permafrost covered (11.77 x 10^6 km^2 of permafrost) with the exception of two small regions located on the northern most tip of the Antarctica Peninsula and on the northwestern base of the Tasmanian land bridge, regions on Antarctica where permafrost appears to be correlated to low elevation areas. The Northern Hemisphere produced a permafrost area of 19.47 x 10^6 km^2 with nearly all of the land area north of 60° permafrost covered with only the high elevation below 60° N containing permafrost.

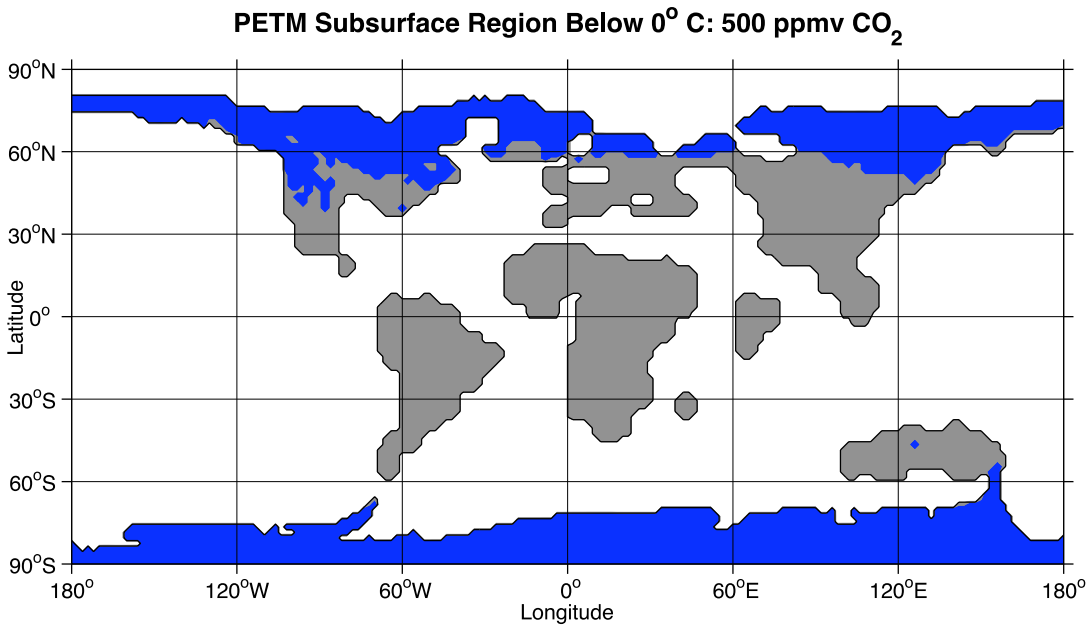

Figure 3.4: 500 ppmv CO_2 simulation permafrost extent based on subsurface temperature of soil layer T6.
The blue represents regions that contain permafrost. The grey represents permafrost-free land area. Experiment 1 (500 ppmv CO_2) yield 31.24 x 10^6 km^2 total permafrost area with 11.77 x 10^6 km^2 in the Southern Hemisphere and 19.47 x 10^6 km^2 in the Northern Hemisphere.

3.2.1.2 Experiment 2

The 750 ppmv CO_2 neutral orbit simulation produced a total permafrost area of 22.35 x 10^6 km^2 with 10.31 x 10^6 km^2 in the Southern Hemisphere and 12.04 x 10^6 km^2 in the Northern Hemisphere. The Northern Hemisphere shows permafrost degradation between 0 and 60°E along the 60°N line of latitude. The high elevation permafrost regions below 60°N are largely reduced. The once continuous permafrost region in southern North America is now sporadic and large regions void of permafrost have appeared northwest North America as well as in northeastern North America. The perimeter of Antarctica is also seeing signed of degradation with large portions of the coastline permafrost free. The Northern Hemisphere appears more sensitive to initial increases in GHG concentrations compared to the Southern Hemisphere. This Northern

Hemisphere bias is likely due to the increase terrestrial area and lower latitude of the land mass in the Northern Hemisphere versus the Southern Hemisphere.

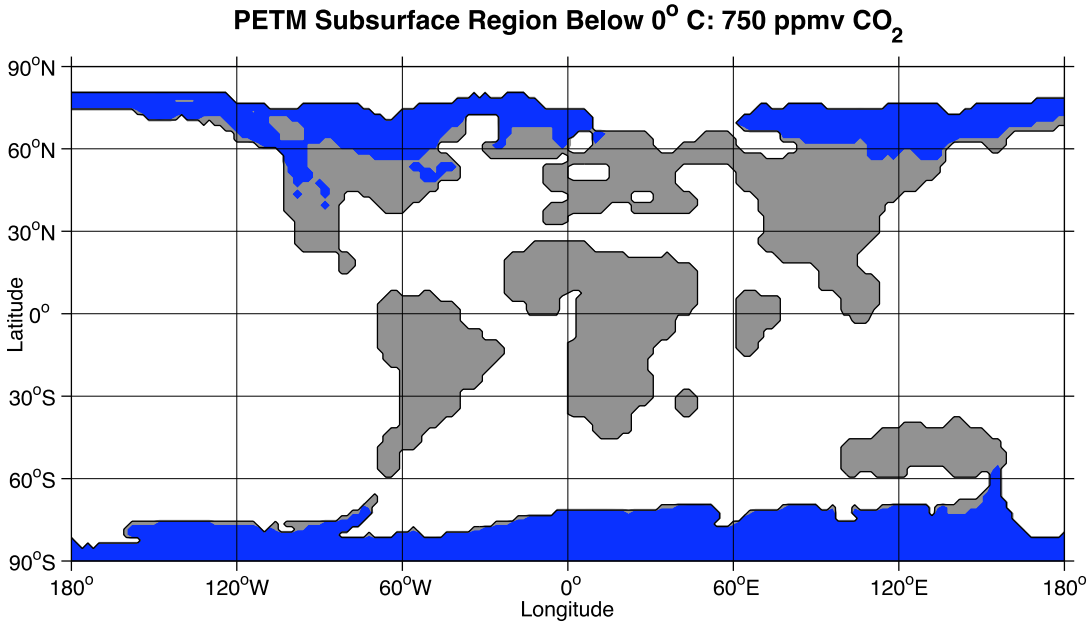

Figure 3.5: 750 ppmv CO_2 neutral orbit simulation permafrost extent based on subsurface temperature of soil layer T6.
The blue represents regions that contain permafrost. The grey represents permafrost-free land area. Experiment 2 (750 ppmv CO_2) yield 22.35 x 10^6 km^2 total permafrost area with 10.31 x 10^6 km^2 in the Southern Hemisphere and 12.04 x 10^6 km^2 in the Northern Hemisphere.

3.2.1.3 Experiment 3

The 750 ppmv CO_2 high obliquity (24.5° versus 23.5°) simulation was meant to test the influence of obliquity as a driving force of permafrost degradation. With an overall global reduction of 5.41 x 10^6 km^2 over experiment 2, experiment 3 yield 16.94 x 10^6 km^2 of permafrost with 9.70 x 10^6 km^2 in the Southern Hemisphere and 7.24 x 10^6 km^2 in the Northern Hemisphere. Antarctica remains largely unaffected by the increase in obliquity, however, the Northern Hemisphere displays permafrost loss through large regions of northwest North America and northern Siberia. The landmass northeast of North America also lost a majority of it's permafrost.

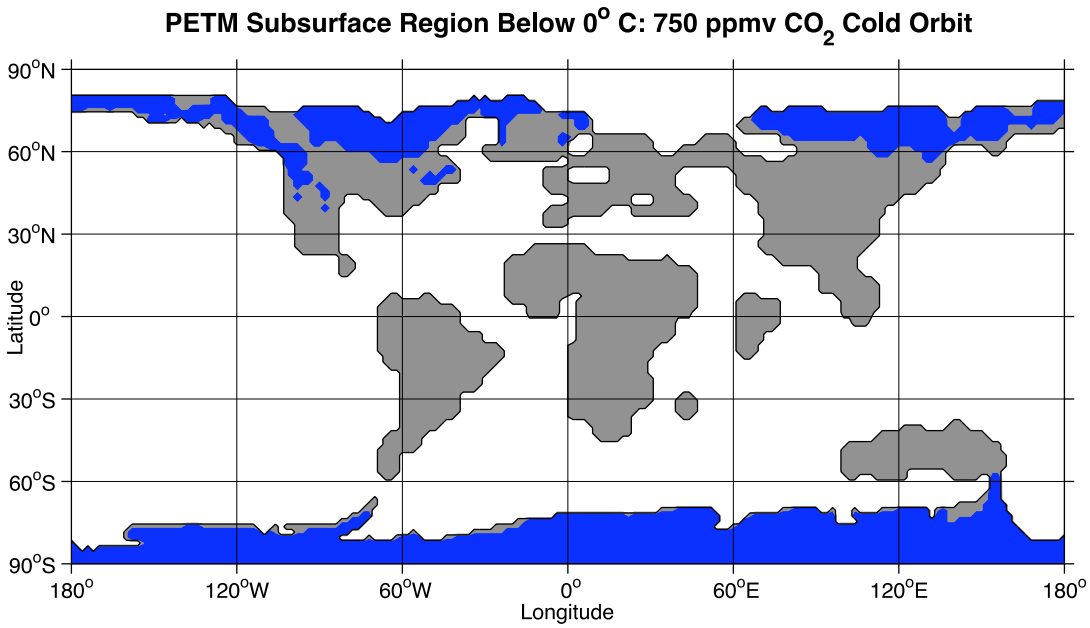

Figure 3.6: 750 ppmv CO_2 cold orbit simulation permafrost extent based on subsurface temperature of soil layer T6.
The blue represents regions that contain permafrost. The grey represents permafrost-free land area. Experiment 4 (750 ppmv CO_2 Cold Orbit) yield 15.52 x 10^6 km^2 total permafrost area with 9.70 x 10^6 km^2 in the Southern Hemisphere and 5.82 x 10^6 km^2 in the Northern Hemisphere.

3.2.1.4 Experiment 4

The 750 ppmv CO_2 cold orbit (0.05 eccentricity and 270° Precession) simulation tests the influence of eccentricity and precession as an orbital forcing factor for a cold orbit an or orbit where the Northern Hemisphere is angled towards the sun (summer solstice) during perihelion. The total permafrost area is 15.52 x 10^6 km^2 with 9.70 x 10^6 km^2 in the Southern Hemisphere and 5.82 in the Northern Hemisphere. This is a reduction of 6.83 x 10^6 km^2 over the neutral orbit simulation. Antarctica remains unchanged between experiments 3 and 4, however, the Northern Hemisphere of experiment 4 shows slight reductions in eastern North America.

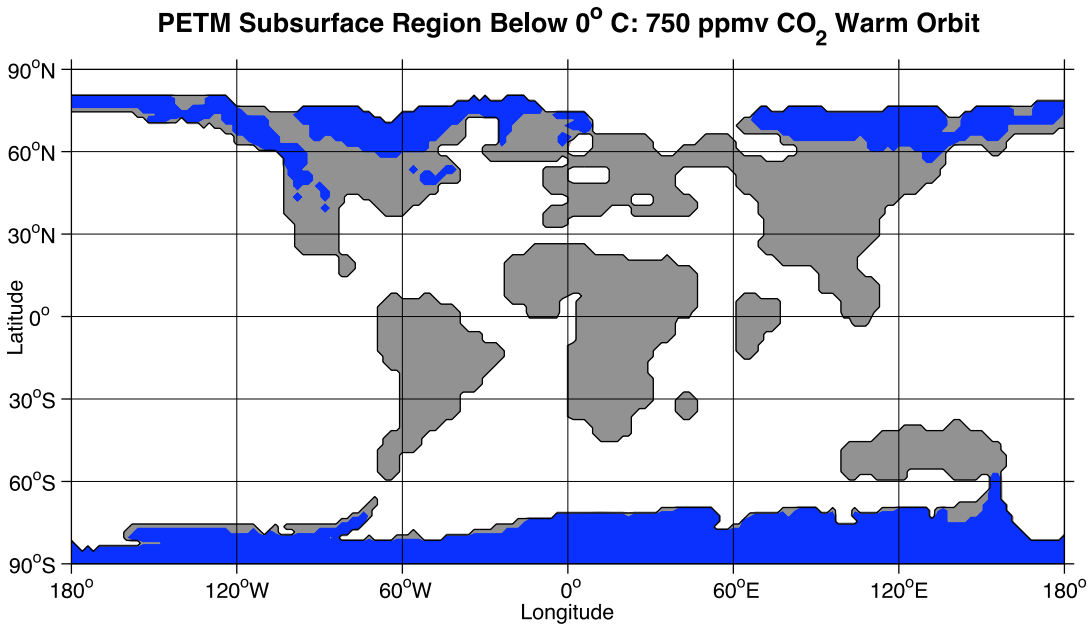

Figure 3.7: 750 ppmv CO_2 warm orbit simulation permafrost extent based on subsurface temperature of soil layer T6.
The blue represents regions that contain permafrost. The grey represents permafrost-free land area. Experiment 5 (750 ppmv CO_2 Warm Orbit) yield 14.98 x 10^6 km^2 total permafrost area with 9.21 x 10^6 km^2 in the Southern Hemisphere and 5.77 x 10^6 km^2 in the Northern Hemisphere.

3.2.1.5 Experiment 5

The 750 ppmv CO_2 warm orbital (0.05 eccentricity and 90° precession) simulation is designed to test the influence of the warm orbital situation. This simulation produced a total permafrost area of 14.98 x 10^6 km^2 with 9.21 in the Southern Hemisphere and 5.77 in Northern Hemisphere. The difference between experiment 4 and 5 is minimal, with both having nearly identical results. The warm and cold orbit had the most significant influence of the permafrost area. This orbital interaction between the neutral case and the warm and cold orbit cases is discussed in the following chapter.

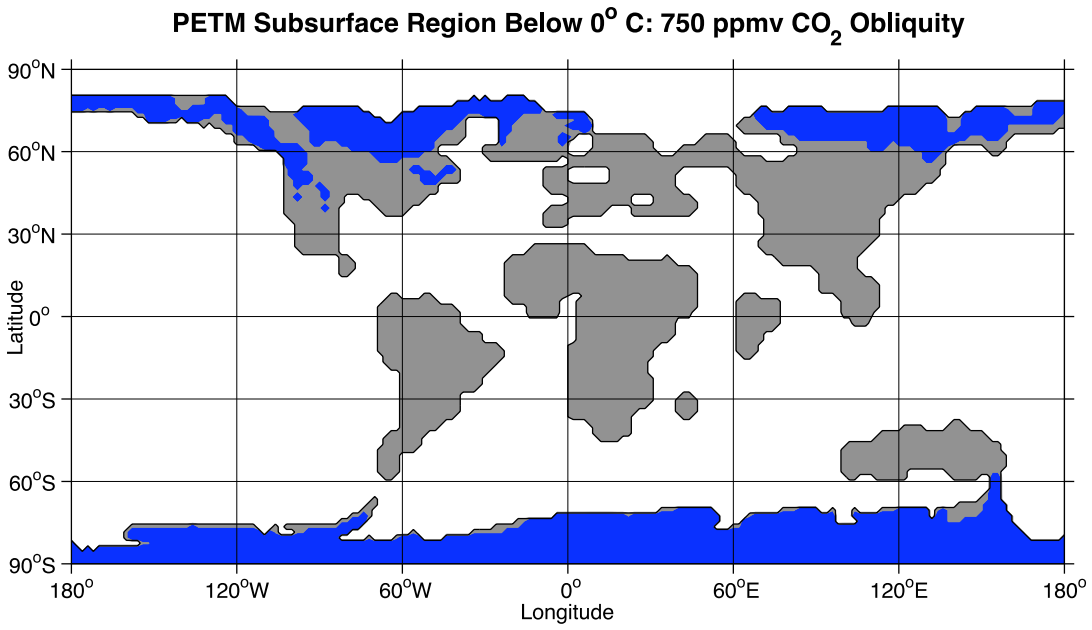

Figure 3.8: 750 ppmv CO_2 high obliquity simulation permafrost extent based on subsurface temperature of soil layer T6.
The blue represents regions that contain permafrost. The grey represents permafrost-free land area. Experiment 3 (750 ppmv CO_2 High Obliquity) yield 16.94 x 10^6 km^2 total permafrost area with 9.70 x 10^6 km^2 in the Southern Hemisphere and 7.24 x 10^6 km^2 in the Northern Hemisphere.

3.2.1.6 Experiment 6

The 1000 ppmv CO_2 neutral orbit simulation displays a permafrost area that is largely reduced with a total area of 9.86 x 10^6 km^2. The Northern Hemisphere is nearly permafrost free with only a few grid cells existing in eastern Siberia and small patches present in northeastern, western, and northwestern North America. Antarctica begins to see significant signs of permafrost degradation along the low-elevation regions around the perimeters of the continent, yet the interior remains widely unchanged.

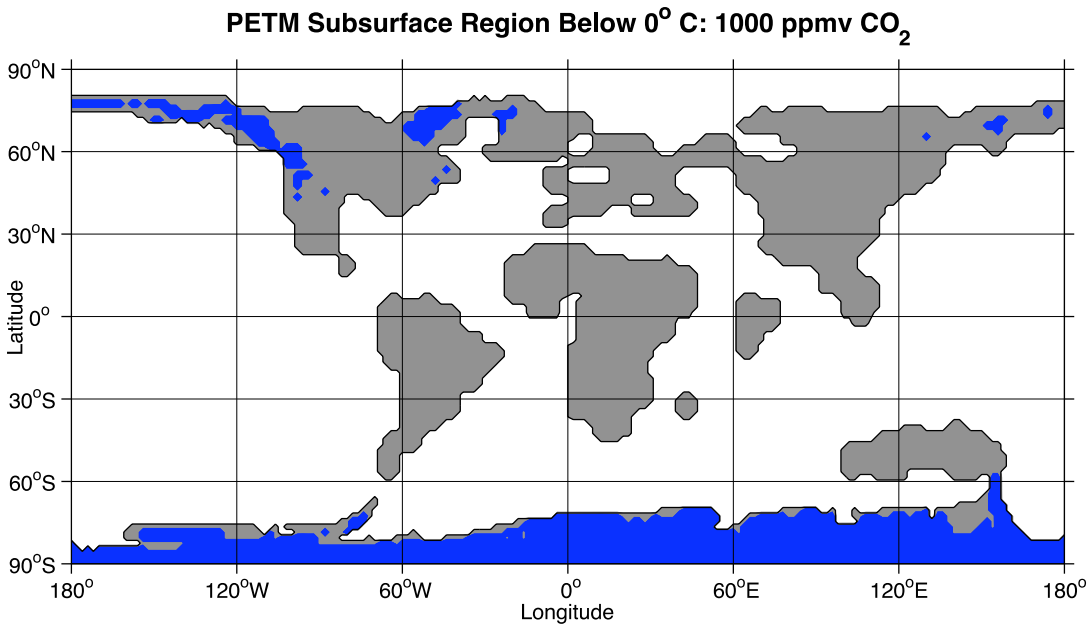

Figure 3.9: 1000 ppmv CO_2 simulation permafrost extent based on subsurface temperature of soil layer T6.
The blue represents regions that contain permafrost. The grey represents permafrost-free land area. Experiment 6 (1000 ppmv CO_2) yield 9.86 x 10^6 km^2 total permafrost area with 8.27 x 10^6 km^2 in the Southern Hemisphere and 1.59 x 10^6 km^2 in the Northern Hemisphere.

3.2.1.7 Experiment 7

The 2000 ppmv CO_2 neutral orbit simulation represents the mid point of the PETM carbon dioxide increase. In this simulation, the Northern Hemisphere is nearly permafrost free with only 0.45 x 10^6 km^2 of permafrost present at only the highest elevation in western and northwestern North America. The Southern Hemisphere produced an area of 1.33 x 10^6 km^2, which is 6.94 x 10^6 km^2 less than experiment 6. Between experiment 6 and 7, Antarctica lost most of its permafrost with sporadic patches remaining in the high elevations region only. The total area for experiment 7 is 1.78 x 10^6 km^2.

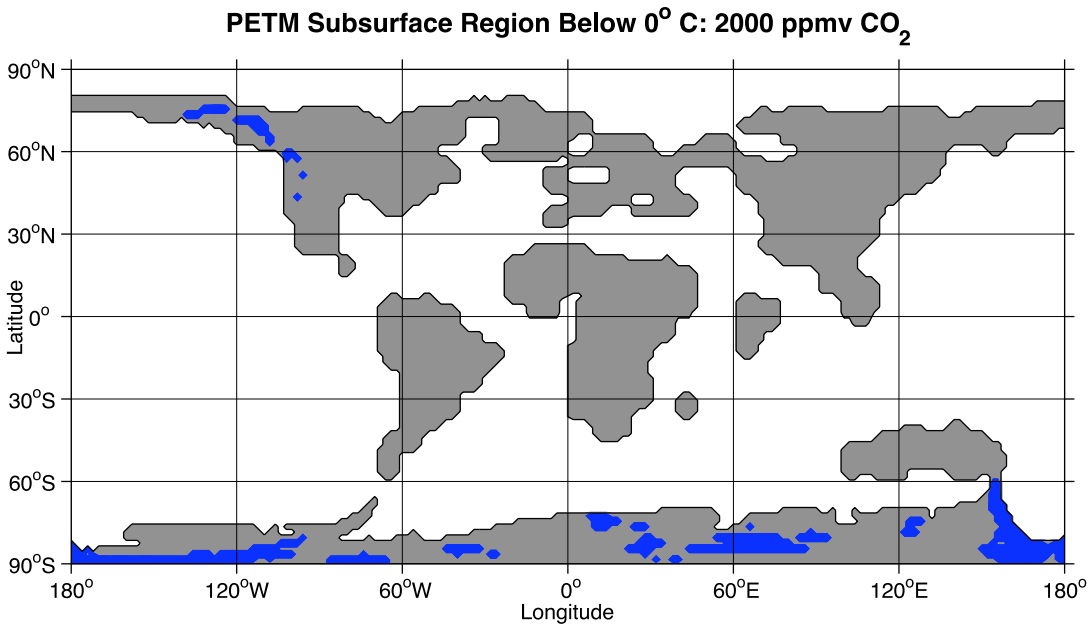

Figure 3.10: 2000 ppmv CO_2 simulation permafrost extent based on subsurface temperature of soil layer T6.
The blue represents regions that contain permafrost. The grey represents permafrost-free land area. Experiment 7 (2000 ppmv CO_2) yield 1.78 x 10^6 km^2 total permafrost area with 1.33 x 10^6 km^2 in the Southern Hemisphere and 0.45 x 10^6 km^2 in the Northern Hemisphere.

3.2.1.8 Experiment 8

The 4000 ppmv CO_2 neutral orbit simulation is beyond the apex of the PETM carbon dioxide increase. The total permafrost area is 0.18 x 10^6 km^2 with 0.11 constrained to North America and 0.07 sporadically located throughout Antarctica. The grid cells that produced this area exist at the highest elevation possible. Due to the location of the permafrost and the low likelihood that those regions could support permafrost or be a contributor to the carbon cycle, this simulation will be treated as an end member extreme case.

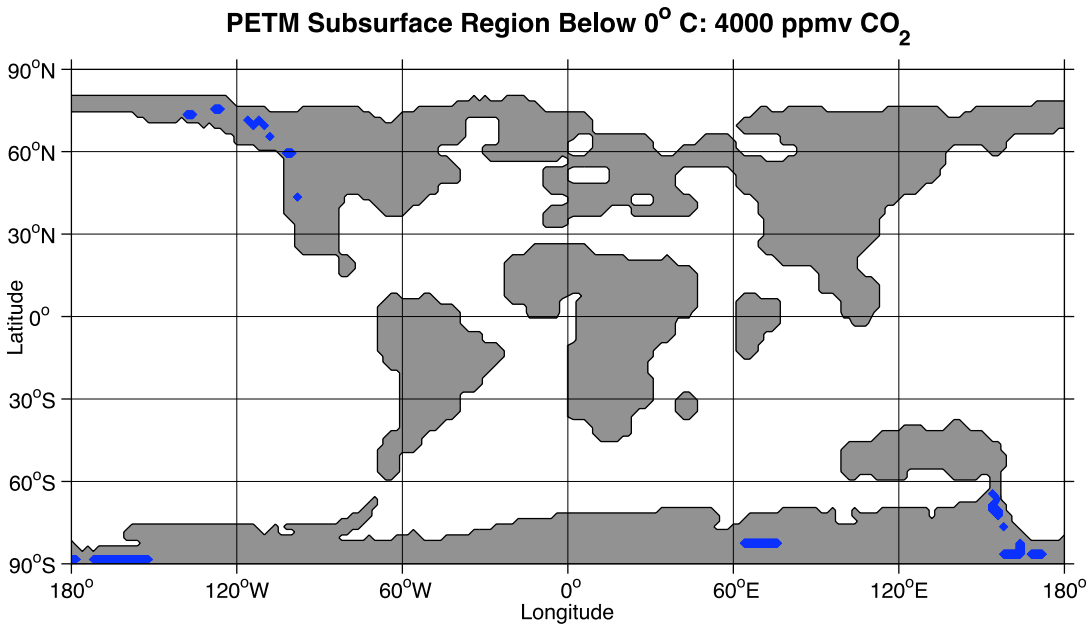

Figure 3.11: 1000 ppmv CO_2 simulation permafrost extent based on subsurface temperature of soil layer T6.
The blue represents regions that contain permafrost. The grey represents permafrost-free land area. Experiment 8 (4000 ppmv CO_2) yield 0.78 x 10^6 km^2 total permafrost area with 0.07 x 10^6 km^2 in the Southern Hemisphere and 0.11 x 10^6 km^2 in the Northern Hemisphere.

3.2.2 Vegetation Distribution

The vegetation distribution in the model simulations changes with every adjustment to the greenhouse gas concentrations and orbital parameters. Starting with experiment 2, the vegetation closely resembled the zonal distribution of the modern day climate. However, as the greenhouse gases were incrementally increased, the global temperature also increased. Vegetation that was once constrained to the tropics can now exist at higher latitudes. This, in a sense, pushed the vegetation that favors warmer temperatures to higher-latitudes. Eventually, the global temperatures increased to a point where the high latitude vegetation was nearly removed and tropical-like vegetation existed zonally worldwide.

In the following section the vegetation distributions are broken down per experiment in order to analyze the affects increased green house gases and extreme orbital parameters has on the biosphere.

3.2.2.1 Experiment 2 - 8

The zonal vegetation distribution of the 500 ppmv simulation (Figure 3.12) closely resembles the modern day zonal distribution. The predominant high latitude vegetation is evergreen taiga/montane forest (type 14). North central North America is split by tropical deciduous forest/woodland (type 3), which seems rather uncharacteristic given the cool temperatures. This may be a reflection of the high moisture and low elevation that allows for the formation of such biomes in these areas. Tundra is present (types 21, 22, 23, 24, 25) in the highest elevation regions of western and northwestern North America. Antarctica is fully vegetated in this run with evergreen taiga/montane forest covering a majority of the land surface. Deciduous taiga/montane forest (type 15) is placed sporadically across the continent with the various forms of tundra occupying the highest elevation. Tropical savanna (type 16) cover the low latitudes with tropical evergreen forest following the equator.

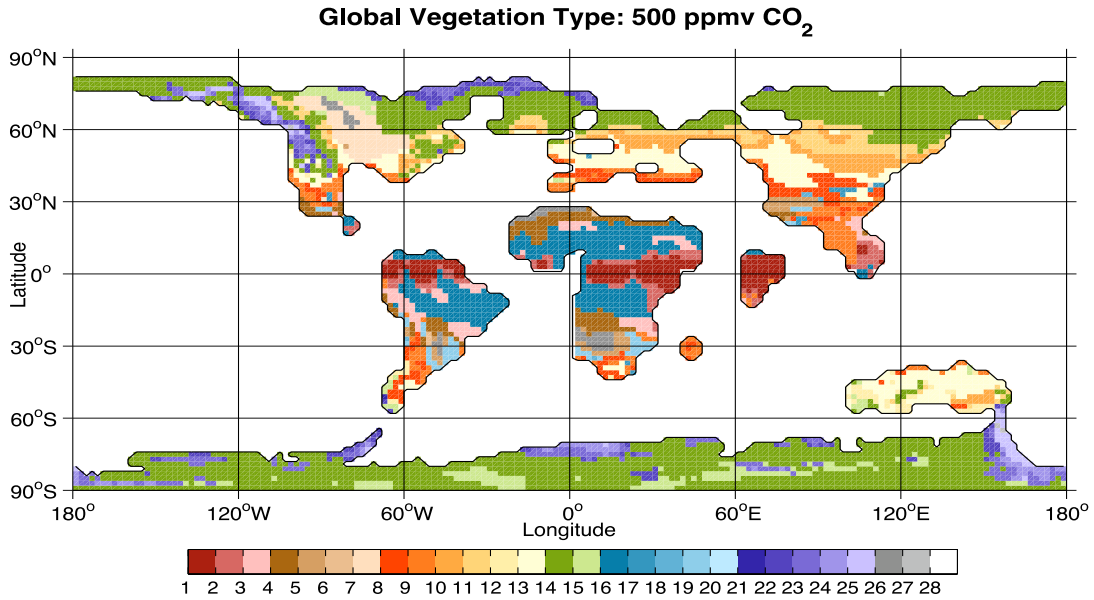

Figure 3.12: Vegetation distribution for the 500 ppmv CO_2 simulation. The 500 ppmv neutral orbit simulation displays a global vegetation distribution similar to the control simulation, however, the Antarctica is now fully vegetated. The predominant high latitude vegetation type is evergreen taiga/montane (Type 14).

The 750 ppmv neutral orbit simulation (Figure 3.13) closely resembles the 500 ppmv simulations, however, the biomes of the low latitudes have spread to the higher latitudes pushing the cool temperature vegetation further to the north and south. The change is subtle, with increase in green house gases displacing the zonal vegetation distribution by ~2° to the north and south. Permafrost that once existed along the parameter of Antarctica is now taiga/montane forest. In the 750ppm run, cool conifer forest (Type 11) and temperate grassland (Type 7) exist near the shore of Antarctica just east of 60°W.

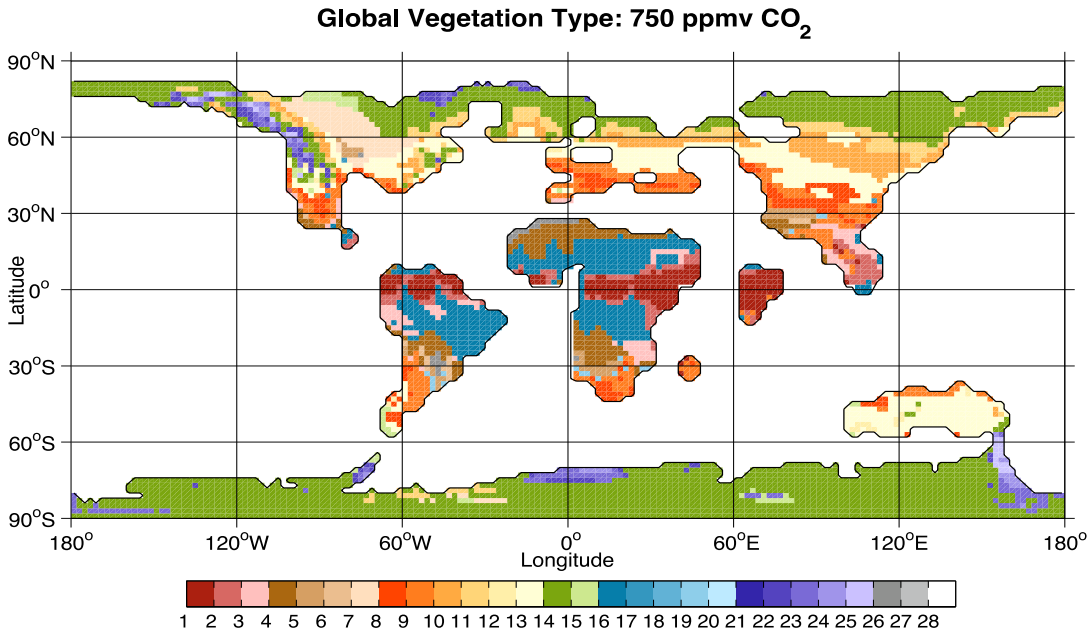

Figure 3.13: Vegetation distribution for the 750 ppmv CO_2 neutral orbit simulation.

The 750 ppmv neutral orbit simulation displays altered vegetation through north-central North America and Antarctica. Temperate grasslands (Type 7) have migrated north in North America and tundra is more confined on Antarctica. This represents the first step in the warm of the PETM.

The 750 ppmv cold orbit simulation (Figure 3.14) continues the northward migration of the low latitude to mid latitude vegetation types. Nearly all tundra type biomes are absent from the Northern Hemisphere with small regions only existing at the highest elevations. The evergreen taiga/montane biome that dominated the high north latitudes have nearly vanished. These are now covered by cool conifer forest (Type 11) and temperate grassland (Type 7). Antarctica remains largely unchanged from the 750 neutral orbit simulation.

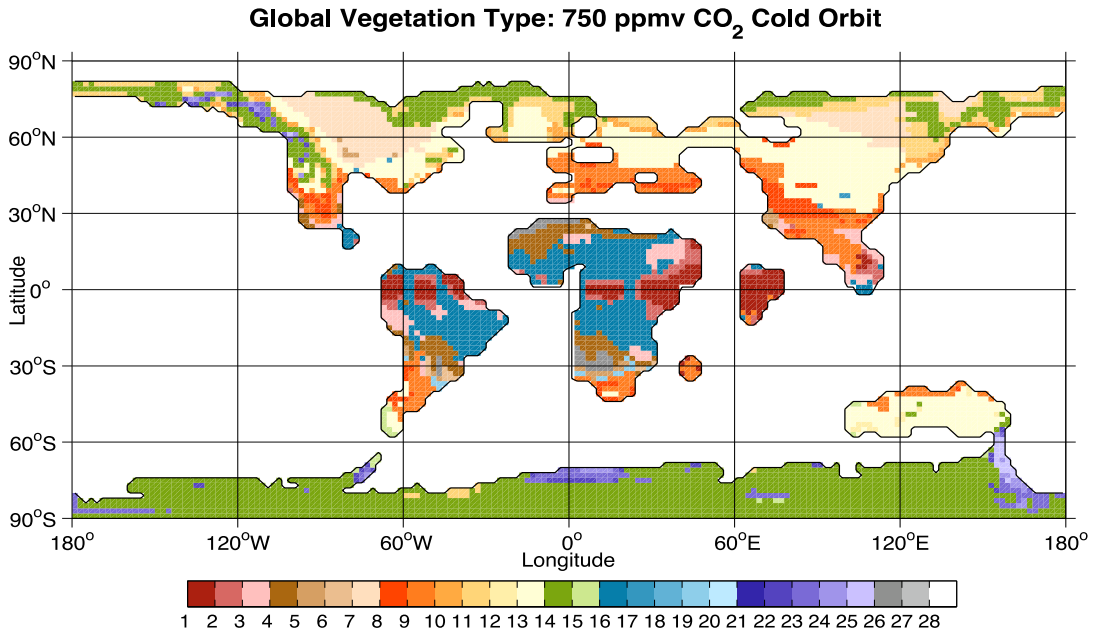

Figure 3.14: Vegetation distribution for the 750 ppmv CO_2 cold orbit simulation. The 750 ppmv austral cold orbit simulation displays significant changes in the vegetation distribution. Antarctica remains virtually unchanged while the Northern Hemisphere shows a loss of evergreen taiga/montane forest (Type 14) and an advance of temperate grasslands (Type 7), cool conifer forest (Type 11), and temperate deciduous forest (Type 13).

The 750 ppmv warm orbit simulation (Figure 3.15) results are opposite of the cold orbit. The Northern Hemisphere remains largely unchanged from the neutral orbit, however, the Southern Hemisphere, most notably Antarctica, shows huge alterations in the distribution of vegetation. From the coast just east of the Antarctic Peninsula to the far reaches of the interior, evergreen taiga/montane (Type 14) forest is replaced by temperate grasslands (Type 7). Tundra only exists in two locations and conifer forest (Type 11) is now more widespread than in the previous simulation. Both the warm (Figure 3.15) and cold orbit (Figure 3.14) 750 ppmv simulations show very similar results with respect to permafrost extent, however, the vegetation's response is nearly opposite. This is understandable when considering the orbital difference between warm

and cold orbits. An interesting point is that it does not matter what the orbital configuration is, warm or cold, because both display the same basic result regardless of the timing of perihelion.

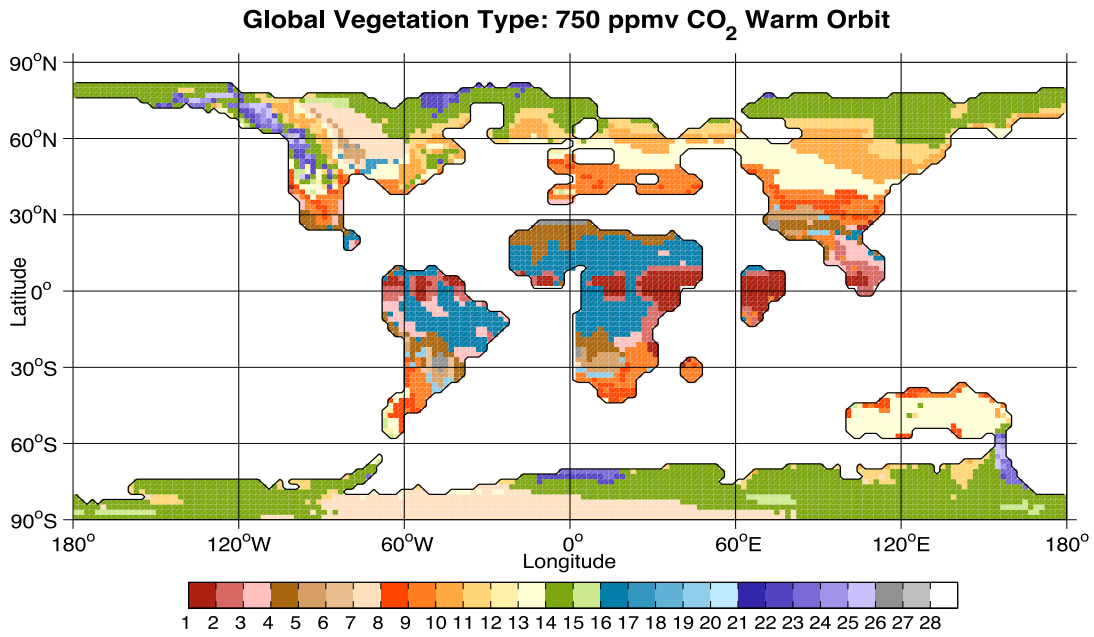

Figure 3.15: Vegetation distribution for the 750 ppmv CO_2 warm orbit simulation.

The 750 ppmv warm orbit simulation shows similar results for the Southern Hemisphere as the cold orbit does for the Northern Hemisphere. The Northern Hemisphere resembles the 500 ppmv simulation while Antarctica has a loss of evergreen taiga/montane forest (Type 14) and a widespread distribution of temperate grassland (Type 7).

The 750 ppmv high obliquity orbit (Figure 3.16) displays similar results to both the warm and cold orbit, but not as robust as either simulation. The effects are smaller due to the lack of eccentricity forcing. The Northern Hemisphere displays a slight northward migration of the low to mid latitude vegetation. The biomes that did advance north (and their distributions) are very close to the 750 ppmv cold orbit scenario, however, not to the same extent. The Southern Hemisphere shows very similar results, a situation that is close to the warm orbit simulation but with the same overall extent as the warm orbit. The high obliquity orbit shows substantial permafrost reductions over the 750 ppmv neutral orbit but lacks the end point extreme warming/vegetation displacement that is seen in the warm/cold orbits.

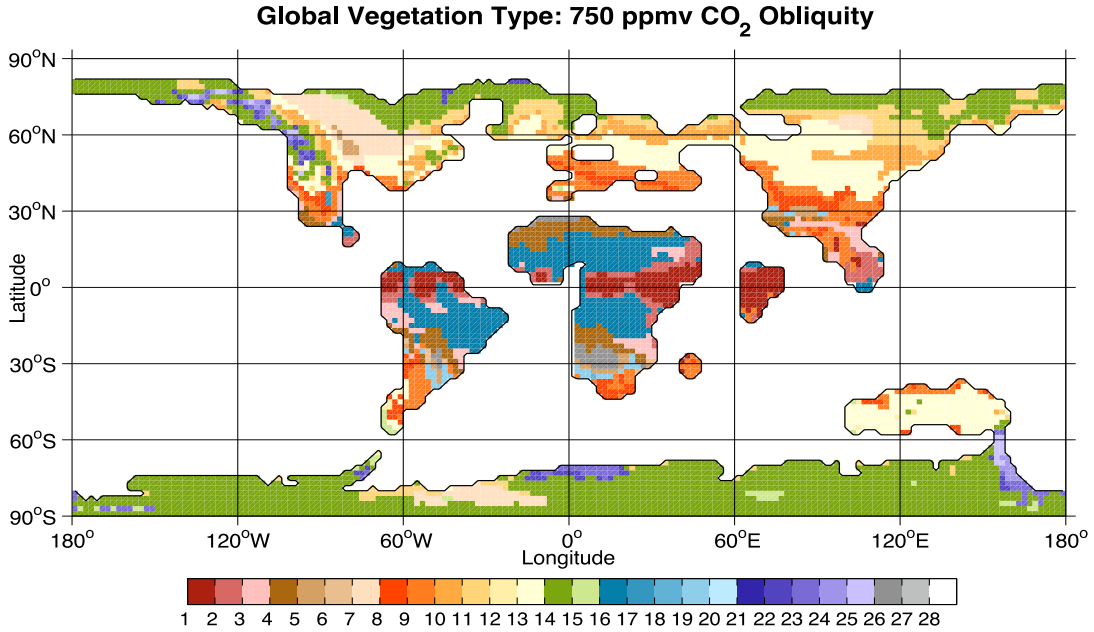

Figure 3.16: Vegetation distribution for the 750 ppmv CO_2 high obliquity simulation.
The 750 ppmv high obliquity orbit simulation displays a vegetation distribution with attributes similar to the 750 ppmv cold and warm orbit simulations. The northward migration of mid-latitude vegetation is present in the Northern Hemisphere as well as the introduction of temperate grasslands (Type 7) on Antarctica.

The 1000 ppmv neutral orbit (Figure 3.17) displays a large shift in the biodiversity in the Northern Hemisphere. Many vegetation types such as tropical xerophytic shrubland (Type 4), cool mixed forest (Type 10), and more widely spread temperate deciduous forest (Type 13). The evergreen taiga/montane forest is now only sporadically found throughout the highest land bearing latitudes and elevations. Only minor changes are seen on Antarctica with a larger distribution of cool conifer forest (Type 11), and the introduction of temperate deciduous forest (Type 13).

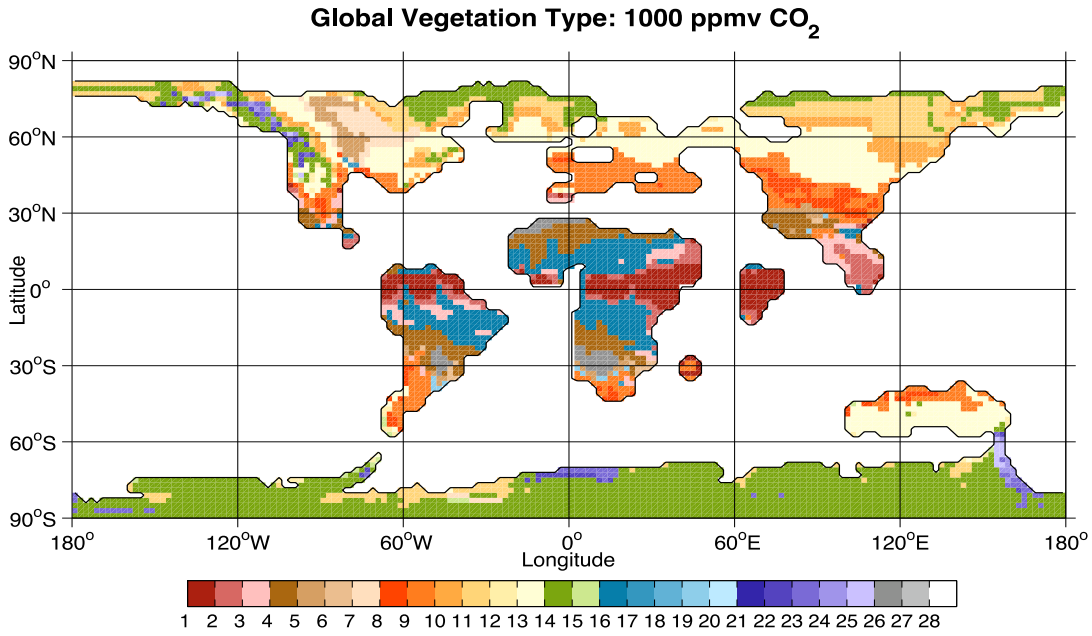

Figure 3.17: Vegetation distribution for the 1000 ppmv CO_2 simulation. The 1000 ppmv neutral orbit simulation displays large shifts in the Northern Hemisphere vegetation distribution in comparison to lower CO_2 simulations. The dominant vegation types are cool mixed forest (Type 11), temperate deciduous forest (Type 13), and evergreen taiga/montane forest (Type 14). Antarctica remained vastly unchanged from earlier simulations.

The 2000 ppmv simulation (Figure 3.18) displays the largest shift in global vegetation yet. The dominant global vegetation types are temperate deciduous forest (Type 13), Tropical xerophytic shrubland (Type 4), and warm mixed forest (Type 9). Tropical evergreen forest (Type 1) spans the equatorial region with small bands of tropical semi-deciduous forest (Type 2) and tropical savanna (Type 16) in the latitudes just pole ward of the equator. Antarctica begins to show significant changes in vegetation type and distribution with temperate deciduous forest (Type 13), cool conifer forest (Type 11), and evergreen taiga/montane forest (Type 14) having a three way split in vegetation and distribution across the continent. Tundra now only exists in the highest peaks of North America and the mountain range through Tasmania.

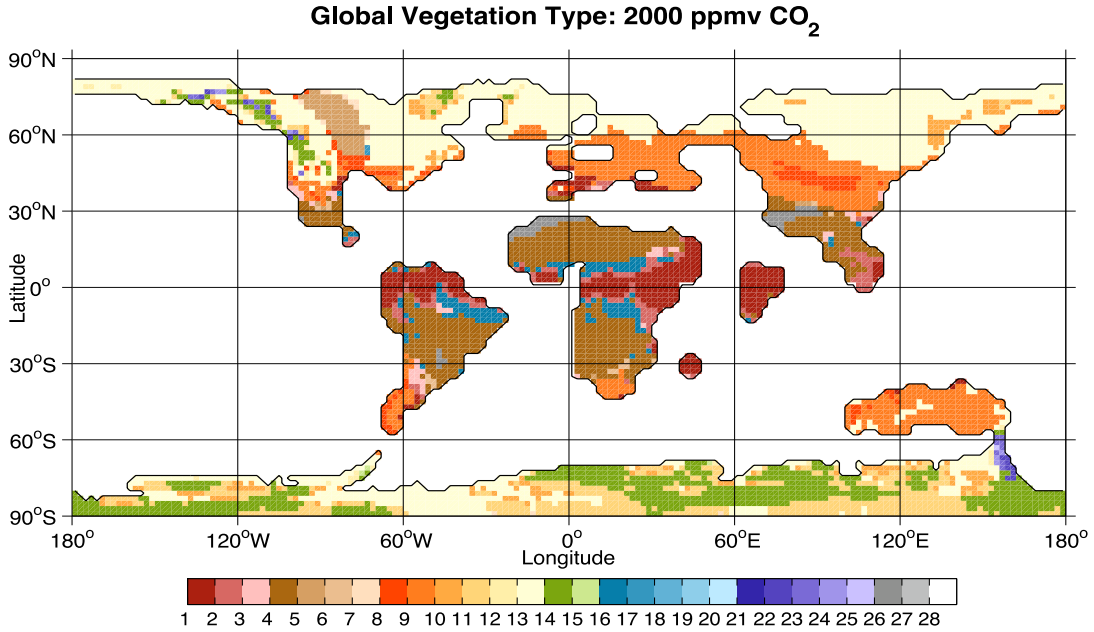

Figure 3.18: Vegetation distribution for the 2000 ppmv CO_2 simulation. The 2000 ppmv neutral orbit simulation shows significant global vegetation change. The dominant vegetations types are warm mixed forest (Type 9), temperate deciduous forest (Type 13), and tropical xerophytic shrubland (Type 4). Antarctica shows the first real signs of vegetation change with the reduction of evergreen taigi/montane forest (Type 14), which is replaced by cool conifer forest (Type 11) and temperate deciduous forest.

The 4000 ppmv neutral orbit simulation (Figure 3.19) represents the end point scenario for the PETM warming. The vegetation is zonally distributed based on type with Tropical evergreen forest (Type 1) running along the equator, Tropical xerophytic shrubland (Type 4) occupying the subtropical latitudes, with warm mixed forest (Type 9) occupying the northern mid to upper latitudes. A large portion of the northern latitudes as well as a majority of Antarctica is covered by temperate deciduous forest (Type 13). There are ~9 grid cells of tundra and ~50 grid cells of evergreen taiga/montane forest (Type 14) located at the highest elevations.

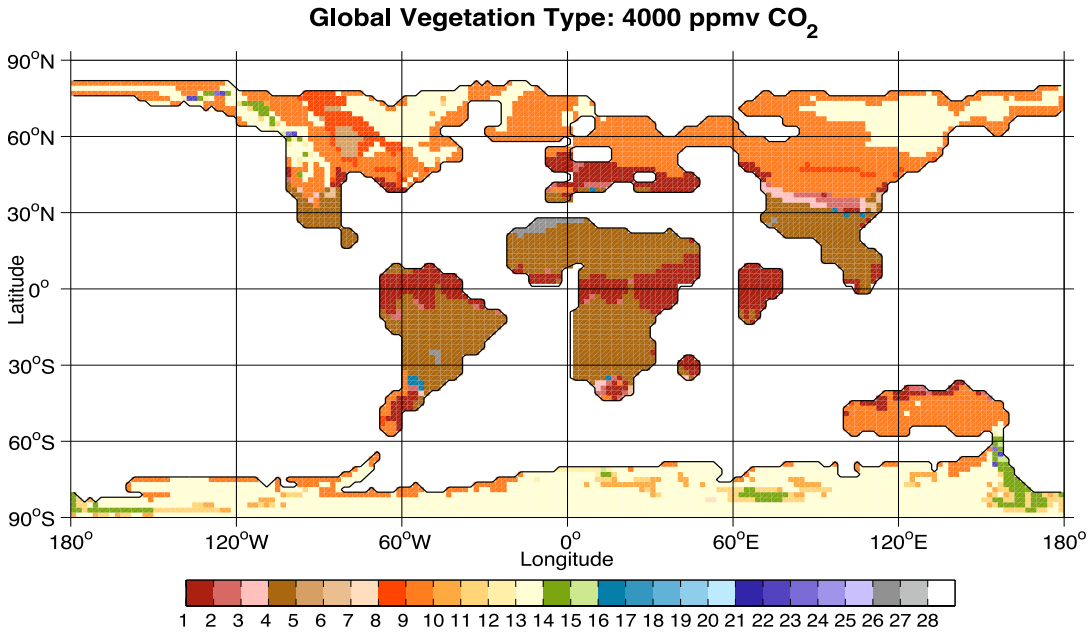

Figure 3.19: Vegetation distribution for the 4000 ppmv CO_2 simulation. The 4000 ppmv neutral orbit simulation displays the end point result of the PETM. Temperate climate vegetation has been replaced by tropical xerophytic shrubland (Type 4), warm mixed forest (Type 9), and temperate deciduous forest (Type 13).

3.2.3 Net Primary Production

The NPP output generated by BIOME4 is controlled by several main factors. Temperature, precipitation (driving soil moisture), and topography appear to be the three main driving forces behind NPP. NPP is controlled or represents terrestrial biomass, which is dependant on Atmospheric CO_2. As displayed in the control (Fig. 3.20), NPP is highest in lowlands of the equatorial region and lowest in the higher elevation and regions of low temperature and low precipitation. For methodology of calculating global and continental total estimates, please refer to section 2.7.1. All figures in this section display NPP model output in $g/m^2/yr$.

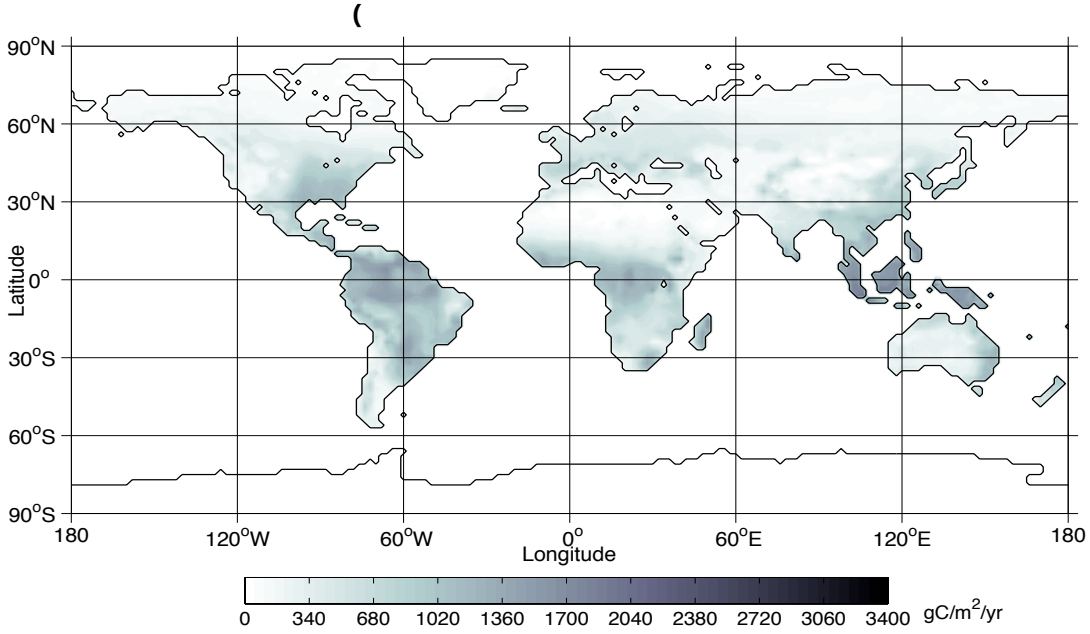

Figure 3.20: Global NPP for the control simulation
The NPP BIOME4 Control simulation displays the global output of NPP. The control simulation produced a global NPP total of 62.4 PgC/yr. The key features to note are the low elevation equatorial and high elevation polar values. NPP is greatly defined by temperature and precipitation.

The PETM model simulations are constrained to the same controlling factors as the control simulation except CO_2, however, Antarctica is now a key player elevating the

global NPP total. In the first CO_2 increase (500 ppmv neutral orbit– Fig. 3.21) from the control the global NPP decreases by 1.22 PgC/yr (total of 61.18 PgC/yr). The slight reduction on NPP is due to the reduced terrestrial area as described in Section 2.5. The NPP of Antarctica is ~2.21 PgC/yr (3.61% of total).

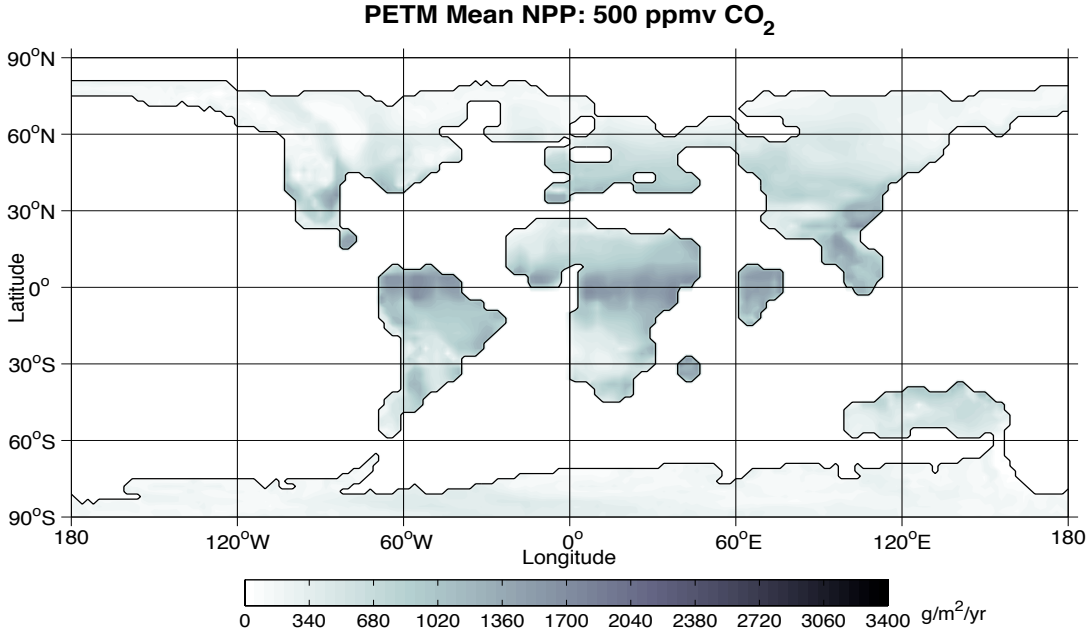

Figure 3.21: Global NPP for the 500 ppmv CO_2 simulation
The 500 ppmv neutral orbit simulation incorporates Antarctica as a key player in the global NPP contribution. The highest values are constrained to regions of high temperature/precipitation while the low values are found in regions of low temperature/precipitation. In this simulation, Antarctica produced 2.21 PgC/yr.

The 750 ppmv neutral orbit simulation (Figure 3.22) displays a total NPP output of 78.43 PgC/yr, an increase of 17.25 PgC/yr globally over the 500 ppmv neutral orbit simulation. Antarctica contributes 2.90 PgC/yr (3.70% of total) to the global total in the 750 ppmv neutral orbit simulation. NPP is highest in the low latitudes with minimal contributions from mid to high latitudes.

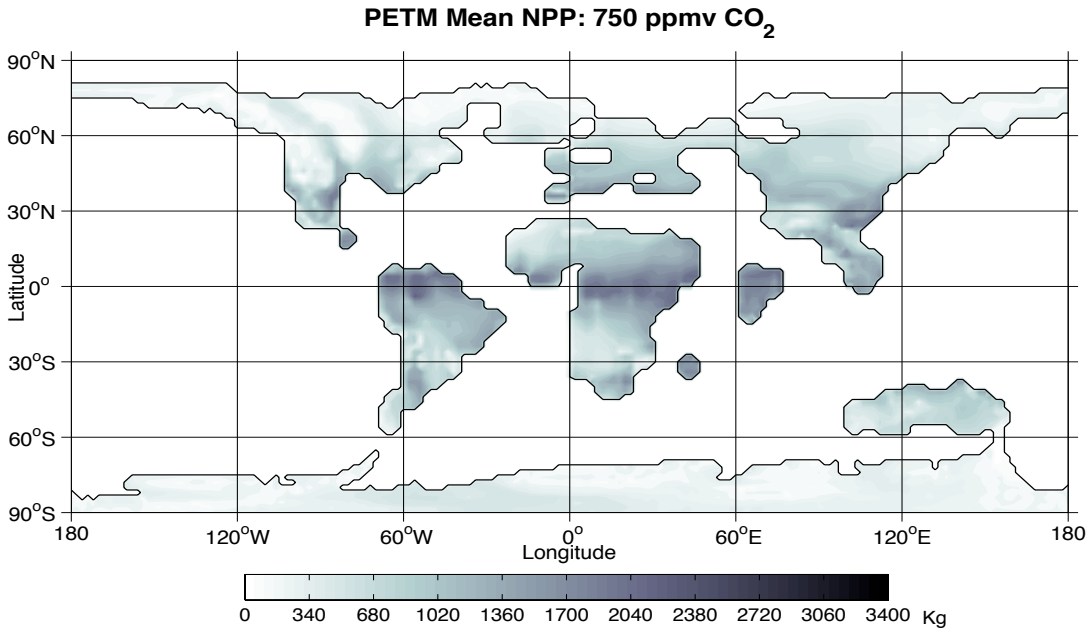

Figure 3.22: Global NPP for the 750 ppmv CO_2 simulation
The 750 ppmv neutral orbit simulation displays a NPP total of 78.43 PgC/yr with Antarctica contributing 2.90 PgC/yr. The low latitudes contain the highest NPP values with little contribution from the mid to high latitudes.

The 750 ppmv cold (Fig 3.24), warm (Fig 3.23), and high obliquity (Fig 3.25) orbit simulations will be discussed together for a better comparison with all three figures following below. The 750 ppmv warm orbit yielded the lowest global NPP total (82.25 PgC/yr) of the three simulations, with Antarctica contributing 3.67 PgC/yr (4.46% of the warm orbit total) to the global total. The cold orbit simulation yielded the highest NPP global total with 82.85 PgC/yr with Antarctica yielding the lowest NPP of 3.01 PgC/yr (3.63 of the cold orbit total). The high obliquity simulation produced an NPP total of 82.72 PgC/yr global and a 3.30 PgC/yr contribution from Antarctica (3.99% of the high obliquity total). The results of the 750 ppmv warm and cold orbits are expected with respect to which simulation yielded the highest/lowest totals based on the orbital configuration. The distribution of global NPP output varies slightly from the cold and

warm run, with high northern latitudes contributing a greater amount in the cold orbit simulation than in the warm orbit simulation. This is also expected given the simulation setup. The NPP output from Antarctica across the three 750 ppmv orbitally varied simulations only changes by 0.5 PgC/yr. The contribution to the global total remains low, yet not absent.

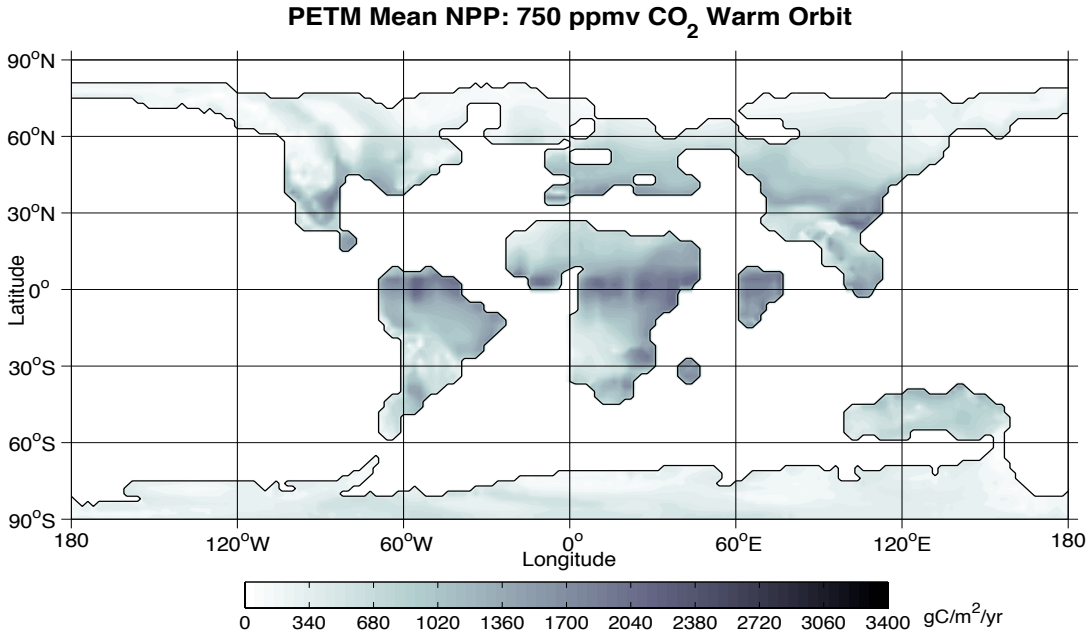

Figure 3.23: Global NPP for the 750 ppmv CO_2 warm orbit simulation
The 750 ppmv warm orbit simulation yield an NPP of 82.25 PgC/yr globally, with Antarctica contributing 3.67 PgC/yr to the global total. This is the lowest contribution from Antarctica of the 750 ppmv orbitally varied simulations. Most NPP is seen in the low latitudes.

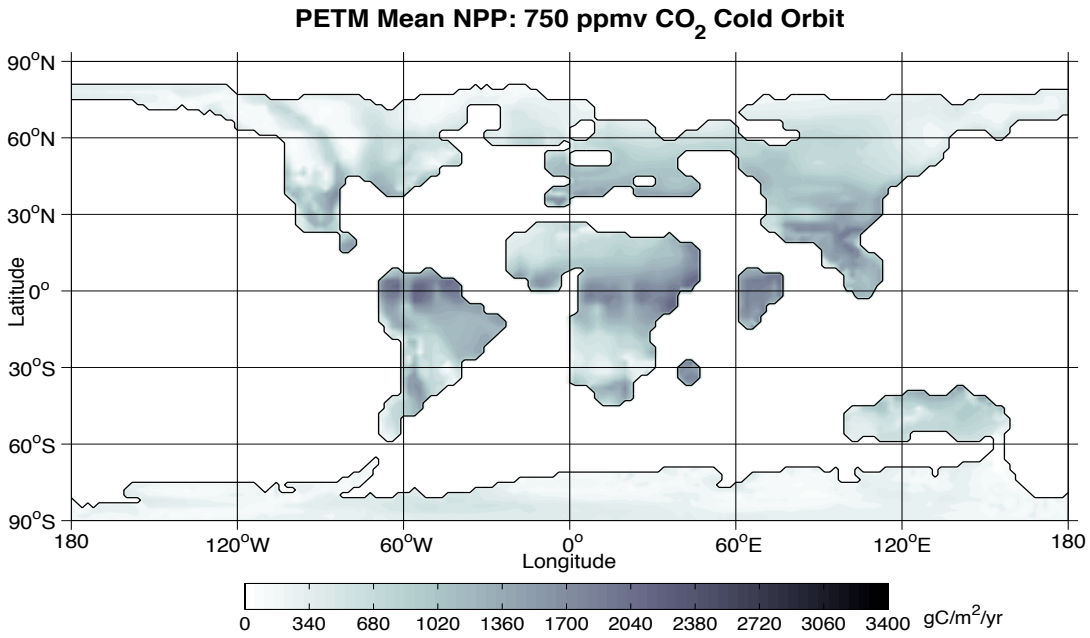

Figure 3.24: Global NPP for the 750 ppmv CO_2 cold orbit simulation
750 ppmv cold orbit simulation yield a NPP of 82.85 PgC/yr global with Antarctica contributing 3.01 PgC/yr to the global total.

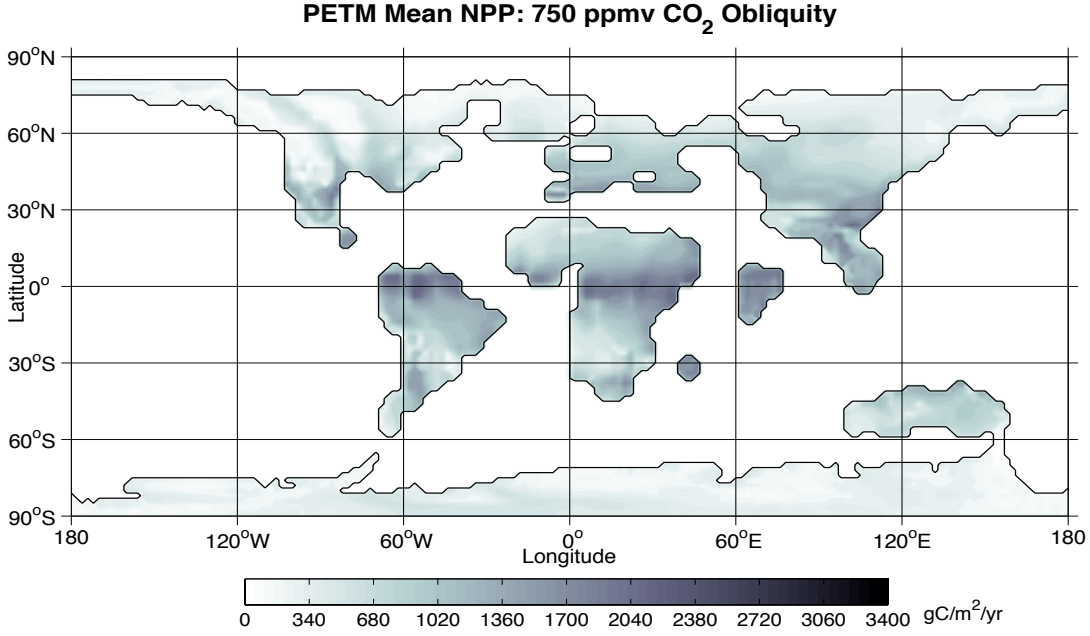

Figure 3.25: Global NPP for the 750 ppmv CO_2 high obliquity simulation
The 750 ppmv high obliquity simulation yield a NPP of 82.72 PgC/yr global with Antarctica contributing 3.30 PgC/yr to the global total.

A significant jump is observed in the NPP global total between the 750 ppmv simulations and the 1,000 ppmv neutral orbit simulation (Fig 3.26). The 1,000 ppmv simulation yields 94.58 PgC/yr with Antarctica contributing 3.56 PgC/yr (3.76% of total) to the global total. The north and south mid latitudes become a key contributor with the areas of modern day south-central North America and Eurasia, as well as northern Australia producing outputs on the order of 1,300 KgC/yr per grid cell, which nearly equals the equatorial outputs which are typically the highest outputs observed. This is in comparison to the polar region, which produce outputs on the order of ~210 KgC/yr per (2°x2°) grid cell.

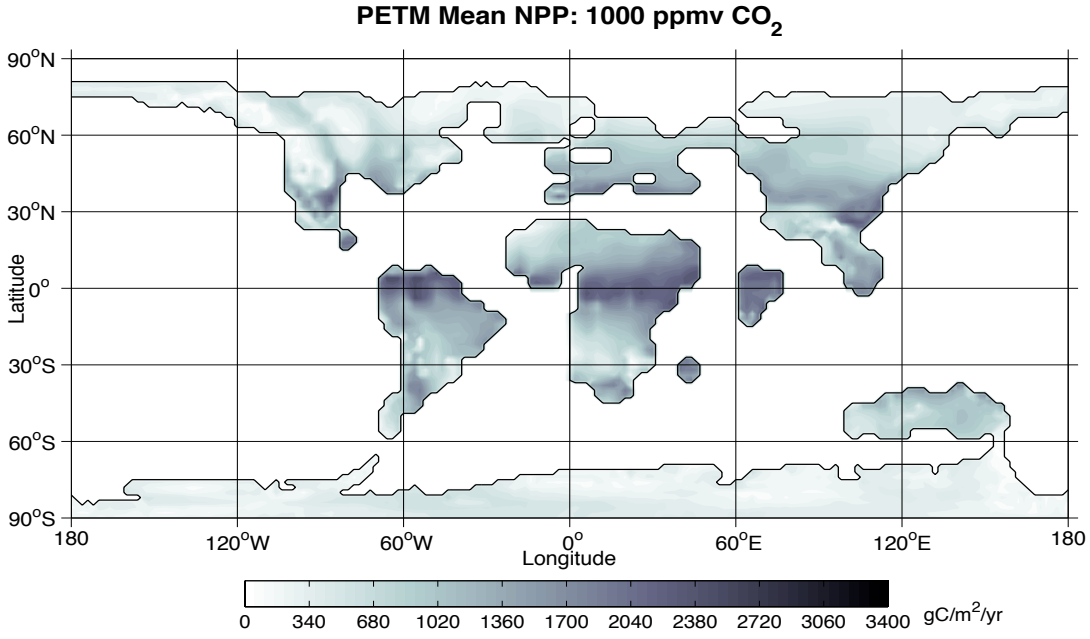

Figure 3.26: Global NPP for the 1000 ppmv CO_2 simulation
The 1000 ppmv simulation displayed the largest CO_2 output increase of the simulations discussed thus far. The simulation yield a NPP global total of 94.58 PgC/yr with Antarctica contributing 3.56 PgC/yr. The north and south mid latitudes became main contributors in this simulation.

The 2,000 ppmv neutral orbit simulation (Fig 3.27) doubles the atmospheric CO_2 from the previous simulation. The NPP increases to 140.99 PgC/yr with Antarctica

contributing 5.97 PgC/yr to the global total (4.23% of total). The elevation (i.e. temperature/precipitation) influence becomes very evident in this simulation with the mountain ranges clearly marked by a notable drop in output per grid cell area. The northern mid-to-high latitudes become major contributors with several low elevation regions north of sixty-degree latitude producing nearly 1,000 KgC/yr per grid cell. The highest output per grid cell on Antarctica is ~751 KgC/yr, with the majority of the land surface area producing totals on the order of ~400 KgC/yr per grid cell area.

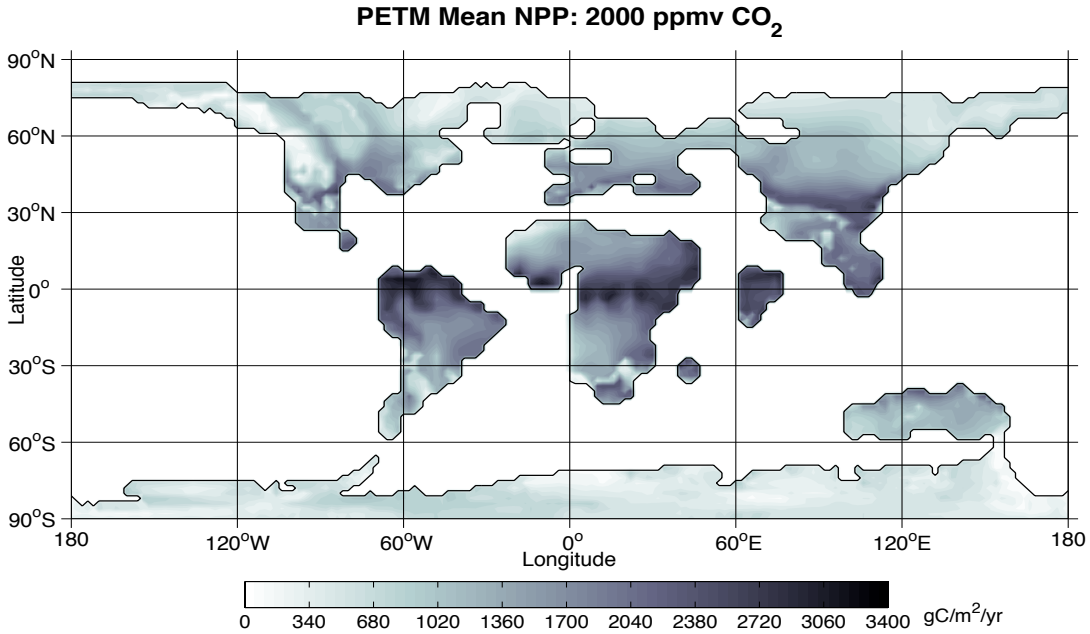

Figure 3.27: Global NPP for the 2000 ppmv CO_2 simulation
The 2000 ppmv neutral orbit simulation yield a NPP global total of 140.99 PgC/yr with Antarctica contributing 5.97 PgC/yr. The northern mid to high latitudes become a major contributor the overall global total, however, Antarctica's contribution remains limited. The influence of elevation is more evident in this run than others with the mountains clearly marked by low output values.

The 4,000 ppmv neutral orbit simulation (Fig 3.28) produced an NPP global total of 202.02 PgC/yr with Antarctica contributing 10.21 PgC/yr. As with the 2,000 ppmv simulation, the northern mid-to-high latitudes contribute a significant amount of carbon

to the global total along with the mid-southern latitudes. However, Antarctica NPP remains limited regardless of the warmer global conditions. As with the 2,000 ppmv simulation, the global mountain ranges are clearly marked on all continents.

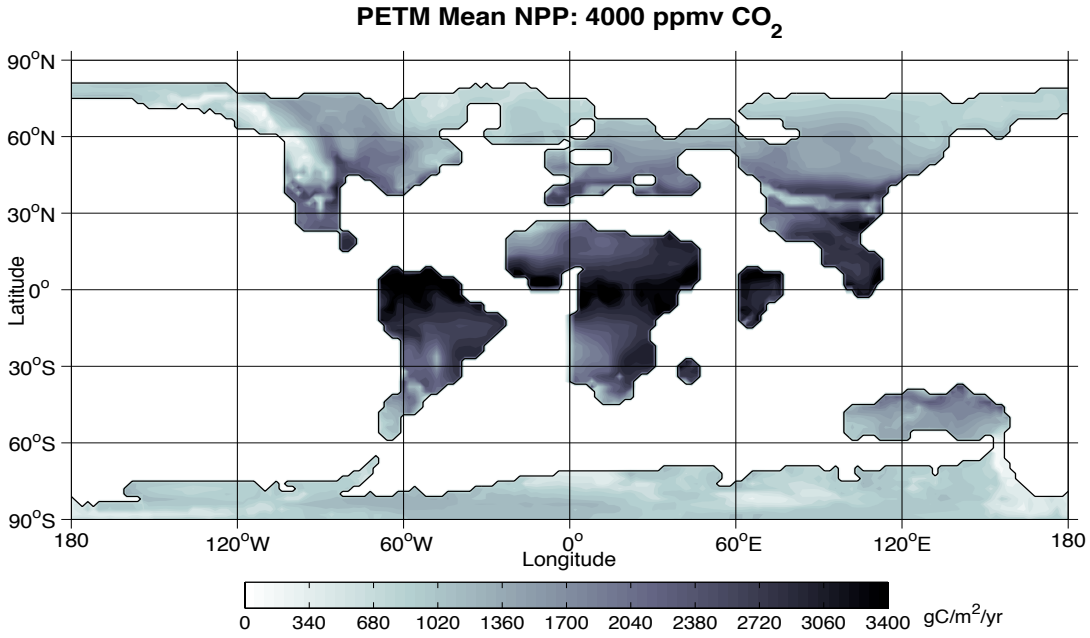

Figure 3.28: Global NPP for the 4000 ppmv CO_2 simulation
The 4,000 ppmv CO_2 neutral orbit simulation yields a NPP global output of 202.02 PgC/yr, with Antarctica contributing 10.21 PgC/yr. The equatorial region remains the highest contributor as is consistent with the other simulations. The northern mid and high latitudes along with the southern mid-latitudes produce significant contributions to the global total.

3.2.4 Soil Respiration

As outlined in the methods section, the Rs model utilized here is based on an algorithm that draws on the GENESIS outputs of precipitation and two-meter surface air temperature. As a result, the Rs outputs, as noted with the NPP outputs, are directly linked to the same parameters that control GENESIS temperature and precipitation. As seen in the Biome4 control simulation (Figure 3.29), elevation is again a key factor in the Rs output as well. The BIOME4 control simulation produces a global total of 74.00 PgC/yr, compared with the observed of 74 PgC/yr (Bahn *et al.*, 2009). For methodology of Rs global and continental estimates please refer to section 2.8.1 and 2.8.2.

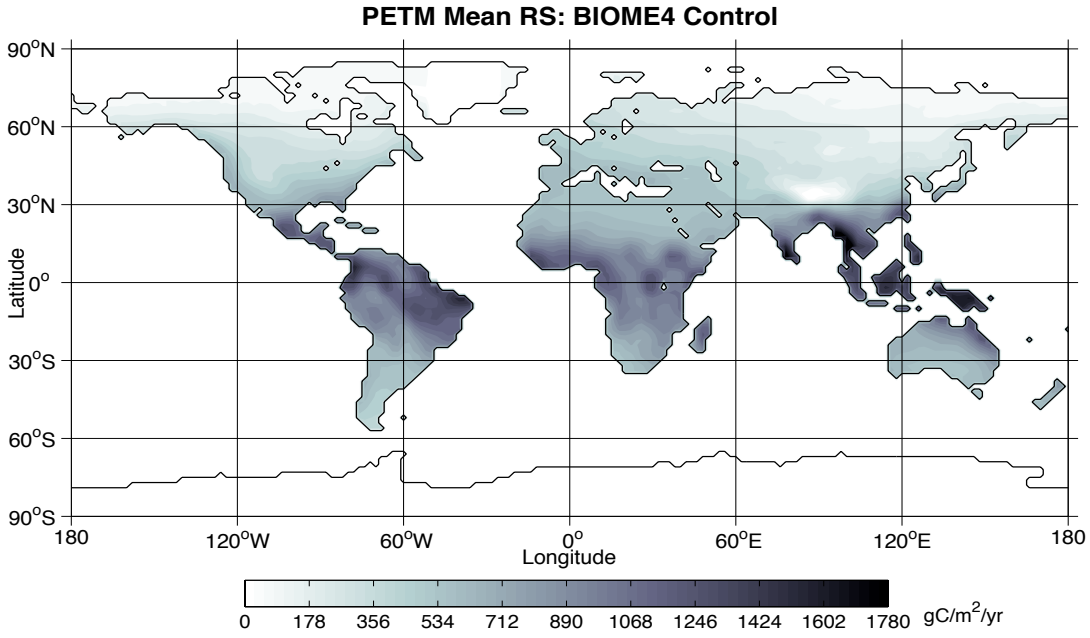

Figure 3.29: Global Rs output for the control simulation
The BIOME4 control simulation displays the global distribution of Rs. The global total is 74.00 PgC/yr. Note the output elevation dependence, which is directly tied to temperature and precipitation.

The 500 ppmv neutral orbit simulation (Fig 3.30) is very similar in appearance to the Rs control simulation with respect to the layout of high and low output

concentrations. The major difference is the incorporation of Antarctica in the global total. The highest outputs are found along the equatorial regions while the mid to high latitudes contribute very little to the global. The 500 ppmv simulation yields 56.85 PgC/yr with Antarctica providing 2.03 PgC/yr (3.57% of total) to the global total. The 500 ppmv simulation is reduced from the control simulation due to the overall reduction in available terrestrial area from increased sea level.

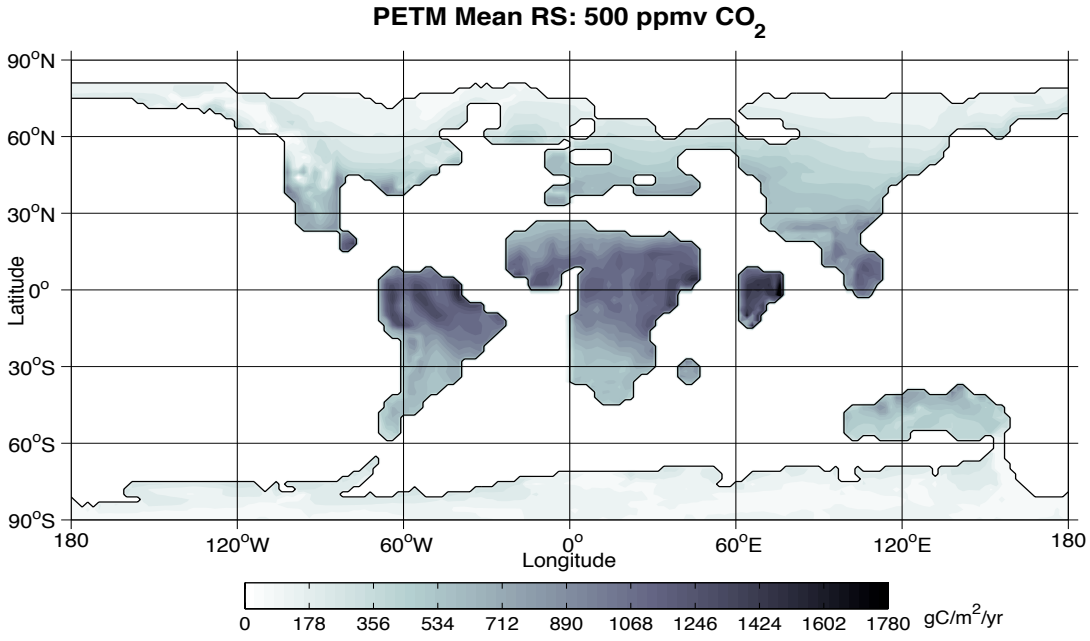

Figure 3.30: Global Rs output for the 500 ppmv CO_2 simulation
The 500 ppmv neutral orbit simulation yield 56.85 PgC/yr with Antarctica contributing 2.03 PgC/yr to the global total. Note the high output of the equatorial region with limited output from the mid to high-latitudes.

The 750 ppmv neutral orbit simulation (Fig 3.31) is nearly identical to the 500 ppmv run based on appearance, with no noticeable increase in output concentration for a given area. The 750 ppmv neutral orbit simulation yields 63.74 PgC/yr, with Antarctica contributing 2.58 PgC/yr (4.04% of total) to the global total. This is a global terrestrial increase of 6.89 PgC/yr over the previous simulation. The northern mid latitudes begin to

produce higher output levels on the order of ~550 KgC/yr per grid cell. Antarctica's contribution remains limited with outputs of ~120 KgC/yr per grid cell.

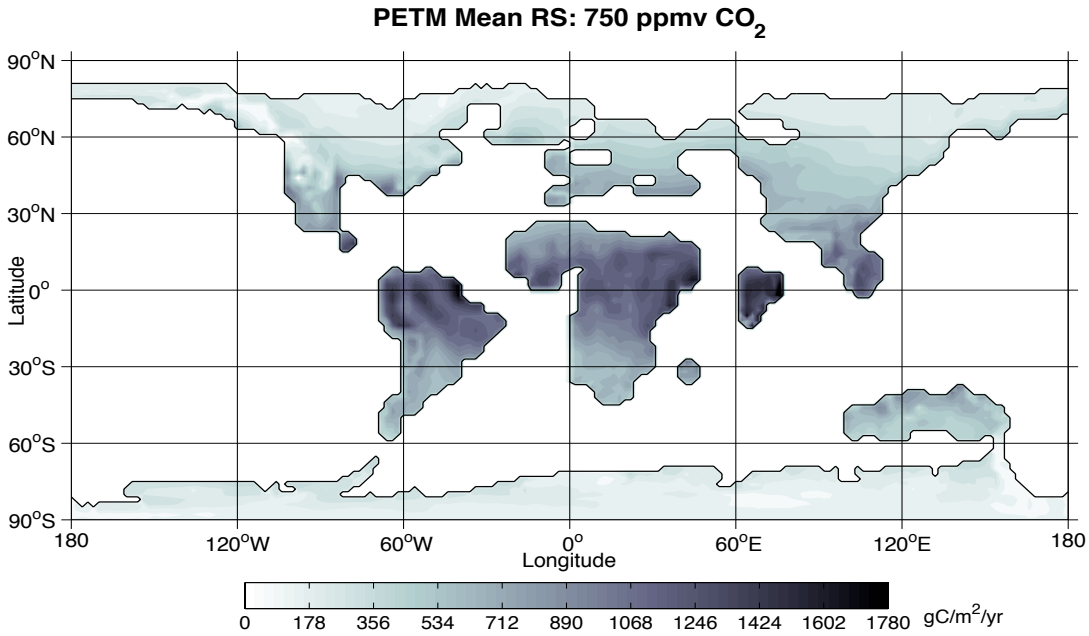

Figure 3.31: Global Rs output for the 750 ppmv CO_2 neutral orbit simulation The 750 ppmv neutral orbit simulation yields an NPP output of 63.74 PgC/yr, with Antarctica contributing 2.58 PgC/yr to the global total. Note the limited output of Antarctica thus far and the increase northern mid-latitude carbon flux.

The 750 ppmv cold, warm, and high obliquity orbital configuration simulations are discussed together for comparative purposes. The 750 ppmv cold orbit simulation (Fig 3.32) displays a notable change in the northern mid to high latitudes compared to the 750 neutral orbit simulation. The 750 ppmv cold orbit simulation yield 65.96 PgC/yr with Antarctica contributing 2.72 PgC/yr (4.12% of the cold orbit total). This simulation yields the largest global total of the three orbitally varied 750 ppmv simulations. The 750 ppmv warm orbit simulation (Fig 3.33) displayed an increase in Southern Hemisphere Rs output. The equatorial region remains the main contributor as with the other various simulations previously discussed in this section. The 750 ppmv warm orbit simulation

yields a 65.69 PgC/yr with Antartica contributing 2.83 PgC/yr (4.31% of the warm orbit total). Antarctica produced the highest output in all of the orbitally varied simulations in the warm orbit simulation. The 750 ppmv high obliquity simulation (Fig 3.34) does not highlight any particular area globally, instead the overall total is higher due to a slight global increase in Rs output versus a northern or southern hemisphere bias. This simulation produced an Rs output of 65.10 PgC/yr with Antarctica contributing 2.73 PgC/yr (4.19% of the total). The 750 ppmv high obliquity simulation is slightly increased over the cold orbit simulation (by 0.01 PgC/yr) for Antarctic output and overall the lowest NPP result of the three simulations.

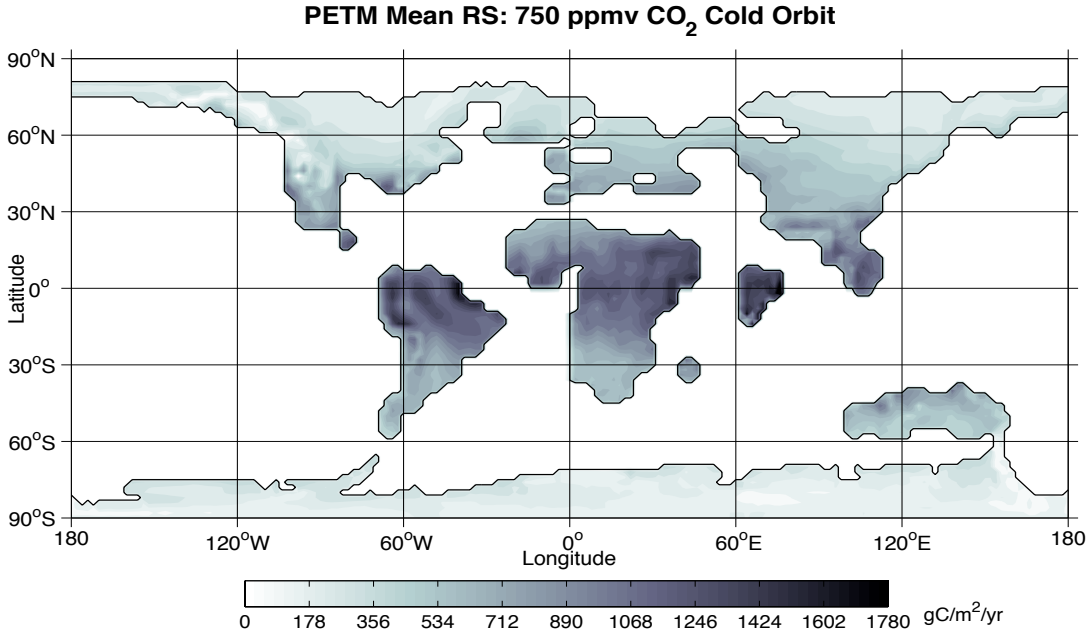

Figure 3.32: Global Rs output for the 750 ppmv CO_2 cold orbit simulation The 750 ppmv CO_2 cold orbit simulation yield a global total of 65.96 PgC/yr with Antarctica contributing 2.72 PgC/yr. Note the Northern Hemisphere mid-latitude expansion the higher Rs output as seen near the equator.

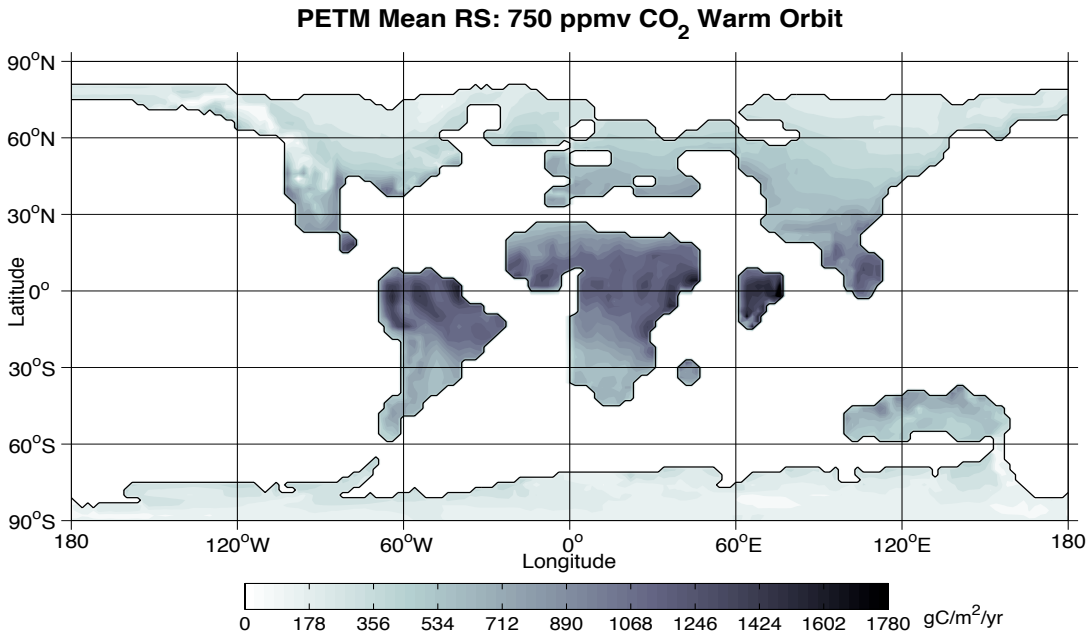

Figure 3.33: Global Rs output for the 750 ppmv CO_2 warm orbit simulation The 750 ppmv CO_2 warm orbit simulation yields a global total of 65.69 PgC/yr, with Antarctica contributing 2.83 PgC/yr. Note the Southern Hemisphere mid latitude expansion the higher Rs output as seen near the equator.

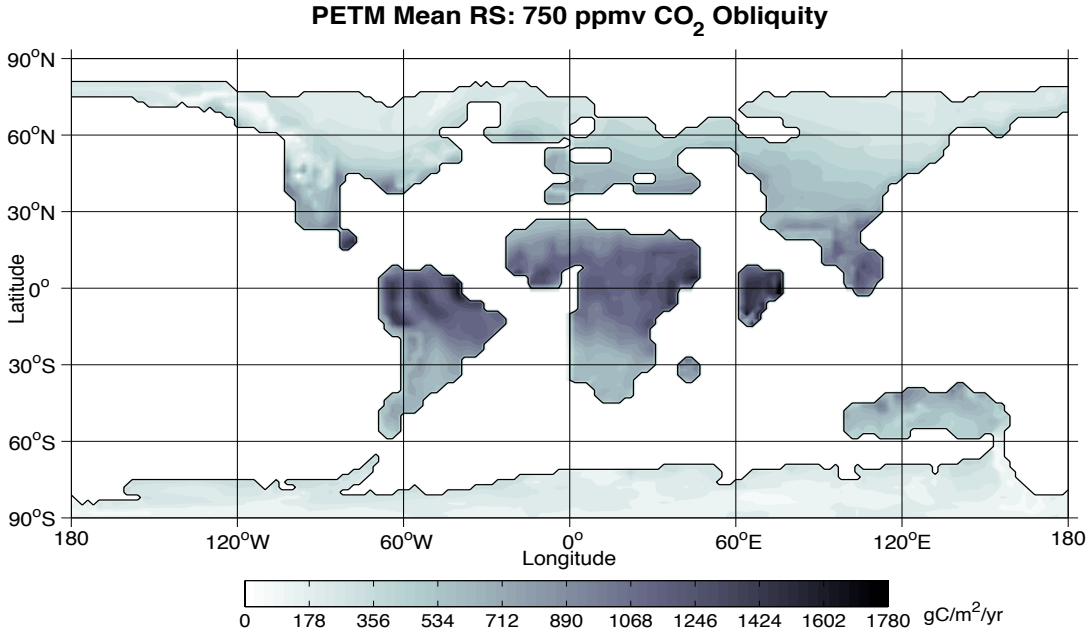

Figure 3.34: Global Rs output for the 750 ppmv CO_2 high obliquity simulation The 750 ppmv CO_2 high obliquity simulation yield a global total of 65.10 PgC/yr with Antarctica contributing 2.73 PgC/yr. Note the lack of a hemispheric bias with a slight increase in Rs output globally.

The 1000 ppmv neutral orbit simulation (Fig 3.35) displays an overall global increase in Rs output with the Northern Hemisphere showing a larger increase over the Southern Hemisphere. The southern mid-latitudes also increase in Rs, however, due to the smaller area per degree on latitude, the Northern Hemisphere increase has a larger total output and therefore affect of the global total. Antarctica's output increased by 0.33 PgC/yr over the average of the 750 ppmv simulations (average of 2.72 PgC/yr), with a total of 3.05 PgC/yr for the 1000 ppmv simulation. The Rs output produced a global total of 71.4 PgC/yr.

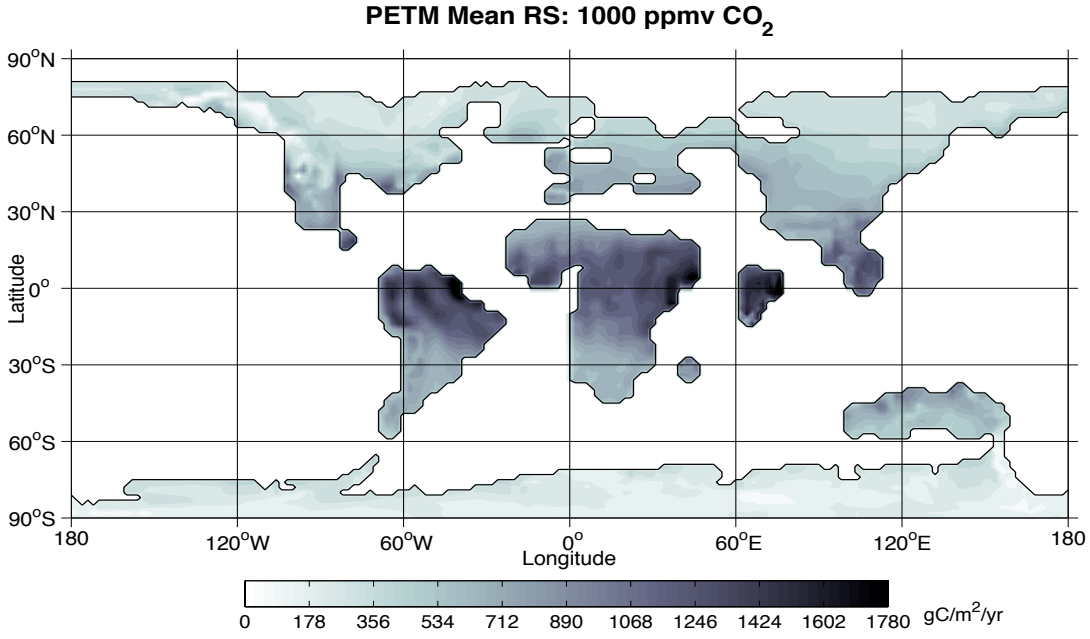

Figure 3.35: Global Rs output for the 1000 ppmv CO_2 simulation
The 1000 ppmv CO_2-neutral orbit simulation yield a global total of 71.4 PgC/yr with Antarctica contributing 3.05 PgC/yr. Note the substantial global increase of the Rs output in comparison to the previous simulations. The elevation dependency becomes more apparent at the higher atmospheric CO_2 concentrations.

The 2000 ppmv neutral orbit simulation (Fig 3.36) displays a notable increase in global Rs output, specifically in the equatorial region. Along the equator outputs are observed on the order of ~1,500 KgC/yr per grid cell area. As previously mentioned, the dependence on topography becomes more apparent with the higher Rs outputs. The 2000 ppmv simulation produced a global Rs output of 86.10 PgC/yr with Antarctica contributing 4.23 PgC/yr.

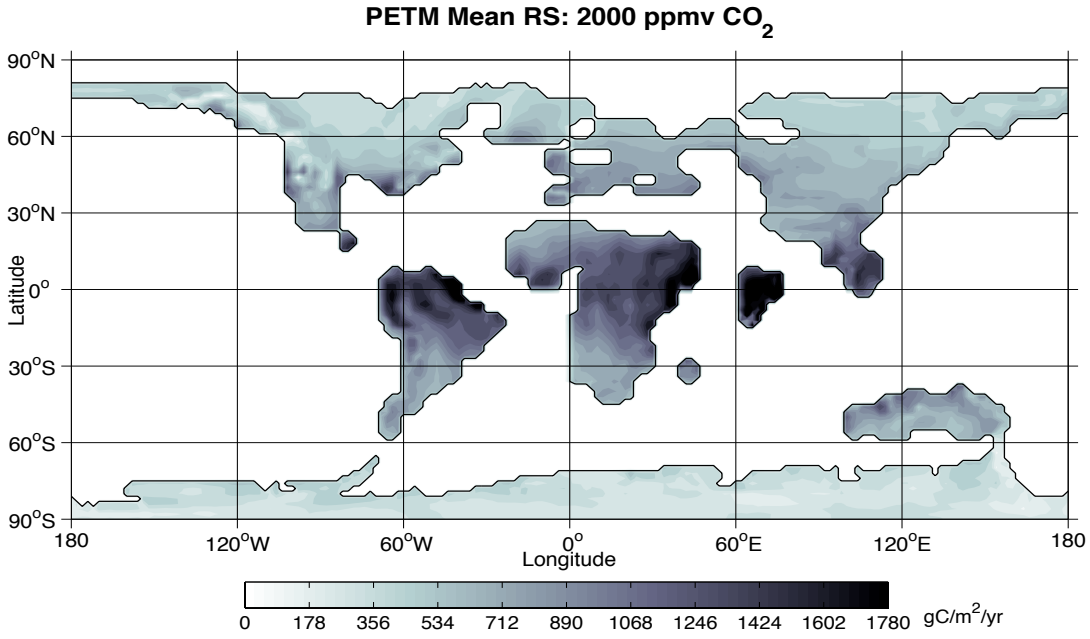

Figure 3.36: Global Rs output for the 2000 ppmv CO_2 simulation
The 2000 ppmv CO_2 neutral orbit simulation yields a global total of 86.10 PgC/yr, with Antarctica contributing 4.23 PgC/yr. Note the substantial global increase of the Rs output in comparison to the previous simulations, specifically in the equatorial region.

The 4000 ppmv neutral orbit simulation (Fig 3.37) displays a global increase of 15.26 PgC/yr over the 2000 ppmv simulation. The 4000 ppmv simulation yields 101.36 PgC/yr with Antarctica contributing 5.80 PgC/yr. The equatorial region displays Rs output values on the order of ~1,600 KgC/yr per grid cell. The output observed from Antarctica is on the order of ~400 KgC/yr per gird cell area.

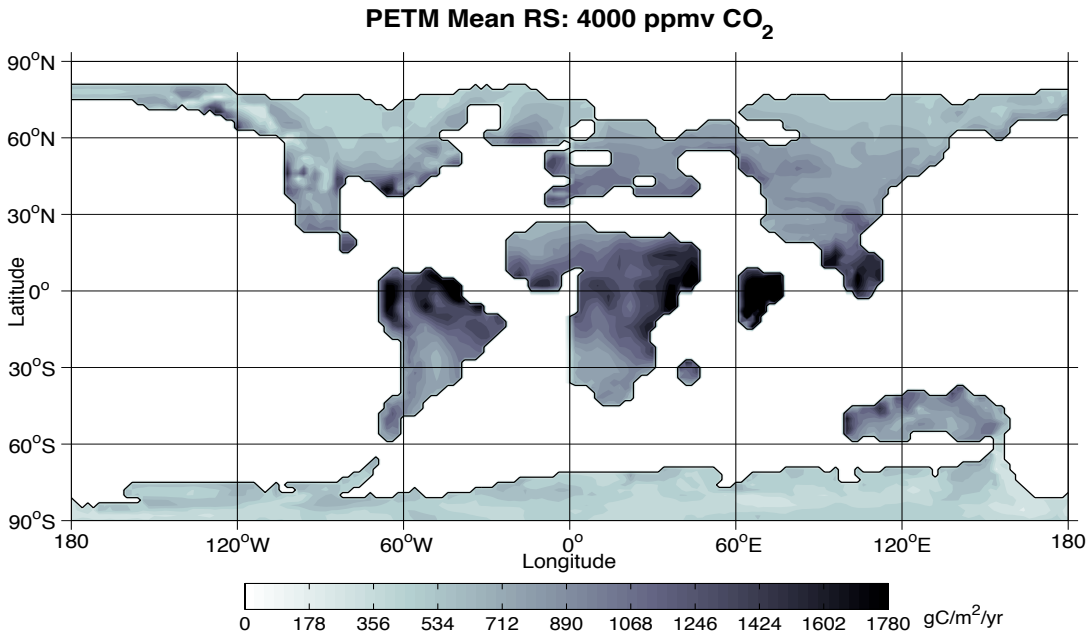

Figure 3.37: Global Rs output for the 4000 ppmv CO_2 simulation
The 4000 ppmv CO_2 neutral orbit simulation yields a global total of 101.36 PgC/yr, with Antarctica contributing 5.80 PgC/yr. As Noted with the 2000 ppmv simulation, there is a substantial global increase of the Rs output in comparison to the previous simulations, specifically in the equatorial region.

3.2.5 NPP vs. Rs

In order to compare NPP and Rs globally, the two outputs were plotted against one another with Rs/NPP on the Y-axis and degrees latitude on the X-axis as can be seen in the control simulation (Fig 3.38). The control displays an equatorial region with NPP producing a slightly higher output over Rs. The northern mid through high latitudes, from 35° northward, show that the output of Rs and NPP are roughly equal with Rs producing a slightly higher output. For the control simulation, Rs produces an overall higher output than NPP, with 74.00 PgC/yr and 62.4 PgC/yr, respectively. As expected, the Rs and NPP output for Antarctica are both zero. At approximately +/-25° there is an NPP minima which may related to precipitation. This can be seen in Figure 3.39 with average annual precipitation (mm/yr) plotted in the same method as NPP and Rs. Via Figure 3.39 it is

easy to observe that close relationship between NPP and precipitation. Further more, this suggests that as global atmospheric carbon increases so does global precipitation.

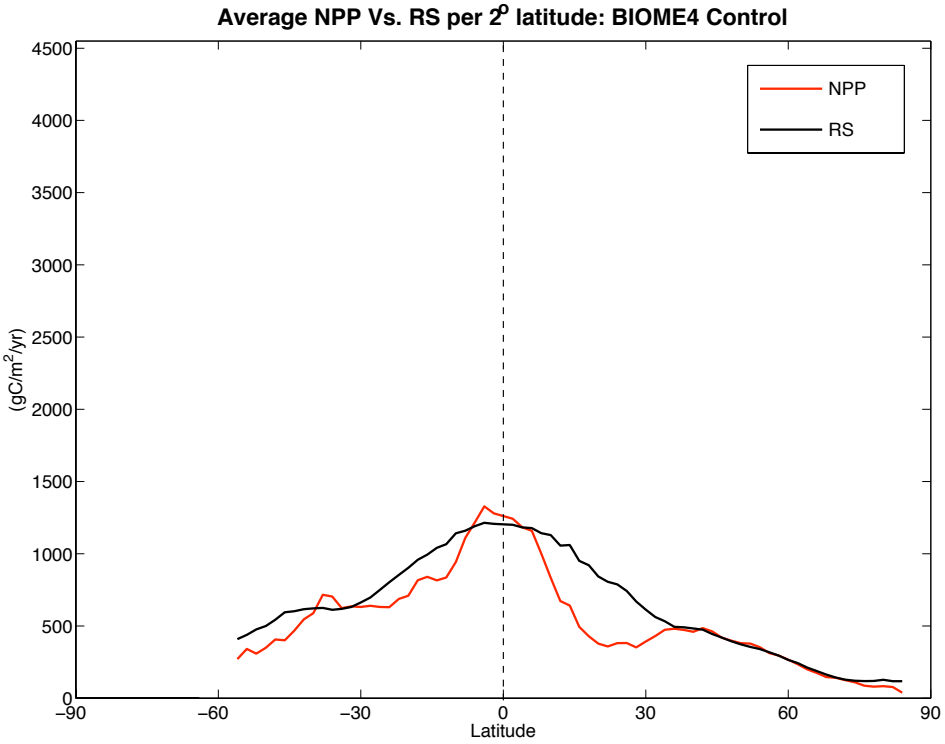

Figure 3.38: Zonally averaged NPP vs. Rs: control simulation
The control simulation illustrates the equatorial high output for both variables. The output of Antarctica is absent with the northern mid to high latitude NPP and Rs outputs nearly equal.

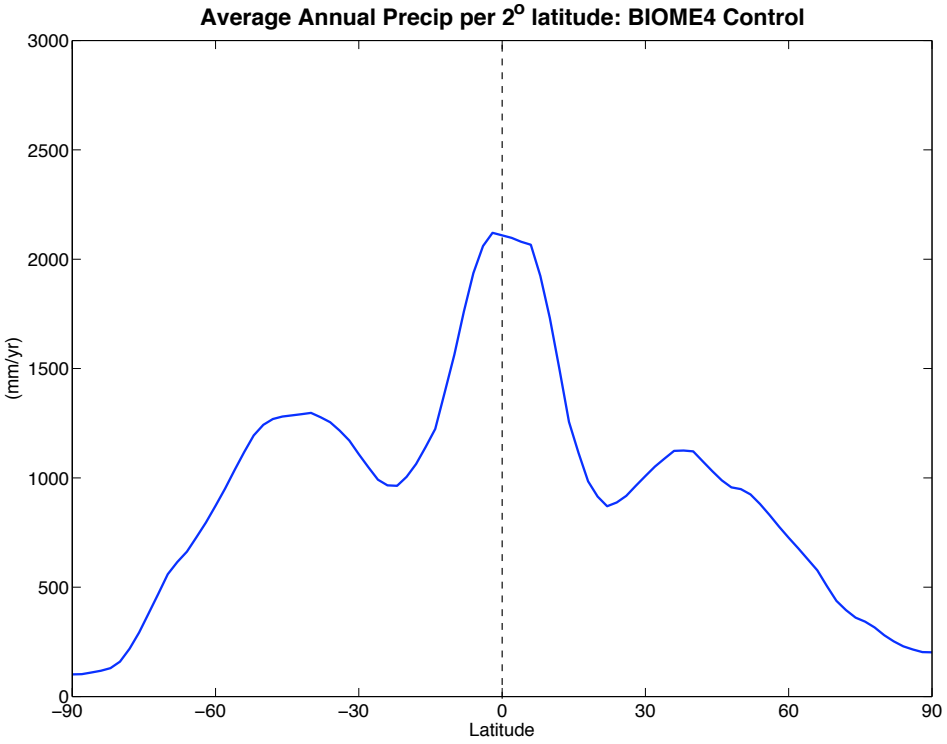

Figure 3.39: Zonally averaged annual precipitation: control simulation Plotted in the same fashion NPP and Rs in this section. The above displays average annual precipitation in mm/yr. NPP closely resembles precipitation, which indicates a strong correlation between the two parameters.

The 500 ppmv neutral orbit simulation (Fig 3.40) displays increased NPP along the equatorial region, as well as at ~35° north and south of the equator. Antarctica is now an active component of the terrestrial biosphere and is incorporated into totals, displaying interesting results. Along the northern most boundary of Antarctica Rs output is higher than NPP. Further south near -80° Rs drops and NPP increases. At -90°, NPP is the dominant output. From +/- 5° to ~ +/- 30° Rs in latitudinal totals are larger than NPP. NPP is slightly increased over Rs indicating a net sink of global atmospheric carbon is taking place.

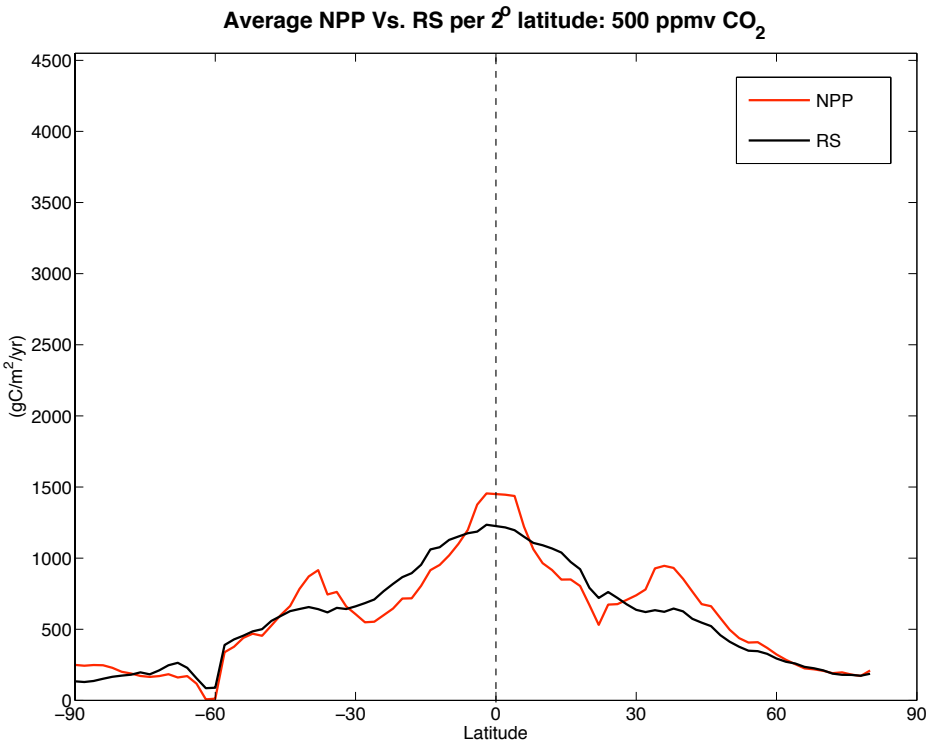

Figure 3.40: Zonally averaged NPP vs. Rs: 500 ppmv CO_2 simulation
The 500 ppmv neutral orbit simulation shows NPP beginning to increase with Rs reduced. Rs and NPP production has now begun on Antarctica. Note the increased NPP output at +/- 30° latitude as well as along the equator. These results indicate a slight net sink in atmospheric carbon.

The 750 ppmv neutral orbit simulation (Fig 3.41) has very similar characteristics to the 500 ppmv simulation. The 750 ppmv simulation outputs are slightly increased in both hemispheres, with the peak Rs output seen at the equator and the peak NPP outputs seen at +/- 35° as well as at the equator. Antarctic NPP and Rs output compensate similarly to the 500 ppmv simulation. As with the 500 ppmv simulation, Rs is equal to or slightly greater than NPP from +/- 5° to +/- 30°, this same observation is true for all of the 750 ppmv simulations. This may be attributed to the savanna biome that exists in these regions.

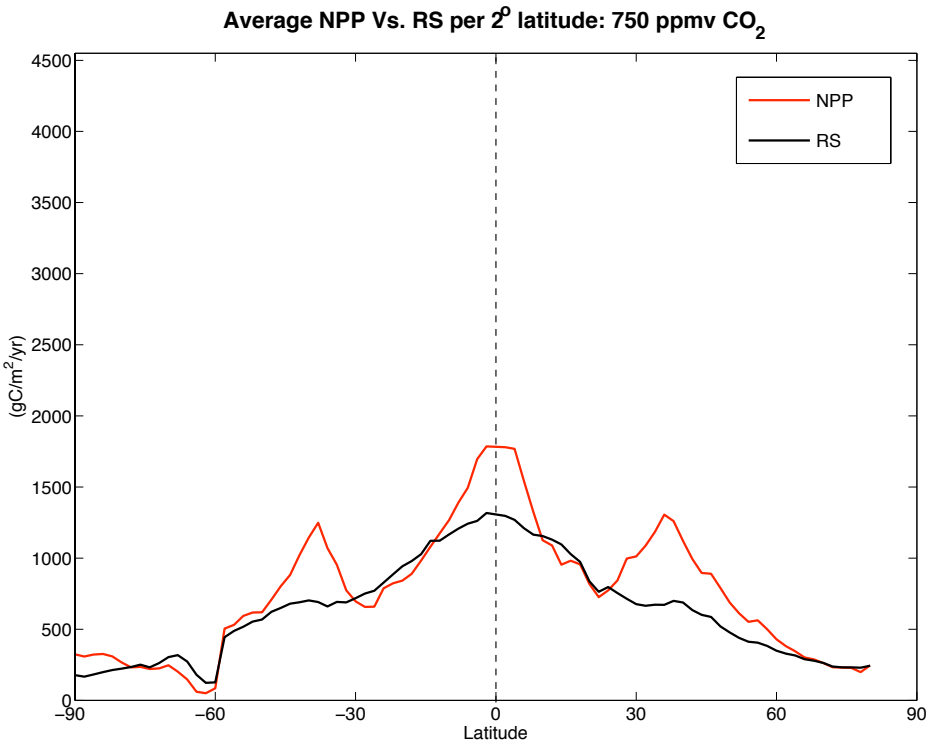

Figure 3.41: Zonally averaged NPP vs. Rs: 750 ppmv CO_2 neutral orbit simulation

The 750 ppmv neutral orbit simulation displays three NPP output peaks at +/- 35° as well as at the equator. Rs output maximum is seen only at the equator. Note the Rs/NPP Antarctic output reversal and the northern mid-to-high latitude region where NPP and Rs are roughly equal.

The 750 ppmv cold orbit simulation (Fig 3.42) displays similar results to the 750 neutral orbit simulation. The Northern Hemisphere displays increases in NPP as well as Rs. The Southern Hemisphere appears unchanged from the 750 ppmv neutral orbit simulation. NPP continues with the output peaks at +/- 35° and the equator, while Rs has one peak at the equator. The NPP peak is offset to the south in this simulation.

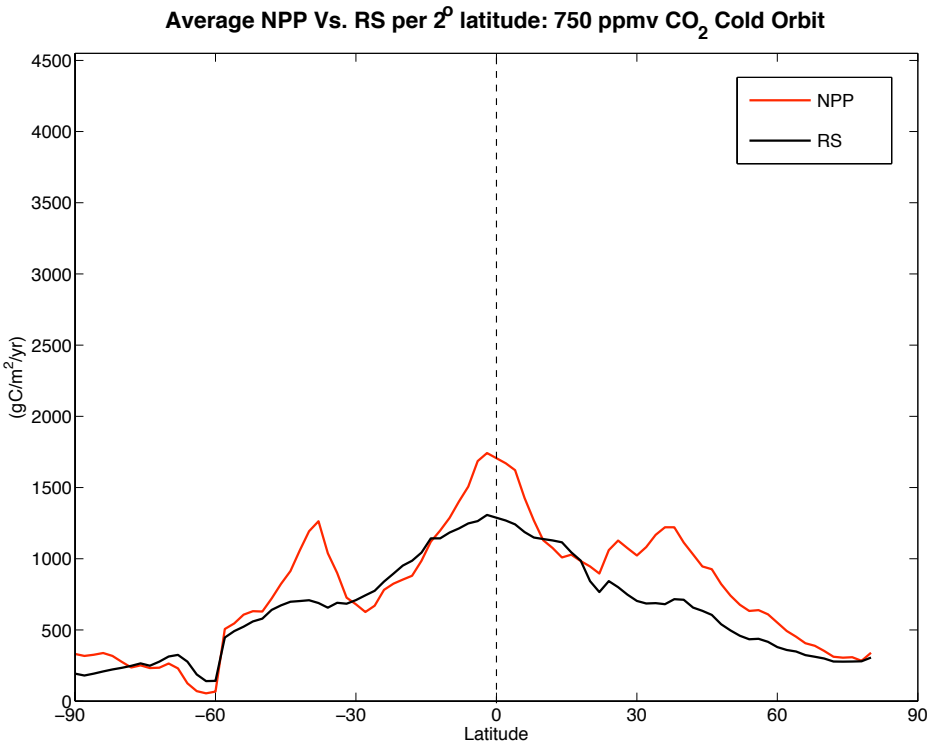

Figure 3.42: Zonally averaged NPP vs. Rs: 750 ppmv CO_2 cold orbit simulation The 750 ppmv cold orbit simulation displays increases in the Northern Hemisphere from ~15° to 80° while the Southern Hemisphere remains unchanged. NPP continues with the three maxima output (+/- 35°, equator) while Rs has one maximum (equator).

The 750 ppmv warm orbit simulation (Fig 3.43) displays an increase in the southern NPP. This can be seen from -75° to -90° as well as at -55°. Rs output is slightly increased. The Northern Hemisphere resembles the neutral orbit simulation with regard to NPP. As in previously discussed simulations, NPP continues with the three latitudinal maxima (+/- 35°, equator), while Rs has one maximum (equator).

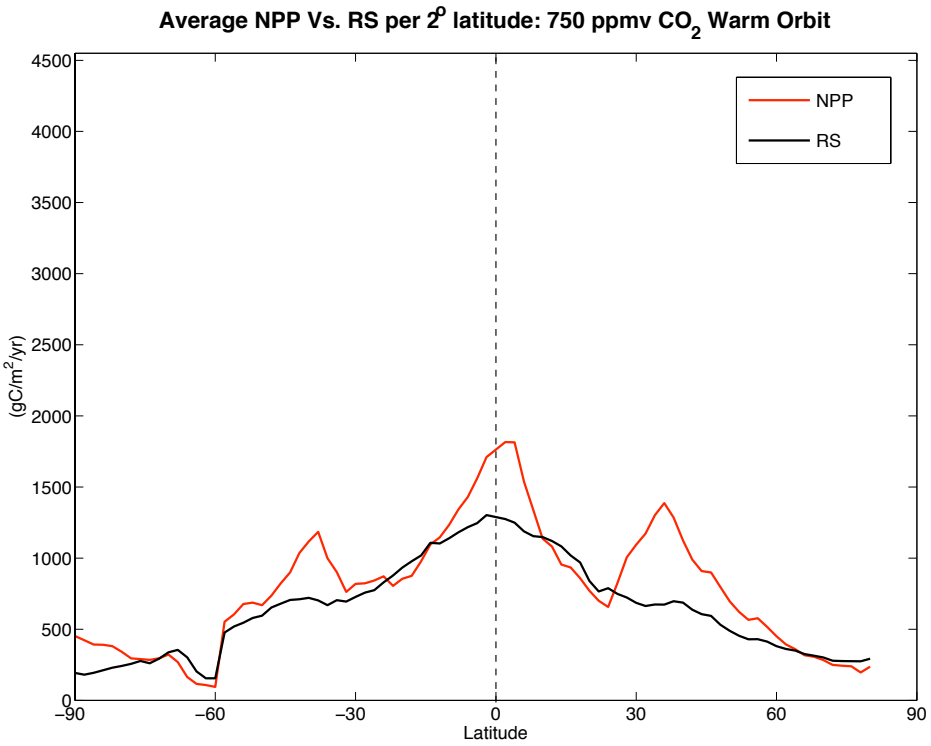

Figure 3.43: Zonally averaged NPP vs. Rs: 750 ppmv CO_2 warm orbit simulation The 750 ppmv warm orbit simulation displays increase Southern Hemisphere NPP and Rs output. The Rs increase is limited with NPP showing larger increases. In the Northern Hemisphere NPP peaks at ~35° and Rs out is greater than NPP (net source) from ~10° to ~25°.

The 750 ppmv high-obliquity simulation (Fig 3.44) displays results nearly identical to the 750 neutral orbit simulation, however global totals for both Rs and NPP are slightly increased over the neutral orbit condition. As seen previously, the dominance of Rs and NPP trade off at approximately -75°, however, NPP output from -75° to -90° increase over the neutral orbit simulation. NPP contains three maxima (+/- 35°, equator) while Rs has one maximum (equator).

The 750 ppmv simulations displays slight pole to pole varibility. The cold orbit simulation exhibits the highest overall Rs and NPP of the three simulations. The overall result indicates that there is a net sink occurring, which is most likely a global response to

a large carbon influx to the atmosphere. While at 750 ppmv CO_2 flux, orbital variation does not appear to result in a tipping point with a run away sink or influx of atmospheric carbon.

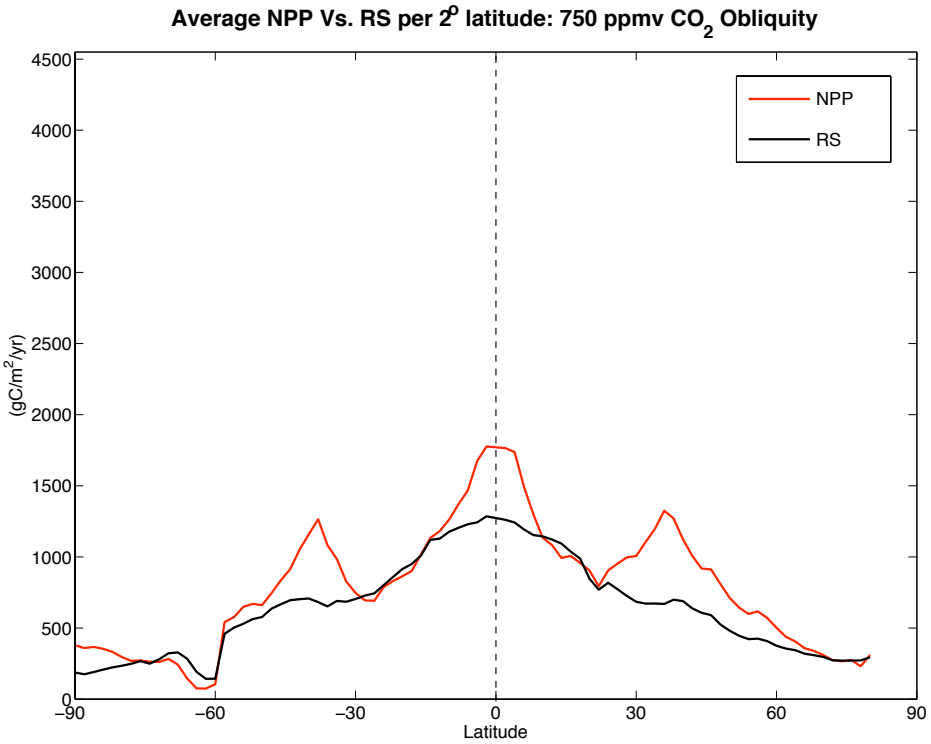

Figure 3.44: Zonally averaged NPP vs. Rs: 750 ppmv CO_2 high obliquity simulation
The 750 ppmv high obliquity simulation displays increased Antarctic NPP output over the neutral orbit condition. NPP continues with the three maxima output (+/- 35°, equator) while Rs has one maximum (equator).

The 1,000 ppmv neutral orbit simulation (Fig 3.45) displays highly increased Rs and NPP outputs, with NPP producing a larger overall increase when compared to Rs. As with the previous simulations NPP contains three maxima with Rs peaking at the equator. Antarctic NPP and Rs output is also slightly increased, with NPP again displaying a larger overall jump in output over the observed Rs increase. In previously described simulations at lower CO_2 levels, Rs output was greater than NPP in the low latitudes with

NPP spikes at the equator. However, in this simulation, NPP and Rs are roughly equal in the low latitudes. Again, this is an example of a global response of an enormous atmospheric carbon sink.

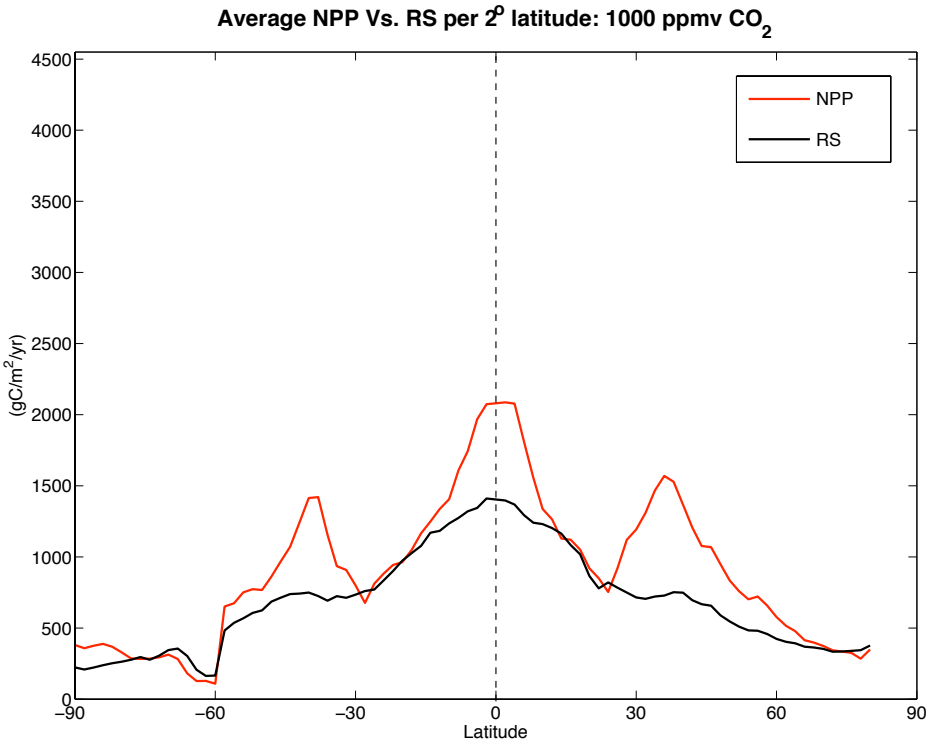

Figure 3.45: Zonally averaged NPP vs. Rs: 1000 ppmv CO_2 simulation
The 1000 ppmv neutral orbit simulation displays greatly increased NPP and Rs output over the previously discussed simulations in this section. As with previous simulations, NPP displays 3 global maxima while Rs peaks at the equator. Note that NPP and Rs are nearly equal in the mid latitudes, whereas previously Rs was greater than NPP.

The 2000 ppmv neutral orbit simulation (Fig 3.46) displays dramatic increases over the 1000 ppmv simulation. NPP has dramatically increased and is now greater than Rs at all latitudes except for -60° to -70°. As previously stated, the biomass growth and global storage of carbon has greatly increased in the 1000 and 2000 ppmv simulations. The mid latitudes (~+/- 30°) display NPP and Rs minima which, as stated, is related to low annual mean precipitation in that band of latitude.

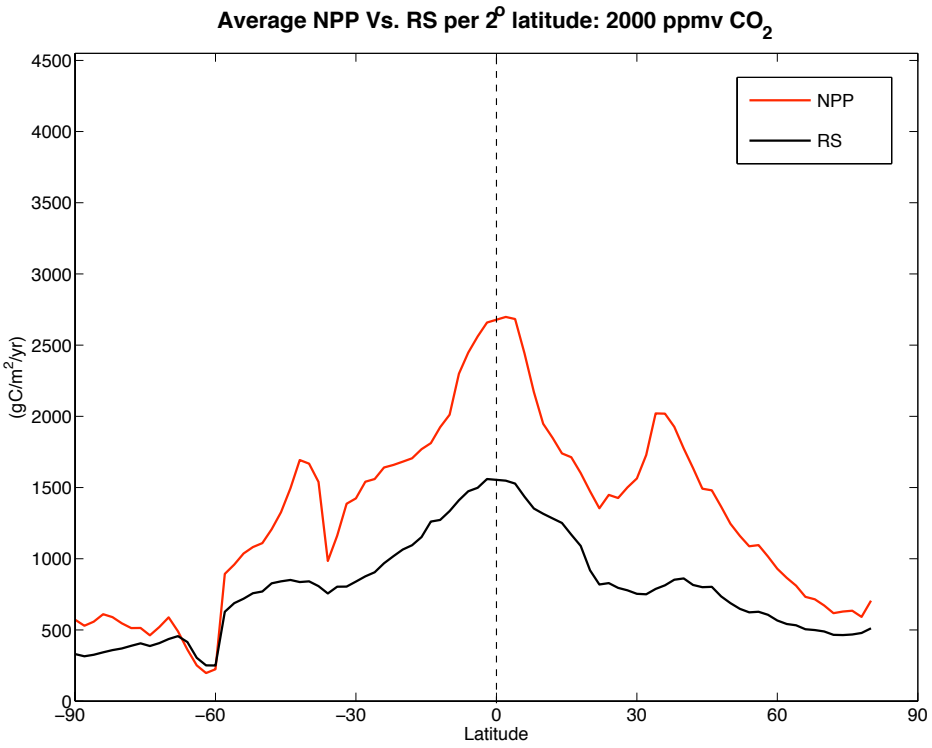

Figure 3.46: Zonally averaged NPP vs. Rs: 2000 ppmv CO_2 simulation
The 2000 ppmv neutral orbit simulation displays a increased global NPP over previous simulations discussed in this section. Rs output is greatly increased as well, however, mean NPP per band of latitude is larger than Rs (except for ~-60°). This indicates that the amount of carbon being sequestered is far great than the amount being released.

The 4000 ppmv neutral orbit simulation (Fig 3.47) displays similar results to the 2000 ppmv simulation. The 4000 ppmv condition shows a marked increase in NPP with Rs displaying less pronounced increases globally. As with the 2000 ppmv simulation, Rs is greater than NPP from -60° to -65°. 4000 ppmv is assumed to be the highest possible peak in PETM atmospheric CO_2. At this point NPP is far greater than Rs, which could be considered to be a global response to sequester atmospheric carbon. The increased NPP also directly reflects a marked increase in precipitation as shown in Figure 3.48. The drastic outpacing of NPP over Rs indicates that not only is there a net sink globally, but

also the terrestrial carbon stock is recharging itself. This recharge affect would actively build up a new carbon pool available for release to drive the subsequent hyperthermals.

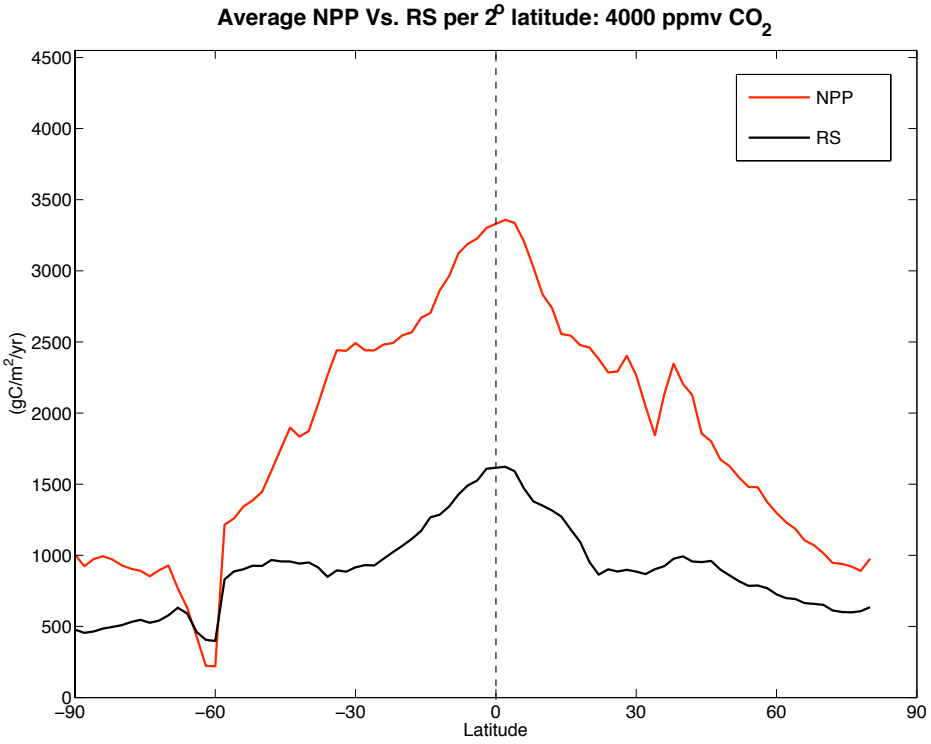

Figure 3.47: Zonally averaged NPP vs. Rs: 4000 ppmv CO_2 simulation
The 4000 ppmv neutral orbit simulation displays a marked increase in NPP while Rs remains nearly unchanged when compared to the 2000 ppmv simulation. The amount of atmospheric carbon sequestered is far greater than the amount released which would indicate a global response towards balancing the global terrestrial/atmospheric carbon stock.

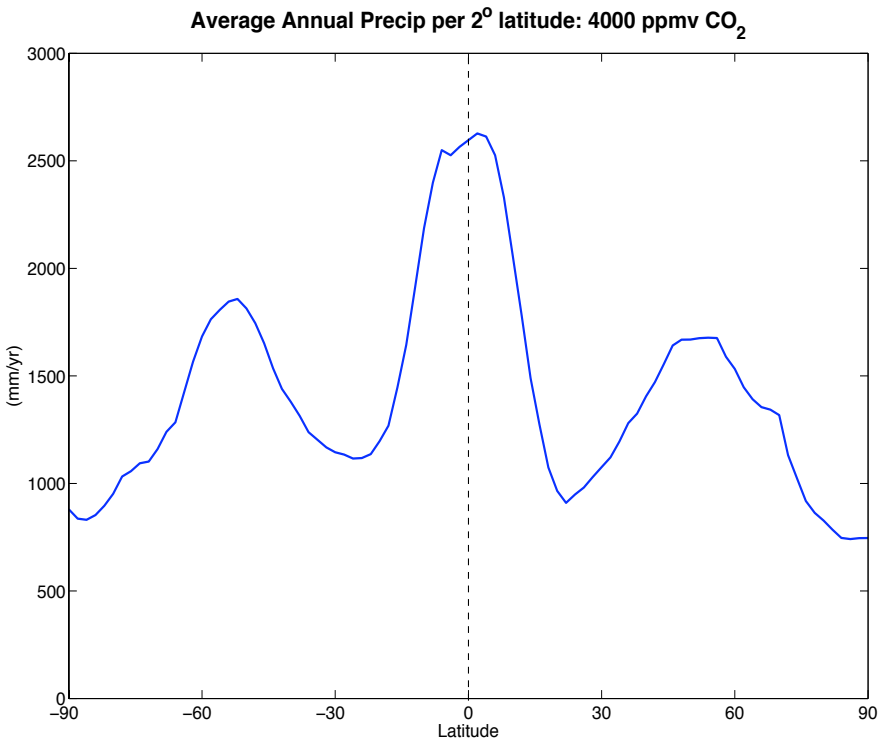

Figure 3.48: Average annual precipitation per 2° latitude: 4000 ppmv CO_2 simulation

The 4000 ppmv global mean precipitation shows significant increases over the control simulation. This mimics the NPP response to global atmospheric carbon increase.

CHAPTER 4

DISCUSSION

The PETM marks a pivotal time in Earth's history and provides a crucial piece of the climatic puzzle that may help to unlock information regarding Earth's future. This research intended to shed light on the dynamics of the terrestrial carbon cycle during the early Eocene hyperthermals. Most previous studies have focused on the marine carbon cycle. Global marine and terrestrial carbon reservoirs increase over time with increased biomass growth and oceanic acidification/carbon sequestration. As stated in the introduction, this storage of carbon can be approximated as the difference between NPP and Rs. In some areas (such as permafrost regions) the net sink outweighs the net loss via Rs. These regions have the potential to contain thousands of petagrams of carbon.

Prior, and up to the PETM, the planet experienced a steady increase in global temperature. As shown by Lourens *et al*., (2005) and Galeotti *et al*., (2010), the PETM and subsequent hyperthermals appear correlated with orbital forcing and might have provided a catalyst for permafrost degradation, which not only acted as a positive feedback to global warming, but also provided a future surface area for biomass growth and terrestrial carbon sequestration. As Figure 4.1 displays, there is a transition from a net source of terrestrial carbon to a net sink, which occurs between the control simulation to the 500 ppmv simulation. Due to multiple boundary condition alterations between the two simulations, this observation cannot be stated as a significant result. More interestingly, however, the transition between the 750 ppmv simulations and the 1000 ppmv simulation indicates a major global shift in restocking terrestrial carbon reservoirs.

During the transition from 750 ppmv to 1000 ppmv, the Northern Hemisphere becomes nearly permafrost free, while Antarctica retains a large permafrost region. This result aids in explaining why the NPP and Rs of Antarctica were reduced in comparison to other landmasses. With permafrost removed from the Northern Hemisphere, coupled with increased high-latitude temperatures, the indirectly enabled increased vegetation growth and an avenue for terrestrial sequestration driving towards a recovery scenario from the PETM. This modeled scenario would aid in explaining the successively smaller hyperthermal events, as the reservoir had less time to recover resulting in less intense hyperthermals (ETM2, ETM3). Beerling (2000) used terrestrial carbon cycle model global paleoclimate simulations as well as an independent global carbon isotope mass balance analysis to show there was an increase in the terrestrial carbon pool leading up to the PETM (55.5 Ma). The conclusion of Beerling (2000) aligns with the results of this research, demonstrating immense carbon sequestering potential of the terrestrial biosphere. Furthermore, the two step-permafrost degradation of first, the high latitude Northern Hemisphere carbon reservoirs between 750 and 1000 ppmv and second, Antarctica would aid in explaining the magnitude of the PETM.

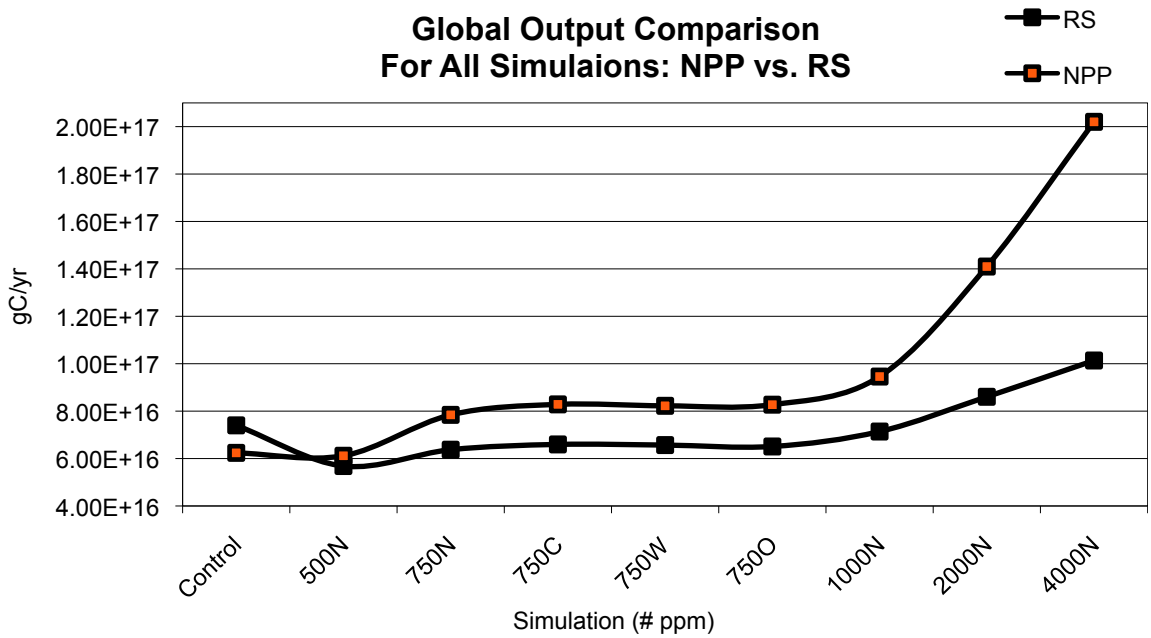

Figure 4.1: Comparison of model simulation NPP and Rs global totals This displays the transition from net source (control) to net sink as atmospheric carbon begins to be sequestered by the terrestrial and oceanic carbon reservoirs. As the graph displays, the potential for a run-a-way sequestration and rapid build up of terrestrial carbon reservoirs does not occur until ~1000 pmmv atmospheric CO_2.

Limitation of this work including the models inability to capture the onset of the PETM, stems from the core functions of the model, model biases, area matrix-based calculations, and the error associated with NPP and Rs itself. GENESIS is a steady state model, which completes simulations to a state of equilibrium between the various components incorporated within GENESIS. This approach effectively bypasses the initial threshold of the PETM because the model (as used here) does not account for time-varying parameters (i.e. atmospheric CO_2) to be incorporated. Instead, each simulation is provided a set of initial parameters and brought to equilibrium with those set parameters. Transient modeling allows for continuously changing concentrations of greenhouse gases

and would allow for a more realistic changes, however, given the long time scale of the events like the PETM, this is not feasible. Given that Rs and NPP are highly correlated, reflecting change in temperature and precipitation (i.e. the Rs model), any biases within those two parameters would appear in NPP and Rs. The global total calculations were limited by the means of their calculation. As stated in the methods section, the NPP and Rs global totals are processed via a terrestrial land-area array. This array matches the 2°x2° resolution of the model and therefore follows the same constraints of latitude and longitude. Due to the oblate spheroid shape of the Earth, the equatorial regions naturally cover a larger area per grid cell versus the poles. With small polar areas per grid cell, coupled with high equatorial results for both parameters, this has the affect of creating enormous global totals biased by the equatorial region. This issue was solved by basing the global totals for NPP and Rs on their respective global means. While more accurate overall, this is not an ideal calculation methodology. Lastly, published NPP and Rs estimates carry large error bars of up to +/- 20 PgC/yr. While great effort was put into finding a logical and accurate means of NPP and Rs calculation significant error does inherently exist within each parameter, which can propagate through the calculations.

Initially, the goals of this research were to better understand the characteristics of a potential carbon release due to permafrost and Antarctica's role in this release. While it was shown that there was an adequate permafrost-based carbon reservoir to provide an increase in global atmospheric CO_2 and temperature consistent with the PETM, the model appears to have captured a mechanism for the planets recovery from the PETM, by quickly restocking the terrestrial carbon reservoirs. Due to Antarctica's slower response to warming and orbital forcing, it had the potential to release carbon near the peak of the

PETM, as high latitude surface temperatures increased to a point allowing for the degradation of permafrost. This does not disprove the original hypothesis of this research, rather it spawns further questions as to the exact pacing of the event. At the peak of the PETM, post permafrost thaw, high latitude temperatures would have been initially too warm to sustain permafrost, however, due to high net carbon fixation (high NPP aka atmospheric carbon sequestration) global temperatures would begin to cool. This would eventually develop favorable conditions for permafrost growth. Based on the potential rates of carbon storage shown by these calculations, substantial (~4,000 PgC) terrestrial carbon reservoirs would have restocked within as the planet recovered from the PETM, and prior to the subsequent hyperthermals following the PETM. Due to the pacing of the subsequent events, the carbon reservoir would have been reduced resulting in a smaller hyperthermal. Additionally, as shown in this research, the Antarctic permafrost did not thaw until atmospheric CO_2 reached ~2000 ppmv. In post PETM hyperthermals, peak global temperatures may have been reduced in comparison to the PETM, due to a smaller available terrestrial carbon reservoir, therefore Antarctica permafrost may have remained intact during subsequent hyperthermal events. This hypothesis is a topic for further future research.

CHAPTER 5

CONCLUSIONS

This research has shown that global terrestrial carbon reservoirs contained ample resources to drive a PETM-scale event. This is demonstrated via adequate global permafrost extent, as shown in section 3.2.1, and progressive low to high-latitude biomass degradation that drove global temperature increase (via increased greenhouse gas concentrations). The onset of these events is a result of a series of high eccentricity and high obliquity orbital cycles, triggering onset of permafrost thaw leading to the PETM. Near the crest of peak warming, terrestrial soil carbon rapidly increased globally, as shown in section 3.2.2, providing a negative cooling feedback, by sequestering atmospheric carbon (also demonstrated by Beering, (2000)). This is seen in Figure 4.1, with larger global NPP totals per simulation over Rs. This acted to restore global terrestrial carbon reservoirs, with a global net carbon sink providing a vulnerable carbon source for successive hyperthermal events. As the global carbon budget became balanced, NPP and Rs began to reestablish the near one-to-one ratio that existed prior to the onset of the event.

The model used here, has the ability to capture net primary production in great detail, due to various model constraints and correlations between the leaf area index, vegetated light-use efficiency, temperature, and precipitation. The offline soil respiration model utilized for this research relied solely on temperature and precipitation. Due to this, soil respiration results are less responsive to biomass variation than NPP and ignore the effects of permafrost degradation. Regardless, soil respiration in the control simulation is consistent with modern day estimates. Use of a transient coupled NPP and

Rs global land/atmosphere climate model with a higher resolution and deeper soil model would likely yield more precise results.

Overall, the simulations described herein are consistent with results found in similar research on this time period (Beerling, 2000 among others). This further confirms that research of this nature has the potential to understand the response of the Earth to orbital and climate forcing during the Palaeocene-Eocene transition, and through climate forcing understand the potential planetary response to future global warming.

REFERENCES

Bahn, M. *et al.* Soil Respiration at Mean Annual Temperature Predicts Annual Total Across Vegetation Types and Biomes. Biosciences Discussions **6**, 11501 – 11520, (2009).

Beer, C. *et al.* Terrestrial Gross Carbon Dioxide Uptake: Global Distribution and Covariation with climate. *Science* **329**. 834-838 (2010).

Beerling, D. Increased terrestrial carbon storage across the Palaeocene-Eocene boundary. *Elsevier Science B.V* **161**. 395 – 405, (2000).

Beerling, D., Berner, R. A., Mackenzie, F. T., Harfoot, M. B. & Pyle, J. A. Methane and the CH_4-related greenhouse effect over the past 400 million years. *American Journal of Science* **309**, 97-113 (2009).

Berner, R. A. & Caldeira, K. The need for mass balance and feedback in the geochemical carbon cycle. *Geological Society of America* **25**, 955-956 (1997).

Bernoux, M., Cerri, C. C., Neill, C. & de Moraes, J. F. L. The use of stable carbon isotopes for estimating soil organic matter turnover rates. *GEODERMA* **82**, 43-58 (1998).

Bowen, G. J., Beerling, D. J., Koch. P. L., Zachos, J. C. & Quanttlebaum, T. A humid climate state during the Palaeocene/Eocene thermal maximum. *Nature* **432**, 495-499 (2004).

Brierley, C. M. *et al.* Greatly expanding tropical warm pool and weakened Hadley circulation in the early Pliocene. *Science* **323**, 1714-1717 (2009).

Campbell, I. B., Claridge, G. G. C., Campbell, D. I. & Balks, M.R. Permafrost properties in the McMurdo Sound-Dry Valley region of Antarctica. *Seventh International Conference* **55**, 121-126 (1998).

Conway, H., Hall, B. L., Denton, G. H., Gades, A. M. & Waddington, E. D. Past and future grounding-line retreat of the west Antarctic ice sheet. *Science* **286**, 280-283 (1999).

Davidson, E. A., Belk, E. & Boone, R. D. Soil water content and temperature as independent or confounded factors controlling soil respiration in a temperate mixed hardwood forest. *Global Change Biology* **4**, 217-227 (1998).

Del Grosso, S. *et al.* Global Potential Net Primary Production Predicted From Vegetation Class, Precipitation, and Temperature. *Ecology* **88(9)**, 2117-2126 (2008).

Denman, K. L. *et al.* Couplings Between Changes in the Climate System and Biogeochemistry. In: Climate Change 2007: The Physical Science Basis. Contribution of Working Group I to the Fourth Assessment Report of the Intergovernmental Panel on Climate Change. *Cambridge University Press*, (2007).

Dickens, G. R., Castillo, M. M. & Walker, J. C. G. A blast of gas in the latest Paleocene: Simulating first-order effects of massive dissociation of oceanic methane hydrate. *Geology* **25**, 259-262 (1997).

Dinel, H., Mathur, S. P., Brown, A. & Lévesque, M. A field study of the effect of depth on methane production in peatland waters: equipment and preliminary results. *Journal of Ecology* **76**, 1083-1091 (1988).

Dorrepaal, E. *et al.* Carbon respiration from subsurface peat accelerated by climate warming in the subarctic. *Nature* **460**, 616-619 (2009).

Doughty, C. E. & Field, C. B. Agricultural net primary production in relation to that liberated by the extinction of Pleistocene mega-herbivores: an estimate of agricultural carrying capacity. *Environmental Research Letters* **5**, (2010).

Eswaran, H., Van Den Berg, E. & Reich, P. Organic carbon in soils of the world. *Soil Sci. Soc.* **57**, 192-194 (1993).

Geleotti, S. *et al.* Orbital chronology of early Eocene hyperthermals from the Contessa Road section, central Italy. *Earth and Planetary Science Letters* **290**, 192-200 (2010).

Jobbágy, E. G. & Jackson, R. B. The vertical distribution of soil organic carbon and its relation to climate and vegetation. *Ecological Society of America* **10**, 423-436 (2000).

Harrison, S. P. & Prentice, C. I. Climate and CO_2 controls on global vegetation distribution at the last glacial maximum: analysis based on palaeovegetation data, biome modelling and palaeoclimate simulations. *Global Change Biology* **9**, 983-1004 (2003).

Haxeltine, A. & Prentice, C. I. A General Model for the Light-Use Efficiency of Primary Production. *Functional Ecology*, Vol. 10, No. 5, 551-561 (1996).

Haxeltine, A. & Prentice, C. I. BIOME3: An equilibrium terrestrial biosphere model based on ecophysiological constraints, resource availability, and competition among plant functional types. *Global Biogeochemical Cycles*, Vol 10, No. 4, 693-709 (1996).

Higgins, J. A. & Schrag, D. P. Beyond methane: Towards a theory for the Paleocene-Eocene Thermal Maximum. *Earth and Planetary Science Letters* **245**, 523-537 (2006).

Hoffman, D. L. & Simmons, A. The Resilient Earth: Science, Global Warming and the Fate of Humanity. BookSurge Publishing, 1st edition, (2008).

Huber, M., Sloan, L. C. & Shellito, C. Early Paleogene oceans and climate: A fully coupled modeling approach using the NCAR CCSM. *Geological Society of America* **369**, 25-47 (2003).

Kalbitz, K. *et al.* Changes in properties of soil-derived dissolved organic matter induced by biodegradation. *Soil Biology & Biochemistry* **35**, 1129-1142 (2003).

Kaplan, J. O. *et al.* Climate change and Arctic ecosystems: 2. Modeling, paleodata-model comparisons, and future projections. *Journal of Geophysical Research* **108**, 12-1 – 12-17 (2003).

Katz, M. E., Pak, D. K., Dickens, G. R. & Miller, K. G. The source and fate of massive carbon input during the latest Paleocene thermal maximum. *Science* **286**, 1531-1533 (1999).

Kennet, J. P. & Stott, L. D. Abrupt deep-sea warming, palaeoceanographic changes and benthic extinctions at the end of the Palaeocene. *Nature* **353**, 225-229 (1991).

Kurtz, A. C., Kump, L. R., Arthur, M. A., Zachos, J. C. & Paytan, A. Early Cenozoic decoupling of the global carbon and sulfur cycles. *Paleoceanography* **18**, 1090, DOI: 10.1029/2003PA000908 (2003).

Laskar, J. *et al.* A long-term numerical solution for the insolation quantities of the Earth. *Astronomy and Astrophysics, EDP Sciences* **428**, 261-285 (2004).

Linn, D. M. & Doran, J. W. Effect of water-filled pore space on carbon dioxide and nitrous oxide production in tilled and nontilled soils. *Soil Sci. Soc. Am. J.* **48**, 1267-1272 (1984).

Liu, Z. *et al.* Global Cooling During the Eocene-Oligocene Climate Transition. *Science* **323**, 1187 (2008).

Lou, Y. Zhou, X. Soil Respiration and the Environment. *Academic Press*. ISBN: 0120887827, 9780120887828, P. 17 (2006).

Lourens, L. J. *et al.* Astronomical pacing of late Palaeocene to early Eocene global warming events. *Nature* **435**, 1083-1087 (2005).

Metje, M. & Frenzel, P. Effect of temperature on anaerobic ethanol oxidation and methanogenesis in acidic peat from northern wetland. *Applied and Environmental Microbiology* **71**, 8191-8200 (2005).

Nicolo, M. J., Dickens, G. R., Hollis, C. J. & Zachos, J. C. Multiple early Eocene hyperthermals: Their sedimentary expression on the New Zealand continental margin and in the deep sea. *Geology* **35**, 699-702 (2007).

Pagani, M., Liu, Z., LaRiviere, J. & Ravelo, A. C. High Earth-system climate sensitivity determined from Pliocene carbon dioxide concentration. *Nature Geoscience* **3**, 27-30 (2010).

Pagani, M., Caleira, K., Berner, R. & Beerling, D. The role of terrestrial plants in limiting atmospheric CO_2 decline over the past 24 million years. *Nature* **460**, 85-89 (2009).

Pancost, R. D. *et al.* Increased terrestrial methane cycling at the Palaeocene-Eocene thermal maximum. *Nature* **449**, 332-335 (2007).

Paytan, A., Kastner, M., Campbell, D. & Thiemens, M. H. Sulfur isotopic composition of Cenozoic seawater sulfate. *Science* **282**, 1459-1462 (1998).

Pearson, P. N. & Palmer, M. R. Atmospheric carbon dioxide concentrations over the past 60 million years. *Nature* **406**, 695-699 (2000).

Pollard, D. & Thompson, S. L. Use of a land-surface-transfer scheme (LSX) in a global climate model: the response to doubling stomatal resistance. *Global and Planetary Change* **10**, 129-161 (1995).

Post, W. M., Emanuel, W. R., Zinke, P. J. & Stangenberger, A. G. Soil carbon pools and world life zones. *Nature* **298**, 156-159 (1982).

Raich, J. W. & Potter, C. S. Global patterns of carbon dioxide emissions from soils. *Global Biogeochemical Cycles* **9**, 23-36 (1995).

Raich, J. W. & Schlesinger, W. H. The global carbon dioxide flux in soil respiration and its relationship to vegetation and climate. *Tellus* **44B**, 81-99 (1992).

Röhl, U., Bralower, T. J., Norris, R. D. & Wefer, G. New chronology for the late Paleocene thermal maximum and its environmental implications. *Geology* **28**, 927-930 (2000).

Salzmann, U., Haywood, A. M., Lunt, D. J., Valdes, P. J. & Hill, D. J. A new global biome reconstruction and data-model comparison for the Middle Pliocene. *Global Ecology and Biogeography* **17**, 432-447 (2008).

Schaefer, K. *et al.* Combined simple biosphere/Carnegie-Ames-Stanford approach terrestrial carbon cycle model. *Journal of Geophysical Research* **113**, DOI:10.1029/2007JG000603 (2008).

Schuur, E. A. G. *et al.* Vulnerability of permafrost carbon to climate change: implications for the global carbon cycle. *Bioscience* **58**, 701- 714 (2008).

Sewall, J. O., Sloan, L. C., Huber, M. & Wing, S. Climate sensitivity to changes in land surface characteristics. *Global and Planetary Change* **26**, 445-465 (2000).

Sluijs, A. *et al.* Subtropical Arctic Ocean temperatures during the Palaeocene/Eocene thermal maximum. *Nature* **441**, 610-613 (2006).

Tarnocai, C., Canadell, J. G., Schuur, E. A. G., Kuhry, P., Mazhitova, G., Zimov., S. Soil Organic Carbon Pools in the Northern Circumpolar Permafrost Region. *Global Biogeochemical Cycles*, Vol. 23, (2009).

Thomas, D. J., Zachos, J. C., Bralower, T. J., Thomas, E. & Bohaty, S. Warming the fuel for the fire: Evidence for the thermal dissociation of methane hydrate during the Paleocene-Eocene thermal maximum. *Geology* **30**, 1067-1070 (2002).

Weijers, J. W. H., Schouten, S., Sluijs, A., Brinkuis, H. & Sinninghe Damsté, J. S. Warm arctic continents during the Palaeocene-Eocene thermal maximum. *Earth and Planetary Science Letters **261**, 230-238 (2007).*

White, J. R., Shannon, R. D., Weltzin, J. F., Pastor, J. & Bridgham, S. D. Effects of soil warming and drying on methane cycling in a northern peatland mesocosm study. *Journal of Geophysical Research* **113**, DOI:10.1029/2007JG000609 (2008).

Wilson, D. S. & Luyendyk, B. P. West Antarctic paleotopography estimated at the Eocene-Oligocene climate transition. *Geophysical Research Letters* **36**, DOI:10.1029/2009GL039297 (2009).

Zachos, J. C., Dickens, G. R. & Zeebe, R. E. An Early Cenozoic perspective on greenhouse warming and carbon-cycle dynamics. *Nature* **451**, 279-283 (2008).

Zachos, J. C. *et al.* Rapid acidification of the ocean during the Paleocene-Eocene thermal maximum. *Science* **308**, 1611-1615 (2005).

Zhang, Y. Xu, M. Chen, H. Adams, J. Global Pattern of NPP to GPP ratio derived from MODIS data: effects of ecosystem type, geographical location and climate. *Global Ecology and Biogeography* **18**, 280-290 (2009).

Zimov, S. A. *et al.* Permafrost carbon: Stock and decomposability of a globally significant carbon pool. *Geophysical Research Letters* **33**, DOI:10.1029/2006GL027484 (2006).

Zimov, S. A., Schuur, E. A. G. & Chapin III, F. S. Permafrost and the global carbon budget. *Science* **312**, 1612-1613 (2006).

Zeebe, R. E., Zachos, J. C. & Dickens, G. R. Carbon dioxide forcing alone insufficient to explain Palaeocene-Eocene Thermal Maximum warming. *Nature Geoscience* **2**, 576-580 (2009).